



THE HONG KONG
POLYTECHNIC UNIVERSITY

香港理工大學

Pao Yue-kong Library

包玉剛圖書館

Copyright Undertaking

This thesis is protected by copyright, with all rights reserved.

By reading and using the thesis, the reader understands and agrees to the following terms:

1. The reader will abide by the rules and legal ordinances governing copyright regarding the use of the thesis.
2. The reader will use the thesis for the purpose of research or private study only and not for distribution or further reproduction or any other purpose.
3. The reader agrees to indemnify and hold the University harmless from and against any loss, damage, cost, liability or expenses arising from copyright infringement or unauthorized usage.

IMPORTANT

If you have reasons to believe that any materials in this thesis are deemed not suitable to be distributed in this form, or a copyright owner having difficulty with the material being included in our database, please contact lbsys@polyu.edu.hk providing details. The Library will look into your claim and consider taking remedial action upon receipt of the written requests.

The Hong Kong Polytechnic University

Department of Industrial and Systems Engineering

**Failure Prediction of Dental Restoration Using a
CT-based Finite Element and Damage Mechanics
Approach**

Chan Yiu Pong

**A thesis submitted in partial fulfillment of the
requirements for the degree of Doctor of Philosophy**

August 2011

Certificate of Originality

I hereby declare that this thesis is my own work and that, to the best of my knowledge and belief, it reproduces no material previously published or written, nor material that has been accepted for the award of any other degree or diploma, except where due acknowledgement has been made in the text.

CHAN Yiu Pong

Abstract

Abstract of thesis entitled “Failure Prediction of Dental Restoration Using a CT-based Finite Element and Damage Mechanics Approach”

submitted by CHAN Yiu Pong

for the degree of Doctor of Philosophy

at the Hong Kong Polytechnic University in August, 2011

To perform dental research on living subjects is expensive and needs to take ethical issues into account. Usage of computer simulation offers a better alternative with the capability of detailed stress analysis. In this study, a computational approach has been developed for failure prediction of dental restoration so that experimental effort can be minimized.

The unit cell modeling method has been applied to predict the constitutive relations of dental composites, enamel and dentin. For most dental composites, particles have high loading and are non-spherical in shape, so a CAD-based modeling technique has been utilized to assist in the preparation of the unit cell models. Through employing the inter-part parametric assembly modeling characteristics of CAD tools, modeling of 3D triphasic unit cells with various particle morphologies and particle volume fractions can be achieved effectively and efficiently. The particles are packed using body centered cubic (BCC) or face centered cubic (FCC) packing architectures instead of traditional simple cubic (SC) architecture which has a low packing efficiency. The effect of interfacial debonding damage on the mechanical behavior of a dental composite has been predicted with the application of FE analysis. The mechanical behavior includes elastic modulus, tensile strength, and stress-strain relations for different particle morphologies and volume fraction cases. In addition, the stress

concentration, stress distribution, and damage mechanism of the composite at the micro-scale have been predicted.

In view of the hierarchical structure of enamel and dentin, columnar unit cell models have been designed to determine the anisotropic mechanical behavior. The model for enamel consists of rod and interrod constituents, peritubular and intertubular constituents are used for dentin. In this project, a new method, which integrates nanoindentation, finite element modeling, and artificial neural network techniques, is proposed to determine the elastoplastic stress-strain relations of the four constituents. Thus, the resulting mechanical properties of enamel and dentin in multi-scale include their anisotropic elastoplastic mechanical description parameters and the isotropic elastoplastic stress-strain relations of their four constituents.

To build up a solid computational model of a tooth and its corresponding mandible, a method has been proposed to construct 3D models from 2D scanned images. The models established using the proposed method are characterized by the ease of performing modifications. Facilitated by the CAD tools, the 3D tooth model has been virtually restored with a Class II mesio-occlusal (MO) restoration. This is done through five procedures, i.e. data point extraction, tissue surfaces construction, NURBS object modeling, assembly modeling, and FE model construction. The generated mandible assists in defining the boundary conditions of the tooth model. The tooth model is triphasic, including the enamel, dentin, and pulp phases. The determined anisotropic elastoplastic mechanical properties of enamel and dentin have also been incorporated into the model. Concerning the radial variation structure of the enamel and dentin, the tooth model has been partitioned into 18 regions, with a specific local coordinate system for each region. Stress analysis and failure

prediction of the restoration have then been conducted using the established 3D assembly FE model. The simulation result showing the interfacial debonding occurred once the mastication loading exceeded a critical value of 140N is in a good agreement with the experimental findings.

The deliverables of the proposed method in modeling mechanical properties using unit cell models can facilitate the design of dental composites and other particulate reinforced composites systematically rather than performing development experimentally by means of trial-and-error. Regarding the method used to determine the mechanical properties of the micro-scale constituents of enamel and dentin, it can also benefit other applications involving the determination of the elastoplastic mechanical properties of isotropic materials having small volume. For the established 3D assembly FE model, it also can be applied to other research studies where a tooth model is required. The application of the new method in constructing 3D FE models from 2D scanned images is not limited to the dental industry but also to other medical applications. It can be applied in creating patient-specific models of any body tissue part using CT scanning images.

Acknowledgements

I am heartily thankful to Prof. C.Y. Tang for his guidance, encouragement, and support from the initial to the final stage of my study. His comments and advice have inspired me not just in academic work but also my value of life. I would like to thank Dr. C.P. Tsui for providing me invaluable help and useful suggestions. I am also grateful to Prof. B. Gao for the CT images.

Table of Contents

Abstract	i
Acknowledgements	iv
Table of Contents	v
List of Figures.....	ix
List of Tables	xvi
Chapter 1. Introduction.....	1
1.1. Background of Study.....	1
1.2. Project Objectives	6
1.3. Organization of Thesis	9
Chapter 2. Literature Review.....	11
2.1. Categories of Restoration Materials.....	11
2.2. Mechanical Properties and Failure of Dental Composites.....	14
2.3. Mechanical Modeling and Failure Prediction of Composites.....	19
2.4. Mechanical Properties of Enamel and Dentin.....	24
2.5. Micro-Structure of Enamel and Dentin.....	28
2.6. Mechanical Modeling of Enamel and Dentin	30
2.7. CT-Based Solid Modeling in Dental Research.....	33
2.8. Finite Element Theory.....	36
Chapter 3. Mechanical Responses Prediction of Particulate Reinforced Dental Composite	41
3.1. Material Properties and Mechanical Damage Modeling.....	44

3.2.	CAD-Based Method for Cell Model Construction	45
3.3.	Micro-Damage Mechanism Prediction	53
3.3.1.	Effect of Particle Morphology and Volume Fraction on the Stress Concentration and Distribution	53
3.3.2.	Effect of Particle Morphology and Volume Fraction on the Interfacial Debonding Damage Process and the Stress Distribution	58
3.4.	Macro-Structural Behavior Prediction	64
3.4.1.	Effect of Particle Morphology and Micro-Damage on the Mechanical Properties	64
3.4.1.1.	Elastic Modulus	64
3.4.1.2.	Stress-Strain Relation	66
3.4.1.3.	Tensile Strength	69
3.4.2.	Effect of Particle Volume Fraction and Micro-Damage on the Mechanical Properties	71
3.4.2.1.	Elastic Modulus	71
3.4.2.2.	Stress-Strain Relation	72
3.4.2.3.	Tensile Strength	74
Chapter 4.	Determination of the Mechanical Properties of Enamel and Dentin in Multi-Scale	76
4.1.	Determination of the Isotropic Elastoplastic Parameters of Micro- Scale Tooth Constituents	79
4.1.1.	Nanoindentation Experiment	79

4.1.2.	Finite Element Modeling of Indentation.....	89
4.1.3.	Artificial Neural Modeling	92
4.1.4.	Results and Discussions.....	95
4.2.	Determination the Anisotropic Stress-Strain Relations of Enamel and Dentin	102
4.2.1.	Finite Element Modeling	102
4.2.1.1.	Representative Volume Element for Enamel and Dentin.....	102
4.2.1.2.	Tensile Testing	105
4.2.1.3.	Shear Testing.....	108
4.2.2.	Calibration of Mechanical Parameters.....	112
4.2.3.	Results and Discussions.....	119
Chapter 5.	Failure Prediction of Dental Restoration Using a CT-Based Finite Element Tooth Model.....	121
5.1.	CT-Based FE Model Construction for a Class II MO Restored Tooth and a Mandible	124
5.1.1.	Data Point Extraction.....	124
5.1.2.	Tissue Surfaces Construction	128
5.1.3.	NURBS Object Modeling.....	133
5.1.4.	Assembly Modeling.....	134
5.1.5.	FE Model Construction.....	135
5.2.	Material Properties and Mechanical Damage Modeling.....	136
5.3.	Stress Distribution and Failure Prediction of Restoration.....	138

Chapter 6.	Conclusions and Future Work	141
	6.1. Conclusions and Statement of Originality	141
	6.2. Future Work	145
References	146

List of Figures

Figure 2.1:	The two-dimensional unit cell modeling scheme	21
Figure 2.2:	The three-dimensional unit cell modeling scheme	22
Figure 2.3:	The reported elastic modulus of enamel from the literature	25
Figure 2.4:	The reported elastic modulus of dentin from the literature.....	26
Figure 2.5:	AFM image of enamel surface (Ge et al., 2005).....	29
Figure 2.6:	AFM images of dentin specimen (Kinney et al., 1993).....	30
Figure 3.1:	Schematic diagram describing different packing systems of RVE.....	42
Figure 3.2:	Schematic diagram of a unit cell with spherical particles packed in a body centred cubic system	43
Figure 3.3:	Schematic diagram of a unit cell with spherical particles packed in a face centred cubic system	43
Figure 3.4:	Particle geometries being used in this study (a) sphere, (b) dodecahedron, (c) truncated octahedron, and (d) cuboctahedron	47
Figure 3.5:	Unit cell models with spherical particle phase packed using the body- centred cubic system with a volume fraction of (a) 20%, (b) 30%, (c) 40%, (d) 50%, and (e) 60%.....	51
Figure 3.6:	(a) Face-centred cubic unit cell model comprising dodecahedral particles, (b) development of the cell model, (c) finite element grid of the matrix, interface, and particle phases	52

Figure 3.7:	FEM calculated stress concentration factor (SCF) vs. four particle morphologies.....	53
Figure 3.8:	FEM calculated stress concentration factor (SCF) vs. various particle volume fractions.....	54
Figure 3.9:	Predicted stress distribution in the (a) matrix, (b) interphase, and (c) particle phases in the compomer dental system with PVF=20% for spherical particles under tensile deformation with strain value of 0.3%. (in each phase, the bold arrow shows the loading direction; the region wrapped by the dotted lines describes the areas having high stress concentration value).....	55
Figure 3.10:	Predicted stress distribution in the (a) matrix, (b) interphase, and (c) particle phases in the compomer dental system with PVF=20% for dodecahedral particles under tensile deformation with strain value of 0.3%. (in each phase, the bold arrow shows the loading direction; the dotted line highlights the position with high stress concentration value)....	56
Figure 3.11:	Predicted stress distribution in the (a) matrix, (b) interphase, and (c) particle phases in the compomer dental system with PVF=20% for cuboctahedral particles under tensile deformation with strain value of 0.3%. (in each phase, the bold arrow shows the loading direction; the dotted line highlights the position with high stress concentration value)....	56
Figure 3.12:	Predicted stress distribution in the (a) matrix, (b) interphase, and (c) particle phases in the compomer dental system with PVF=20% for	

truncated octahedral particles under tensile deformation with strain value of 0.3%. (in each phase, the bold arrow shows the loading direction; the dotted line highlights the position with high stress concentration value)..... 57

Figure 3.13: Predicted stress distribution in the (a) whole unit cell model with spherical particle morphology and the corresponding (b) interphase at various strain value: (i) 0.75%, (ii) 2.5%, and (iii) 3%. (the bold arrow indicates the loading direction)..... 59

Figure 3.14: Predicted stress distribution in the (a) whole unit cell model with dodecahedral particle morphology and the corresponding (b) interphase at various strain value: (i) 0.6%, (ii) 1.1%, and (iii) 3%. (the bold arrow indicates the loading direction)..... 60

Figure 3.15: Predicted stress distribution in the (a) whole unit cell model with cuboctahedral particle morphology and the corresponding (b) interphase at various strain value: (i) 0.45%, (ii) 0.6%, (iii) 1.65%, and (iv) 3%. (the bold arrow indicates the loading direction) 61

Figure 3.16: Predicted stress distribution in the (a) whole unit cell model with truncated octahedral particle morphology and the corresponding (b) interphase at various strain value: (i) 0.3%, (ii) 0.6%, (iii) 1.65%, and (iv) 3%. (the bold arrow indicates the loading direction) 62

Figure 3.17: Comparison between the predicted elastic moduli of the dental composites with different particle morphologies and the experimental data.....	65
Figure 3.18: Predicted stress-strain curves of the compomer composite with particle volume fraction of 60% and different particle morphologies.....	67
Figure 3.19: Predicted stress-strain curves of the compomer composite with dodecahedral shaped particle, particle volume fraction of 47%, and different interfacial strength values	69
Figure 3.20: Predicted tensile strength of the compomer composite vs. various particle morphologies.....	70
Figure 3.21: Comparison between the predicted elastic moduli of the dental composites with different particle loadings and the experimental data	71
Figure 3.22: Predicted elastic modulus for particle with spherical and dodecahedral morphologies.....	72
Figure 3.23: Predicted stress-strain curves of the compomer composite with dodecahedral shaped particle, σ_c equals to 60% of matrix strength, and different particle volume fractions.....	73
Figure 3.24: Predicted tensile strength of the compomer composite vs. various particle volume fractions.....	74
Figure 4.1: SEM images in different sectional views of enamel and dentin in micro-scale.....	77
Figure 4.2: A typical load-displacement curve.....	80

Figure 4.3:	A schematic representation of indentation showing a variety of quantities used in the analysis.....	80
Figure 4.4:	Schematic diagram illustrating the indentation paths for nanoindentation tests.....	82
Figure 4.5:	The designed fixture for measuring indentation responses of specimens with curved surfaces	83
Figure 4.6:	Indentations being made (a) near the edge of the hollow tubule and (b) near the interface among the constituents.....	85
Figure 4.7:	Loading curve for a nanoindent located near a free edge	86
Figure 4.8:	Calculated elastic modulus of enamel along the bucco-lingual surface and cross-sectional surface	86
Figure 4.9:	Calculated elastic modulus of dentin versus relative distance from DEJ to pulp	87
Figure 4.10:	The representative indentation responses of tooth constituents.....	88
Figure 4.11:	(a) Geometry of the Berkovich indenter; (b) A schematic illustration of indentation FE model.....	90
Figure 4.12:	Mapping of input and output quantities	93
Figure 4.13:	A hidden layer of an ANN model with S neurons and R inputs.....	95
Figure 4.14:	The von Mises stress distribution of the FE model with a mechanical parameter set of ($E=27.21\text{GPa}$, $\sigma_y =30\text{MPa}$, $n=0.2$) in the period of (a) $t=0.5\text{s}$, (b) $t=5\text{s}$, (c) $t=13\text{s}$	96

Figure 4.15:	Examples of the indentation loading curves obtained from FE analysis for the peritubular constituent having various plastic properties.....	97
Figure 4.16:	Changes of final indentation depth h_u for a peritubular constituent with various σ_y and n values.....	97
Figure 4.17:	The squared normalized error values between the output yield stresses from prediction using various trained ANN architectures and the tested datasets.....	99
Figure 4.18:	The squared normalized error values between the output hardening index from prediction using various trained ANN architectures and the tested datasets.....	100
Figure 4.19:	The unit cell models for enamel.....	103
Figure 4.20:	The unit cell models for dentin.....	104
Figure 4.21:	The one-eighth unit cell model of enamel for tensile test analysis.....	106
Figure 4.22:	The one-eighth unit cell model of dentin for tensile test analysis.....	106
Figure 5.1:	The five-stage method in generating a 3D CT-based FE model from 2D scanned images.....	122
Figure 5.2:	Schematic illustration of the proposed approach in creating a more accurate model of a Class II MO restored molar with consideration of materials' micro-structure in defining properties.....	123
Figure 5.3:	Part of the organized CT images in the top view.....	125

Figure 5.4:	Orientation parameters registration, top <i>T</i> , bottom <i>B</i> , left <i>L</i> , right <i>R</i> , anterior <i>A</i> , and posterior <i>P</i> , for (a) front view images; (b) top view images; and (c) side view images	126
Figure 5.5:	(a) A sliced image with a profile line (about the region with teeth and mandible); (b) the corresponding variations of <i>HU</i> value along the profile line.....	127
Figure 5.6:	The preliminarily obtained geometric point cloud data for (a) mandible, dentin, and pulp descriptions; and (b) enamel description	128
Figure 5.7:	The surface models created through the polygon/facet creation process ..	129
Figure 5.8:	An illustrative example of separating noisy point data and irrelevant facets from the designated mandible tissue surface	130
Figure 5.9:	Surface repairing process involved in the tissue surface construction stage	132
Figure 5.10:	Processes involved in the NURBS object modeling procedure.....	133
Figure 5.11:	Processes involved in the assembly modeling procedure	135
Figure 5.12:	The 18 partitioned regions of the tooth model with their associated local coordinate system.....	137
Figure 5.13:	Predicted stress distribution in the interphase and tooth phase at various loads: (a) 47N, (b) 140N, (c) 152N, (d) 177N, (e) 258N, and (f) 299N	140

List of Tables

Table 2.1:	Mechanical properties of the commonly used dental composite (Xie et al., 2000; Schulze et al., 2003).....	17
Table 3.1:	Material properties of the compomer composite system	45
Table 4.1:	The representative elastic moduli of the four tooth constituents	88
Table 4.2:	The determined plastic properties of the four tooth constituents.....	101
Table 4.3:	The determined transverse isotropic parameters of enamel and dentin	119
Table 5.1:	Mechanical properties of morsel, mandible, and pulp phases	138

Chapter 1. Introduction

1.1. Background of Study

Oral health is considered a foremost global public health problem in the 21st century by the World Health Organization (Petersen, 2009). In China, youngsters of age under 18 have at least one decayed, missing or filled tooth (DMFT), and the number of DMFTs for adults of age ranging from 35 to 44 is 2.1, whilst for the elderly group of age 65-74 years old is 12.4 (Wang et al., 2002). Among the 294 million people in the United States, approximately 44% of the population make at least one dental visit per year and the dental expense involved has increased from US\$374 in 1996 to US\$560 in 2004 (Manski and Brown, 2007). It is also forecasted that dental caries would experience an increasing trend in the near future (Petersen, 2003; 2009). This study can enable closer attention to be paid to the failure prediction of restorative dental materials and thus be of great commercial interest.

There are many reasons for the failure of restorations. Findings from the literature indicate that secondary caries result in the most common cause of failure, and excessive occlusal loading is another significant factor (Sarrett, 2005; Opdam et al., 2007, Drummond, 2008; Frost, 2009; Frencken, 2010). The cause of secondary caries is mainly due to marginal damage (Goldberg, 1990; Hayashi and Wilson, 2003; Forss and Widstrom, 2004), while experimental studies have revealed that mechanical loading affects the integrity of the margin (Davidson and Abdalla, 1994; Baran et al., 2001; Ferracane and Mitchem, 2003, Sakaguchi, 2005). To predict the failure of a restoration,

understanding how mastication loading is spread over a restored tooth is thus crucial. However, ethical restrictions on performing experiments on both humans and animals have limited the biomechanical studies of dental research on live tissue (Magne, 2007; Rodrigues et al., 2009). To save cost as well as minimize the risk in conducting experiments on live subjects, the use of virtual models offers an alternative way for investigation. Hasegawa et al. (2010) have stated that the success of modeling in dental research depends on three factors,

- (i) appropriateness in defining the properties of the materials
- (ii) suitability of the definition of the boundary conditions
- (iii) accuracy in simulating the geometry and surface structure of a tooth

Regarding the first factor, to study the failure prediction of a restoration, definition of the material properties for the restoration composite material, enamel and dentin are thus important.

Particulate reinforced dental composites are extensively used nowadays for restoration applications (Fagundes et al., 2009). Many studies can be found on the effect of polymerization shrinkage and expansion in water on the mechanical properties of dental composites. Since the introduction of compomer-type particulate reinforced dental composites, the shrinkage rate has been found to be compensated by the hydrophilic expansion rate through the water up take, with a net volume change of merely 0.5% (Dentsply, 2011). Eventually, these two factors are no longer the dominant factors affecting the mechanical properties of dental composites. For most of the dental composites, the particles are non-spherical in shape (Gu et al., 2004). Few studies can be

found that investigate the effect of the particle morphology on the mechanical properties of dental composites. Only Yap et al. (2004) have conducted experimental studies in comparing the effect of spherical and non-spherical particles on composite strengths, and a significant effect has been identified. To improve the mechanical properties of restoration composites, a high particle volume fraction is usually involved (Chung et al., 2004). This is because the particles have a higher stiffness than matrix. The interface, probably the least understood of the composite phases, is significantly important since it provides a vital link between the particles and the matrix and can have a crucial effect on the overall performance of the composite. During deformation processes in particulate reinforced composites, debonding at the particle-matrix interface is the most common failure mechanism (Kraus et al., 1997; Tsui et al., 2004). The interfacial debonding damage would affect the mechanical responses of the bulk composite. Therefore, there is a need to predict the micro-damage mechanism and the damage level at various strain states in dental restoration composites such that the failure prediction of this class of material in the macro-structure can be more accurate. The development of a new dental composite with desired mechanical properties is usually carried out experimentally by means of a trial-and-error approach. Since the experimental investigation of mechanical properties of dental composites is not cost-effective, predictive modeling is becoming increasingly important. Conventional computational methods ignoring the development of material damage in service are no longer suitable for the design of this category of material. This is because over-estimation of the maximum applied load of the dental composite would probably occur if the interfacial debonding is not considered. Although particulate reinforced dental composites have been widely studied, the literature seems to

contain little on the effect of these factors on the mechanical properties, which is valuable in designing such materials.

Continuing the consideration of the first factor, evidence from recent research work has indicated that enamel and dentin behave plastically although both the natural bio-composites have long been considered as brittle and hard materials (Nalla et al., 2003; He and Swain, 2007a,c; Ang et al., 2009). Despite the plastic behavior of enamel that is observable, there is a lack of research data describing the plastic mechanical behavior. Enamel and dentin also possess constituents present in radial parallel patterns throughout a tooth. In addition, most of the research studies still assume both materials to be elastic isotropic materials although they are known to be types of elastoplastic anisotropic behaved materials (Lin et al., 2008a; Jiang et al., 2010; Li et al., 2010). This is due to the experiment impediments in identifying their mechanical properties. He and Swain (2007b) and Ang et al. (2009) pointed out that enamel and dentin possess complex micro-structural constituents which greatly affect the mechanical responses in bulk, but such “structure-property” relationship has not been well established. Thus, it is of great interest to understand the relation between the tooth structure and its anisotropic mechanical properties. Preferably, it is desirable to prepare samples at a very small scale, i.e. in the range of microns, where the constituents of enamel and dentin are aligned in a quasi-parallel pattern. In this respect, enamel and dentin can be regarded as composites and these small scale samples can be viewed as representative volume elements providing basic understanding between the materials’ structure and their properties. However, preparing tooth specimens for conventional tests to measure the mechanical properties of enamel and dentin is difficult (Toparli and Koksall, 2005). Moreover, there are

experimental difficulties in identifying the radial variation of the constituents and accordingly preparing samples with desired variations have raised the challenge in determining the mechanical properties of enamel and dentin (Ziskind et al., 2010). In this aspect, the computational hierarchical approach, which is capable of taking into account the structural consideration of the constituents of enamel and dentin, offers a means to determine the desired anisotropic mechanical properties. However, lack of information is present for the elastoplastic properties of the micro-scale constituents. In material science research, quantifying the elastoplastic response of specimens of small size has been characterized as a difficult problem for a long period. This is due to the conventional macro-scale methods, such as tensile and compressive tests, being infeasible for small volume specimens.

Regarding the second factor proposed by Hasegawa et al. (2010), Miura et al. (2009) have stated that periodontal tissues, such as in the mandible, which constrains the location of the tooth, plays an important role for failure prediction in dental research. With consideration of the third factor, advanced digital imaging technology has opened up new possibilities in dentistry. Live tissues involving complex shapes, such as teeth and mandibles, can now be digitized to allow accurate measurement of small changes of irregularities (Rudolph et al., 2006; Persson et al., 2009).

1.2. Project Objectives

The research project is planned to develop a computational approach for failure prediction of dental restoration so that experimental effort can be minimized. The objectives of this study are:

- i. To predict the mechanical properties of particulate reinforced dental composites with various particle morphologies, particle volume fractions, and consideration of interfacial debonding damage
- ii. To predict the isotropic mechanical constitutive relations of micro-scale constituents of a tooth and to predict the anisotropic mechanical properties of enamel and dentin
- iii. To develop a method to create a 3D FE assembly model for a restored tooth and its corresponding mandible based on CT images
- iv. To conduct stress analysis and failure prediction of dental restoration using the 3D FE model established

As mentioned in the previous section, the success of modeling in dental research depends on three factors, appropriateness in defining the properties of the materials, suitability in defining the boundary conditions, and accuracy in simulating the geometry and surface structure of a tooth (Hasegawa et al., 2010). Objectives (i)-(ii) facilitate the determination of more accurate material properties of restoration, enamel and dentin. Objective (iii) helps in the acquisition of 3D geometry of a tooth model using scanned images. Similarly, 3D geometry of the corresponding mandible which constrains the natural location of the tooth model can be obtained, and such model can assist in defining the boundary

conditions of the tooth model. The last objective integrates the findings from the previous objectives and attempts to predict the failure of restoration using a computational approach so that experimental effort can be minimized.

Figure 1.1 describes an overview of methodology. To predict the mechanical behavior of particulate reinforced dental composite with consideration of interfacial debonding damage, the unit cell modeling approach has been applied with the incorporation of FE analysis. A new approach, which integrates nanoindentation, finite element modeling, and artificial neural network techniques, has been proposed to determine the elastoplastic stress-strain relations of the four constituents of teeth at the micro-scale, i.e. the rod and interrod constituents for enamel, and peritubular and intertubular constituents for dentin. To determine the anisotropic elastoplastic properties of enamel and dentin in bulk, the unit cell modeling approach has been adopted with consideration of their hierarchical structures. Unit cell models have been constructed with the incorporation of the determined elastoplastic properties of the four micro-scale constituents. A 3D analytical assembly model, comprising a restored tooth and mandible parts, has been constructed. This was done through a method which can construct 3D models from 2D scanned images and is characterized with modification capability. In assigning material properties, the determined anisotropic elastoplastic mechanical properties of enamel and dentin have been incorporated into the tooth model.

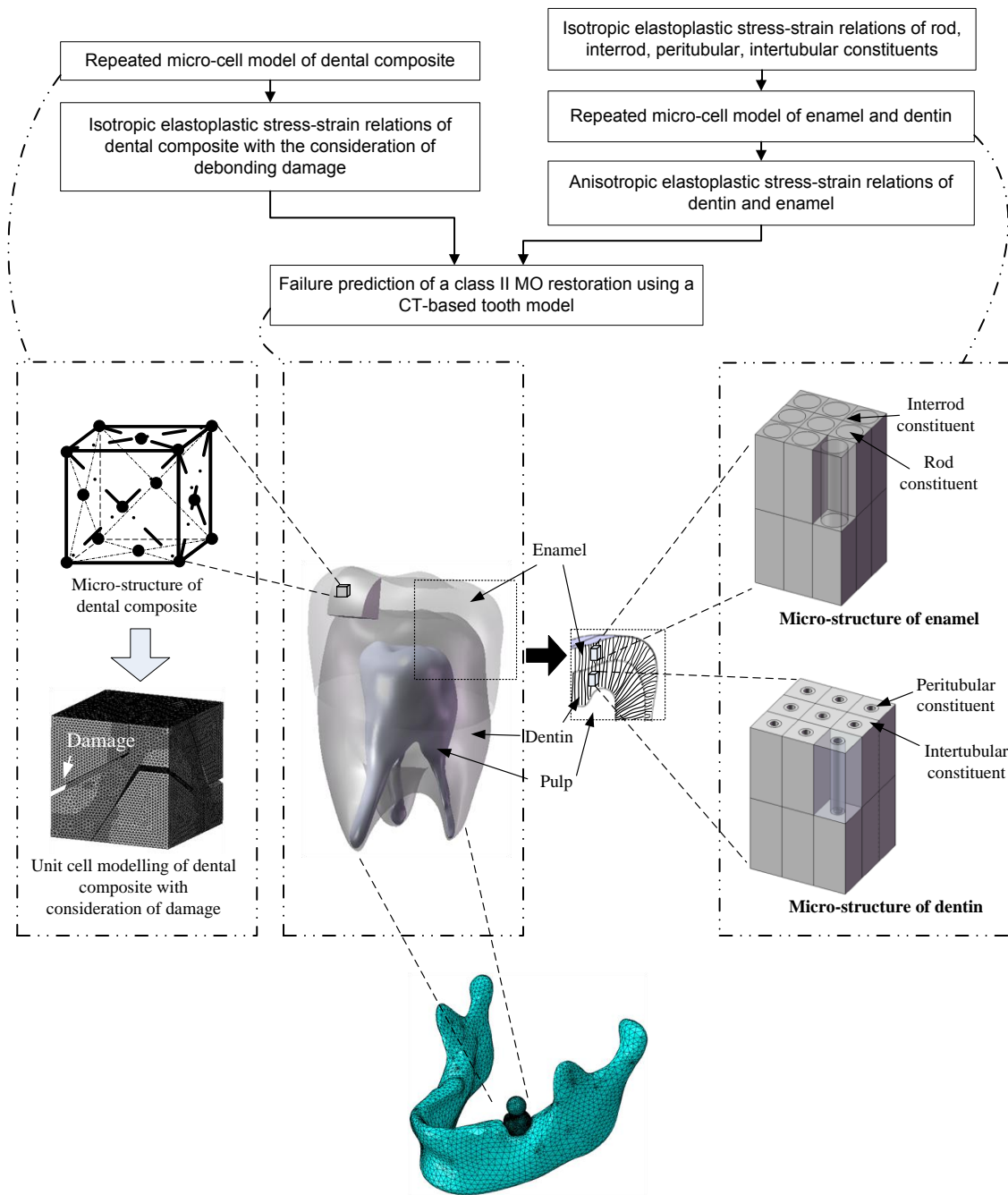


Figure 1.1: Overview of the Methodology

1.3. Organization of Thesis

Chapter 1 gives a brief introduction of the background and the objective of this study.

Chapter 2 presents a literature review on different categories of restoration materials. It is found that particulate reinforced composites with tooth coloring are being increasingly adopted as the filling material. Mechanical properties and the failure causes of commonly used dental composites are described. The empirical equations and unit cell modeling method, which is utilized to model the mechanical properties of composites, are also described. Mechanical properties and the micro-structure of enamel and dentin are also reviewed. Current approaches in modeling the mechanical properties of the two natural bio-composites have been reviewed. This lays down the fundamental knowledge to determine the anisotropic mechanical responses of enamel and dentin using the hierarchical method. In addition, the advanced digital image technology, CT scanning, is reviewed in regard to its application in dental study. The basic theory of finite element analysis is also described.

In Chapter 3, the mechanical properties of a dental composite are predicted. Application of the CAD-based method on the construction of multi-phase unit cell models with various morphologies and volume fractions of the particle phases has been presented. With the use of these cell models and consideration of interfacial debonding, the micro-damage mechanism of the composite is predicted, with a discussion of the stress distribution and concentration. Regarding macro-structural mechanical behavior, the effects of various particle morphologies and volume fractions on the elastic modulus, stress-strain relations, and tensile strength are also predicted.

Chapter 4 presents the two proposed methods in determining the mechanical properties of enamel and dentin in the micro-scale and the macro-scale. In the micro-scale, a method which integrates nanoindentation, finite element modeling, and artificial neural network techniques to determine the elastoplastic isotropic constitutive relation of constituents of enamel and dentin is described. Based on these determined properties and the hierarchical structure of enamel and dentin, the unit cell modeling method is adopted to determine the anisotropic mechanical properties of enamel and dentin in the macro-scale are presented.

Chapter 5 demonstrates the proposed method to create a 3D assembly FE model based on 2D CT images. The assembly model comprises a mandible and a triphasic tooth model, i.e. enamel, dentin and pulp, in which the tooth model is restored virtually with a Class II MO restoration under the CAD environment. The restoration material, enamel, and dentin are assigned using the determined material properties. Stress analysis and failure prediction of dental restoration are described.

Chapter 6 contains the conclusions and the statement of originality. Future research work is also suggested. Preliminary work has been conducted on part of the future work and a brief discussion is also presented.

Chapter 2. Literature Review

2.1. Categories of Restoration Materials

Various materials have been adopted for restoration applications. In general, they can be classified into two major categories, metallic fillings and tooth colored dental composites.

In the metallic fillings category, silver amalgam has been extensively used restoration material for the repair of decayed teeth. However, investigations have demonstrated that there are three primary disadvantages in using this conventional material. Firstly, silver amalgam does not bond properly with the remaining teeth (Philips, 1991), and bacteria may have the chance to penetrate the space between the tooth and the filling. Such phenomenon is termed as microleakage. Once it happens, the tooth-brushing process can no longer completely remove the bacteria, and their metabolic activity leads the tooth to decay extensively, known as secondary caries. The patient may feel pain as the caries develop close to the pulp. Secondly, because amalgam does not adhere to the tooth properly, the dentist has to make a cavity that allows the mechanically retaining of the hardened metallic filling for repairing a tooth lesion. This means that a cavity with a small access and large volume is incised. This process not only removes decayed living tissue along with healthy tissue, but it also weakens the remaining structure of the tooth. Finally, it is due with the potential hazard issue of using silver amalgam as restoration material. Debate on such issue was initiated since this material was introduced. Some research studies have raised safety concerns by demonstrating the chronic release of mercury vapor from amalgam fillings during chewing and brushing (Osorio et al., 1995).

Tooth colored particulate reinforced dental materials are now being increasingly adopted as filling materials to replace conventional amalgam restorations. This is due to the aesthetic advantage and not representing a potential toxic hazard. Tooth colored restoration materials can be subdivided into three categories, i.e. resin composites, glass ionomers and compomers.

A resin composite is characterized by its mechanical properties being comparable to dental amalgams and its capability of rapid polymerization in the presence of oxygen and water (Sideridou et al., 2003). In addition, they are aesthetically attractive materials, translucent in nature, have colors to match the variation of shades of natural teeth and have the ability to maintain color stability. Compositions of resin composite dental materials involve inert glass particles and resinous monomers. Glass particles are usually coated with a polymerizable layer since they are inert in nature. Such action is critical to facilitate better transfer of stress from the matrix phase to the particle, so as to ensure a composite with a better strength value. This is done through enabling the establishment of chemical adhesion bonding between the two phases during the curing process. Through the curing process, a resin composite is formed by joining the monomer molecules together into a cross-linked network with the reinforcement of the glass particles.

Glass ionomers were introduced in mid-1970 by Wilson and Kent (1971). They have since been extensively used in the restorative dentistry field. Compositions of glass ionomers include water soluble acidic polymers and glass powders. Regarding acidic polymers, both poly(acrylic acid) and acrylic/maleic acid are commonly used (Wilson and McLean, 1988). For glass particles, strontium and calcium aluminofluorosilicates are widely used (Hill and Wilson, 1988). Setting of glass ionomers involves acidic polymers,

water and acid soluble glass particles. The acidic polymer here performs with a non-cross linked status. In the mixing process, glass particles dissolve in the acidic solution and fluoride is released. Setting of conventional glass ionomers is done through the neutralization process, which includes the formation of strontium or polyacrylate and aluminium polyacrylate. Glass ionomers possess fluoride releasing characteristics since they are made of fluoride-containing glass. During the setting process, part of the fluoride transfers to the matrix phase. It is believed that the release of fluoride originates from the matrix. Wilson et al. (1972) have shown that glass particles also release fluoride into neutral water. Besides the fluoride releasing capability, a glass ionomer is also characterized by its capability in forming a natural adhesive bond to enamel and dentin (Tyas, 2003).

In the early 1990s, polyacid-modified resin composites were developed, belonging to the category of aesthetic dental material (McLean et al., 1994). It is also named “Compomer”, through the combination of two words, i.e. composite and ionomer. The introduction of compomer aimed at combining the advantages of both glass ionomers and resin composites for the restoration industry (Meyer et al., 1998). A compomer is a cross product of a resin composite and glass ionomer, having the composition of reactive fluoride glass and the monomer as well as acid. The monomer used for compomer comprises both the acidic groups of glass ionomer and the polymerizable groups of a composite resin. Curing of the compomer system involves two stages. In the first stage, with the presence of blue light at 470nm, monomers are polymerized via their methacrylate groups (Meyer et al., 1998). The polymerization process has been observed to carry on at a slow rate for up to 60 hours after switching off the light (Young et al.,

2004). The degree of polymerization $D_{polymerization}$ can be expressed using the equation below:

$$D_{polymerization} = \alpha_1 + \alpha_2 \ln t \quad (2.1)$$

where α_1 and α_2 are material constants and t is time. In stage two, with the presence of water, a reaction similar to glass ionomer curing takes place, fluoride is released and further polymer cross-links are established.

Tooth colored particulate reinforced composites are now increasingly adopted as restoration materials to replace the conventional amalgam fillings. Regarding types of restoration materials, the compomer is characterized by good aesthetic appearance and acceptable mechanical properties. Moreover, its low shrinkage effect and fluoride releasing capability can inhibit the growth of bacteria which favor the formation of secondary caries. Consequently, the chance of failure for restoration can be lowered. Thus, the compomer seems to be the preferred restoration material for future development.

2.2. Mechanical Properties and Failure of Dental Composites

Among the three categories of tooth color restoration materials, the resin composite has the major disadvantage of polymerization shrinkage after the curing process (Feilzer et al., 1987; Kemp-Scholte and Davidson, 1990; Davidson and Abdalla, 1993; Kinomoto, 1999; Dauvillier, 2000; Pereira et al., 2008). The shrinkage volume ranges from 1.5% to 3% (Dauvillier, 2000), and the restrained contraction induces stresses. Instead of having an

adverse effect on the adhesive interface, such type of stress even influences the whole bonding of the restoration. Although shrinkage stress can be relieved through the sorption of water (Bastioli et al., 1990; Oshida and Gorthy, 1999; Martin et al., 2003), this is not an immediate process. In the interim period, the restored tooth is deformed by the composite and the range of deformation has been identified as being from 2 μm to 47 μm (Suliman et al., 1993). In a severe case, the induced stresses can exceed the strength values of the adhesive material and cause damage (Feilzer et al., 1987). Much work has been performed to explore methods of reducing the interfacial stress (Kemp-Scholte and Davidson, 1990; Davidson and Abdalla, 1993; Kinomoto, 1999; Dauvillier, 2000). This was done through the usage of low modulus composites or the introduction of flexible adhesive linings. It has been observed that such stresses can be released. However, using low modulus composite materials is not applicable to load bearing regions. Restoration fillings are required to be strong, which implies that a high modulus is needed (Davidson, 1986). Fluoride is a well-known anti-caries agent. However, resin composites do not comprise any fluoride compound and thus are not capable of releasing fluoride. Many research works and experimental studies have pointed out that the use of fluoride releasing restoration materials can lessen the formation of secondary caries (Zimmerman et al., 1984; Jensen et al., 1991; Griffin et al., 1992; Gomez and Donly, 1994), which explains the reason for the extensive usage of glass ionomers and compomers.

Regarding glass ionomers, research findings have suggested that this category of restoration material is less reliable in sealing the margins of enamel than the category of resin composite (Smith and Martin, 1992). This is due to a momentous penetration of dye being observed at the gingival margins in an in vitro study. Despite glass ionomers being

capable of forming a natural bond with tooth materials, microleakage is found at the restoration margins. In addition, glass ionomers have the critical disadvantage of low strength which limits the applications for stress bearing regions (Wilson and McClean, 1988).

Concerning compomer-type restoration materials, they are identified among other restoration materials as being superior in maintaining the bond with the cavity walls (Chen et al., 2003). Experimental study has indicated that the rate of shrinkage can be compensated by the rate of hydrophilic expansion through water up-take, with the net volume change merely 0.5%, compared with typically 2% for resin composite (Dentsply, 2011). With the fluoride releasing capability and acceptable mechanical properties, compomers have been widely adopted for restoration applications. The compomer is a recently developed composite, and to further improve this kind of particulate reinforced dental composite, systematic study with considerations of damages is needed. In general, dental composites behave as elastoplastic materials (Xie et al., 2000; Dentsply, 2011). Table 2.1 lists the mechanical properties of the commonly used dental composite (Xie et al., 2000; Schulze et al., 2003).

Table 2.1: Mechanical properties of the commonly used dental composite (Xie et al., 2000; Schulze et al., 2003)

Dental Composite	Category	Elastic Modulus (GPa)	Flexural Strength (MPa)	Compressive Strength (MPa)	Tensile Strength (MPa)
Ketac-Bond	Glass Ionomer	8.2	11.1	225.7	20.0
α -Silver	Glass Ionomer	6.5	31.4	176.0	18.7
α -Fil	Glass Ionomer	8.2	26.8	196.5	18.2
Ketac-Silver	Glass Ionomer	7.9	22.9	211.8	22.1
Ketac-Fil	Glass Ionomer	8.7	22.6	251.2	25.5
Ketac-Molar	Glass Ionomer	8.8	21.2	301.3	23.8
Fuji II	Glass Ionomer	8.2	26.1	202.0	20.1
Vitremer	Resin-type	6.5	82.1	265.3	47.5
Fuji II LC	Resin-type	6.4	71.1	306.2	44.4
Photac-Fil	Resin-type	5.9	74.4	243.5	37.9
Dyract	Compomer	9.8	-	260.0	35.0

Failure can be regarded as the result of damage accumulation. In particulate reinforced dental composites, damage can be considered from both the micro-scale and the macro-scale.

In the micro-scale, internal damage of particulate reinforced dental composites takes place when mechanical debonding occurs between the reinforcement and the matrix (Gautier et al., 1999; Sakaguchi et al., 2005). To raise the mechanical properties of

restoration composites, a high particle volume fraction is usually involved (Davidson, 1986; Zhang et al., 2007). However, restoration flow is limited. At the macro level, boundaries are formed at the restoration and tooth surfaces. High particle volume fractions constrain the localized area of the matrix. In the case of occlusal loading, high interfacial stress is induced between the matrix and reinforcement at the micro level (Yukitani et al., 1997; Condon and Ferracane, 1998; 2002; Sakaguchi et al., 2005). This is due to the large mismatch of mechanical properties between the matrix and particles.

In the macro view, secondary caries and excessive occlusal loading are the two main causes for the failure of restorations. Forss and Widstrom (2004) conducted a study on 3,455 restoration cases and found that the secondary caries was the most common factor for tooth replacement while excessive occlusal loading was another significant factor. Similar studies have been conducted by various researchers and similar results have been found (Wilson et al., 1997; Mjör 1985, 1997; Mjör et al., 1998, 2000, 2002; Deligeorgi et al., 2001; Sakaguchi, 2005; Sarrett, 2005; Opdam et al., 2007, Drummond, 2008; Frost, 2009; Frencken, 2010). Secondary caries are usually found at the margin of the restoration. Mahler and Engle (2000) claimed that marginal damage is a sign of secondary caries. Goldberg (1990) has also indicated that the risk of secondary caries can be lessened by reducing the chance of committing marginal damage. In 2003, Hayashi and Wilson (2003) conducted an analysis and found that restorations with marginal degradation at year 3 were more likely to fail in year 5 when compared to those without degradation at year 3. There are many factors that can induce marginal degradation. Experimental studies have revealed that bacteria, restoration shrinkage and mechanical loading affect the integrity of the margin (Davidson and Abdalla, 1994; Baran et al., 2001;

Ferracane and Mitchem, 2003, Sakaguchi et al., 2005) and induced stresses cause the failure of restorations. With the introduction of the compomer dental material, having fluoride releasing capability and minor shrinkage effect, excessive mechanical loading becomes an important factor for restoration committed marginal damage. Composite restoration materials have a mechanical properties disparity problem with hard tooth tissues, enamel and dentin (Pereira et al., 2008). During mastication, this disparity problem leads to the concentration of stress on the restoration which may result in failure (Davidson, 2000; Shor et al., 2003; Li et al., 2011).

2.3. Mechanical Modeling and Failure Prediction of Composites

Most of the currently available dental composites are particulate reinforced composites. Empirical equations and unit cell modeling methods have been developed and extensively utilized to model the mechanical behavior of particulate reinforced composites.

Empirical equations are often used to calculate the elastic modulus E and tensile strength S of composites. Concerning elastic modulus, Brodnyan (1959) has proposed the equation below to take into account a composite comprising non-spherical particles:

$$E = E_m \left[\exp\left(\frac{2.5 \phi_p + 0.407 (R_p - 1)^{1.508} \phi_p}{1 - s \phi_p}\right) \right] \quad (2.2)$$

where E_m , ϕ_p , and R_p are the elastic modulus of matrix, particle volume fraction and the particle aspect ratio, within a range of 1 to 15, respectively. In 1969, Halpin and Tsai

suggested an empirical equation to find the elastic modulus of composites which can account for irregularly shaped particles (Halpin, 1969; Halpin and Tsai, 1969).

$$E = E_m \frac{1+\alpha \beta \phi_p}{1-\beta \phi_p} \quad (2.3)$$

where α and β are composite constants. α is a function of Poisson's ratio of the matrix and particle morphology, while β is a constituents' modulus dependent variable. Based on this equation, Nielsen (1970) proposed another modulus prediction equation:

$$E = E_m \frac{1+\alpha \beta \phi_p}{1-\psi \beta \phi_p} \quad (2.4)$$

where ψ is a particle packing fraction dependent parameter.

Regarding the prediction of tensile strength S , Nielsen (1966) has formulated an equation to predict the strength of a matrix embedded with non-spherical particles a non-linear relationship.

$$S = S_m (1 - \phi_p^{2/3})^\vartheta \quad (2.5)$$

where S_m and ϑ is the matrix strength and a value describing the level of weakness in the composite structure due to the debonding discontinuities for stress transfer respectively. For composite with poorly bonded particles, S has been defined using the equation below (Danusso and Tieghi, 1986; Levita et al., 1989):

$$S = S_m (1 - \phi_p) \quad (2.6)$$

Based on the assumption of strong adhesion bonding, an empirical equation was proposed (Pukanszky et al., 1988; Turcsanyi et al., 1988):

$$S = \left(\frac{1-\phi_p}{1+2.5\phi_p} S_m \right) \exp(\alpha \phi_p) \quad (2.7)$$

where α depends on the particle density, particle surface area and adhesion bonding energy.

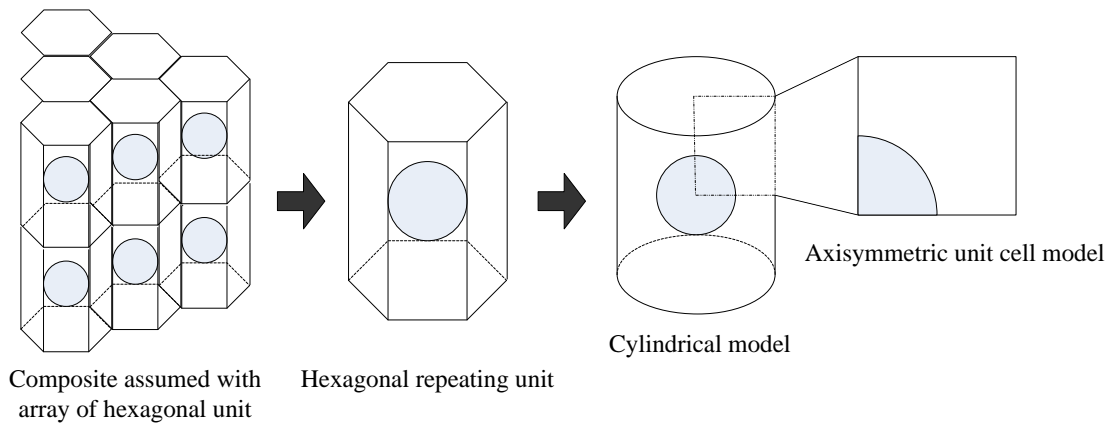


Figure 2.1: The two-dimensional unit cell modeling scheme

In recent years, the unit cell modeling method has been broadly applied to predict the mechanical behavior of particulate reinforced composites. In 1982, Tvergaard has proposed using an axisymmetric cylindrical cell model to predict the mechanical properties of particulate reinforced composites. Particle arrangement in the matrix phase is assumed to be in a hexagonal array. For simplicity, a cylindrical cell was utilized to substitute the hexahedral one, as shown in Figure 2.1. Regarding the repeated and periodic structure, the model was further reduced to a 2D axisymmetric cylindrical cell

model. This model has been widely adopted to investigate the mechanical behavior of particulate reinforced composites (Bao et al., 1991; Zahl and Meeking, 1991; Llorca et al., 1993; Guild and Kinloch, 1994; Kim et al., 2001). In 1992, Bush argued that application of the axisymmetric cylindrical cell model results in a certain degree of inaccuracy and such inaccuracy is enlarged if the particle volume fraction exceeds 40%. This is due to the prior assumption of substituting hexagonal repeating units by cylindrical unit cells, leading to the introduction of a cubic unit cell model. A 3D cubic unit cell model is based on the assumption that particles are evenly distributed in the composite system, as illustrated in Figure 2.2. Packing of the particles is assumed in a cubic array. Due to symmetry, one-eighth of the cubic model is utilized for the unit cell model representation. The 3D cubic unit cell model has also been broadly used to study the mechanical responses of particulate reinforced composites (Wu and Dong, 1995; Guild and Bonfield, 1998; Balać et al., 2001). Application of either the 2D or 3D unit cell models can be extended to model the damage mechanism of composite systems.

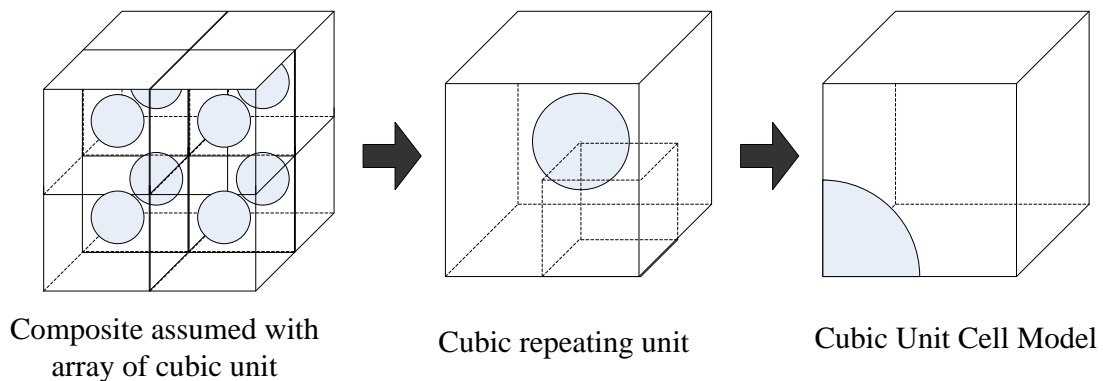


Figure 2.2: The three-dimensional unit cell modeling scheme

Accumulation of damage causes failure. In numerical modeling, three types of damage criteria are usually used, energy-based, strain-based, and stress-based. The concept of the energy-based criteria is that damage occurs when the elastic energy released is equal to or larger than the surface energy limit of the material. Luccioni et al. (1995) and Oller et al. (1995) have suggested the use of energy-based criteria for modeling damage of brittle materials. Toledo et al. (2008) have adopted an energy-based criteria to predict the mechanical responses of composites before failure. For the strain-based criteria, damage is induced once a targeted strain value is larger than a threshold value. The strain-based criterion is deemed suitable for modeling damage in porous materials (Ghosh et al., 2001). His study has tracked the incidence and propagation of micro-structural damage in porous materials. Similarly, for the stress-based criteria, damage is initiated if a targeted stress value (can be hydrostatic stress or a principal stress) exceeds a threshold value. Ghosh and Moorthy (1998) have suggested the adoption of the maximum principal stress criteria to model the damage involved in brittle particulate materials. Fan et al. (2004a) have proposed using radial stress while Tsui et al. (2004; 2005; 2006) have proposed the use of hydrostatic stress as the criterion for damage criteria of the interphase region of composites between the particle and matrix. Moreover, Dejak and Mlotkowski (2008) have adopted stress-based criteria for the failure modeling of dental restorations.

A review of the empirical equations has highlighted the importance of three factors affecting the mechanical behavior of particulate reinforced composites, particle volume fraction, particle morphology, and interfacial adhesion. Although extensive empirical equations have been proposed, with consideration of various factors, empirical equations cannot generate stress-strain relations for composites which are partially debonded. To

deal with such limitations, the unit cell modeling method can be adopted. Empirical equations can offer material scientists an idea of the tendency change of material properties, while numerical approaches offer a platform to consider the effect of these factors on the mechanical stress-strain behavior of composite systems. Knowledge of such behavior is important for the systematic design of dental composites with desired properties. Consequently, the development of new particulate reinforced composites can be facilitated. A review of the current unit cell modeling methods has found that most of the cell models comprise spherical particle phases packed under simple cubic architecture. For most of the dental composites, particles are non-spherical in shape with high particle volume fractions (Gu et al., 2004; Dentsply, 2011). In the current dental industry, glass powders being employed in most of the restoration materials are obtained using glass milling technology. Since such technology is a robust process, glass powders are usually non-spherical in shape. In addition, simple cubic packing architecture offers a low particle packing efficiency which is not suitable for investigations involving high particle volume fractions. Thus, in using the unit cell modeling method to predict the mechanical behavior of dental composites, these two factors should be taken into account. Moreover, internal debonding damage should also be considered.

2.4. Mechanical Properties of Enamel and Dentin

The experimental obtained elastic moduli for enamel and dentin have been summarized and plotted in Figure 2.3 (Craig et al., 1961; Reich et al., 1967; Staines et al., 1981; Habelitz et al., 2001, 2002; Ge et al., 2005; Park et al., 2008; Roy and Basu, 2008) and

Figure 2.4 (Craig and Peyton, 1958; Tyldesley, 1959; Bowen and Rodriguez, 1962; Renson, 1970; Renson and Braden, 1971; Watts et al., 1987; Huang et al., 1992; Van Meerbeek, 1993; Sano et al., 1994; Habelitz et al., 2002; Bechtle et al., 2010) respectively.

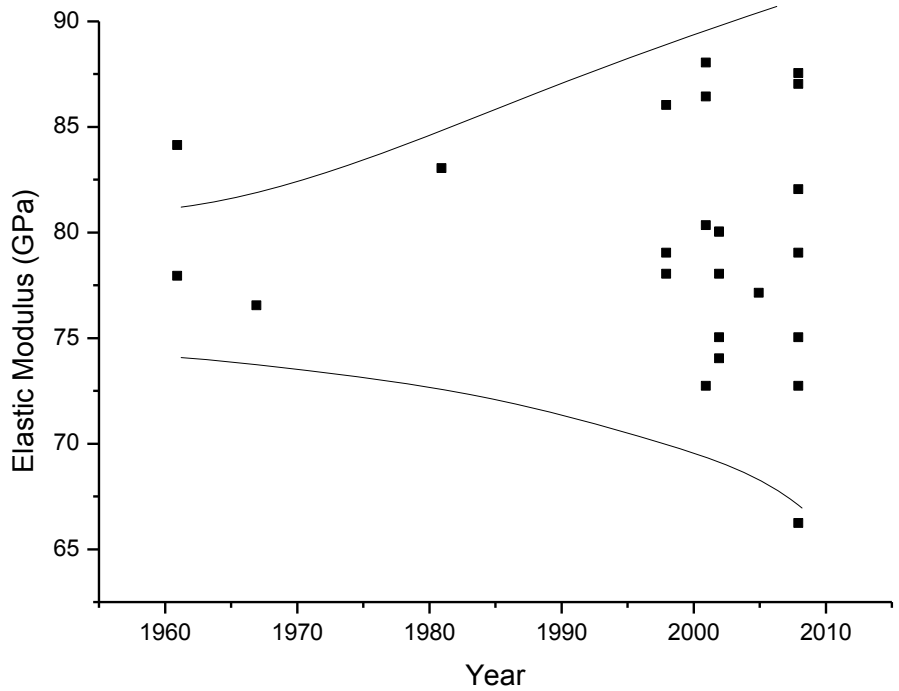


Figure 2.3: The reported elastic modulus of enamel from the literature

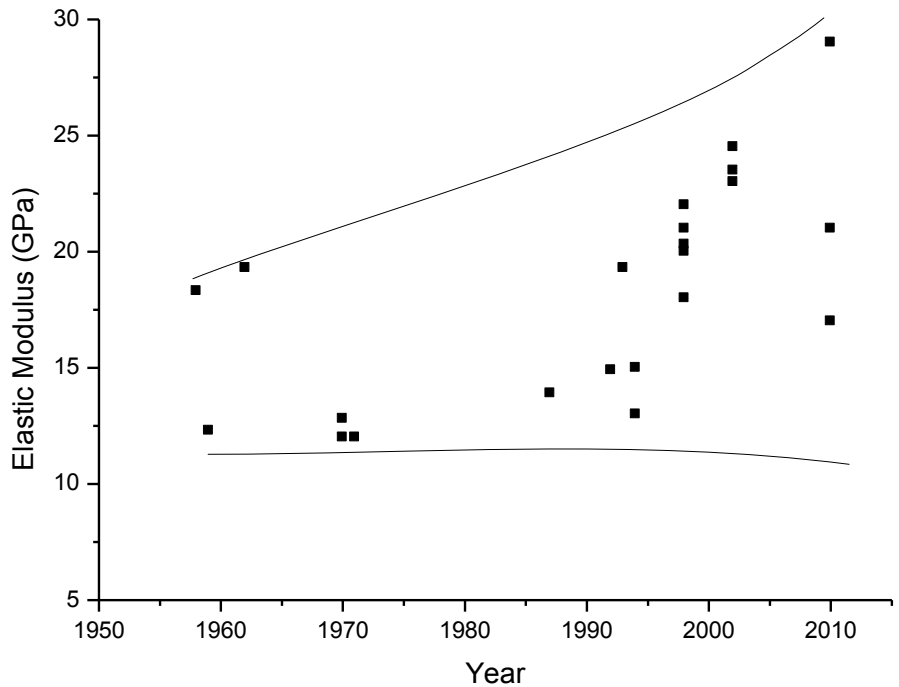


Figure 2.4: The reported elastic modulus of dentin from the literature

For enamel, before 1992, conventional testing techniques, such as tensile, compression and bending tests, were used to measure the elastic modulus. A great inconsistency in the elastic modulus persisted and ranged from 76.5GPa to 84.1GPa. For dentin, similarly, elastic moduli were measured using conventional mechanical testing methods. A wide discrepancy ranging from 12.0GPa to 19.3GPa was observed, which reveals similar problems in carrying out conventional mechanical tests on small specimens. After 1992, microindentation and nanoindentation testing techniques have become the dominant methods to measure the elastic modulus for both enamel and dentin. In spite of the marked advances in both the improved testing techniques and the theoretical knowledge

of the mechanics of composite structures, the great inconsistency in the elastic modulus persisted.

Although enamel and dentin have long been considered brittle and hard materials, evidence from recent research work has indicated that both these natural bio-composites undergo plastic mechanical behavior (Nalla et al., 2003; He and Swain, 2007a,c; Ang et al., 2009). For enamel, He and Swain (2007a,c) carried out a nanoindentation experiment and presented a plot of hardness versus contact radius divided by the indenter radius, using an indenter with a spherical tip. Based on the presumption from Tabor (1951), who has claimed that there is a certain degree of equivalence between the plotting of hardness versus ratio of contact radius and spherical indenter radius, and the conventional stress-strain curves, enamel has been observed as having plastic mechanical behavior. For dentin, Nalla et al. (2003) conducted a double-notched four-point bending test with various loadings on dentin, and an apparent yield point and post-yield behavior have been observed.

Over the 60 years, with the application of advancing testing techniques, it was expected that the experimentally obtained elastic modulus would converge to a certain value. However, an increasing spreading trend is observed for both the enamel and dentin. The spreading tendency can be substantially described using the variation between the maximum and the minimum values. Enamel gives a variation value of 21.8GPa and 16GPa for the case of dentin. Park et al. (2008) conducted experimental studies on the effect of aging on the elastic properties of enamel, it was observed that the differences in values between the age groups, ($18 \leq \text{age} \leq 25$) and ($50 \leq \text{age}$), was 7.30GPa. Similarly, Arola and Repogel (2005) found that the value difference of dentin between 17-year old

and 77-year-old patients was 1.40GPa. Thus, aging would not appear to be the major factor leading to the wide spreading tendency. The other possible reason is that both enamel and dentin exhibit heterogeneity at the micro-scale. Most of the current research work in modeling enamel and dentin makes the assumption that they have elastic and isotropic behavior (Ichim et al., 2007a,b; Magne, 2007; Lin et al., 2008a,b; Jiang et al., 2010; Li et al., 2010). This is due to the lack of elastoplastic anisotropic mechanical parameters in describing their behavior in bulk. One of the success factors in dental modeling depends on the accuracy in defining material properties (Hasegawa et al., 2010). Therefore, a method which can determine the anisotropic elastoplastic mechanical properties of enamel and dentin is in demand. To do so, it is necessary to understand their micro-structures, which are reviewed in the next section.

2.5. Micro-structure of Enamel and Dentin

At the micro-structural hierarchy, enamel is composed of rod and interrod constituents (Ge et al., 2005), as shown in Figure 2.5. It can be observed that the diameter of the rod is about 5 μ m, and is encapsulated by the interrod constituent with a thickness of about 1 μ m (Simmelink, 1987; He et al., 2007b). Rods are parallel to each other and perpendicular from the dentin-enamel junction (DEJ) to the occlusal enamel surface. Both the rod and interrod constituents comprise long and closely packed ribbon-like carbonated apatite crystals (Frazier, 1968). These crystals are roughly hexagonal in cross section with a thickness of about 25-30nm and width of about 60-70 nm (Kerebel et al., 1979). Regarding the length of the crystal, different research reports give different values.

Orams et al. (1974) have tried to explain such observation in two ways. The first one is due to the sample preparation difficulties and the second one is that the true length of the apatite crystals is too long to be determined. A current study suggested the length of crystals to be equal to the entire thickness of the enamel layer (Nanci, 2003). It is also suggested that there is an ~1nm thin film of protein sticking the crystals together.

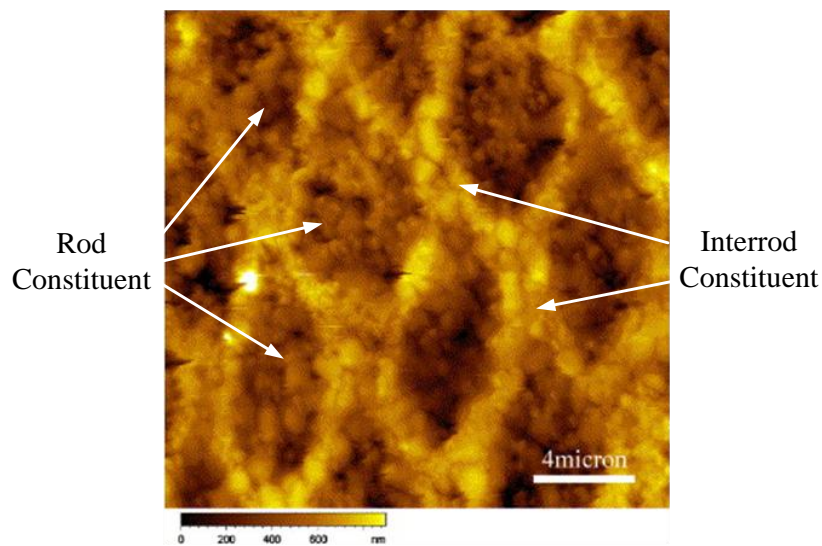


Figure 2.5: AFM image of enamel surface (Ge et al., 2005)

At the microscopic level, dentin can be regarded as a composition of two constituents according to their mineral level, i.e. peritubular and intertubular constituents (Mjör and Fejerskow, 1986; Kinney et al., 1993). As shown in Figure 2.6, the peritubular constituent surrounds the tubule. The tubule is a fluid-filled, circular hollow cylinder. The intertubular constituent takes over the volume exterior to the peritubular constituent. The intertubular constituent is differentiated with the peritubular one by less mineral but more

collagen content. Collagen in dentin refers to type I collagen fibril. The fibrils are oriented randomly in a plane perpendicular to the direction of the dentin formation and have a diameter of about 50 to 100 nm (Jones and Boyde, 1984). Mineral in dentin is mainly in the form of hydroxyapatite and has a thickness of roughly 5 nm, which is invariant with location (Frank and Nalbandian, 1989). The shapes of the mineral crystallites are observed to have a transformation from plate-like to needle-like along the dentin region from the DEJ to pulp (Kinney et al., 2001a,b).

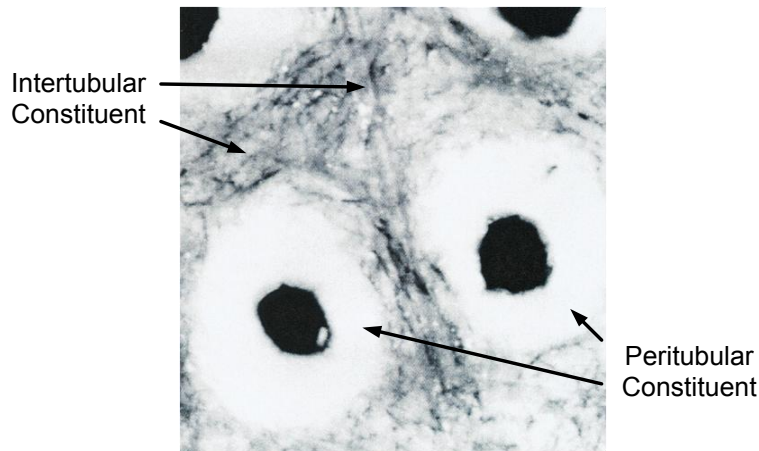


Figure 2.6: AFM images of dentin (Kinney et al., 1993)

2.6. Mechanical Modeling of Enamel and Dentin

Although enamel and dentin are anisotropic materials, both the natural biomaterials in the applications of tooth modeling are usually assumed to be elastic isotropic materials (Ichim et al., 2007a,b; Magne, 2007; Lin et al., 2008a,b; Lin et al., 2009; Jiang et al., 2010; Li et al., 2010). This is due to the lack of mechanical parameters describing their

elastoplastic anisotropic behavior. In the restoration industry, such oversimplification affects the understanding of how mastication loading is spread over a restored tooth. Consequently, this lowers the accuracy in predicting the failure of restoration. To determine the anisotropic elastoplastic mechanical behavior of enamel and dentin, any study needs to start from their complex hierarchical structures. However, very few attempts can be found that examine their mechanical properties from a micro to macro scale.

In 1971, Katz expressed that the differences in structural and chemical composition of enamel affect the measured elastic modulus value. Katz's idea gives a better understanding of the discrepancies of experimentally obtained elastic modulus values. When force is exerted across the mineralized crystal rod orientation, a large portion of the force is borne by the low stiffness organic interrod tissue. The measured elastic modulus value is low. In contrast, force is borne by the high stiffness crystal when exerted along the crystal rod. The measured elastic modulus value is high. Further research has suggested calculating the elastic modulus of the enamel composite using the equivalent strain equation (Ashby and Jones, 1980).

For the elastic modulus E_{\parallel} along the crystal rod orientation,

$$E_{\parallel} = \phi_{rod} E_{rod} + (1 - \phi_{rod}) E_{interrod} \quad (2.8)$$

where ϕ_{rod} is the volume fraction of enamel occupied by the crystal rod.

For the elastic modulus E_{\perp} across the crystal rod orientation,

$$E_{\perp} = \frac{1}{\phi_{rod} / E_{rod} + (1 - \phi_{rod}) / E_{interrod}} \quad (2.9)$$

Similarly, Hashin (1983) and Qin and Swain (2004) have tried to estimate the elastic modulus of dentin through its constituent properties at the microscopic level using bounding models, such as Hashin-Shtrikman and Voigt and Reuss. Through using the bounding principles, the elastic modulus of dentin is approximated using the relative volume fractions of the mineral and collagen phases. Such models have been categorized as worth little due to the mineral and collagen phases deviating by several orders of magnitude. In addition, the use of the upper and lower bounds is only a validity check of experimental values and there is no definite relation that the measured values should lie within the average of the wide bounds. Thus, an accurate elastic response of dentin still cannot be described, even when the elastic modulus is calculated through averaging the upper and lower bounds of the elastic parameters.

In 1997, Spears investigated the anisotropic elastic properties of enamel through a prism shaped model using finite element analysis. For dentin study, Christensen (1990) proposed a mechanics model suitable for micro-structural level consideration. The model considers a homogeneous matrix with a cylindrical inclusion. Huo and Zheng (1999) built a micromechanical model of dentin while Kinney et al. (1999) extended Christensen's micromechanics model to estimate the elastic parameters of dentin in the form of analytical expressions. Huo (2005) has also utilized an analytical approach to create a constitutive model to describe the elastic properties of dentin in terms of transverse isotropy.

Few publications can be found for the mechanical modeling of enamel and dentin. These models only examine the elastic behavior of enamel and dentin but not the plastic behavior. One of the critical reasons is due to the lack of information about the plastic

behavior of their micro-constituents. In the view of material science research, quantifying the elastoplastic response of specimens of small size has been characterized as a difficult problem for a long time. However, such lack of information can hardly allow an accurate description of the mechanical behavior of a tooth overall. Thus, a novel method which is capable of identifying the elastoplastic parameters of small materials is needed.

2.7. CT-based Solid Modeling in Dental Research

Ethical concerns limit the laboratory studies on living subjects. Advanced digital imaging technology has opened up new possibilities in dentistry. The computational simulation method takes a more important position in both clinical and therapeutic applications of the dental industry (Ausiello et al., 2002). Usage of virtual models offers an alternative way of investigation, and cost can also be reduced for in vivo and in vitro experiments.

In dental research, CT scanning is the most frequently used high resolution imaging technology. To conduct CT scans, the targeted object needs to be exposed to a certain amount of ionizing radiation; the absorbed radiation is detected and imaged later on. A series of sliced 2D images depicting a density map of the scanned object can be obtained. Piling these images creates a 3D description of the scanned area. The development of CT technology has been used to study and quantify the morphology of bone (Boyd et al., 2006; Hulme et al., 2007), to non-destructively evaluate porous biomaterials (Lacroix et al., 2006), and to investigate the architecture of scaffolds (Ho and Hutmacher, 2006; Malafaya et al., 2008). Offering reasonably high resolution is the main reason for using CT as imaging technology in the field of hard tissue engineering. Contrast segmentation

is a technique used for tissue differentiation, in which the grayscale of the layered contour images is determined by the tissue density. Living tissues involve complex shapes, such as teeth and mandibles, are possible to be digitized using CT scanned images to allow accurate measurement of small changes of irregularities (Rudolph et al., 2006). Ulusoy and Darendeliler (2008) have evaluated the effects on the stress distribution with different types of Class II activator using a mandible FE model constructed using CT scanned images. Bujtár et al. (2010) have digitized the mandibles of patients of different ages using CT scanned images, and performed analyses with the simulation of supra normal chewing forces. Gao and Chae (2010) have proposed a tooth segmentation method to visualize a tooth from CT images so as to provide assistance for dentists performing orthodontic treatment and surgery.

Despite the availability of the advanced imaging technology, dental research has made far from expectation. Ichim et al. (2007a) have modeled the fracture behavior of restoration using 2D FE model constructed using CT scanned images. Magne (2007) has demonstrated the use of Boolean operations to build up a 3D tooth model with desired restoration morphologies using CT images. In contrast, Lin et al. (2008a,b) have used a 3D tooth model constructed manually, according to the literature data describing the morphology of teeth, to examine the effect on changes in cavity dimensions and various factors on the mechanical response of restoration during oral temperature changes. In 2010, Li et al. have constructed a 2D FE model from scanned images for optimizing the shape of the restoration cavity. Li et al. (2011) have used scanned images to construct a 2D FE model for the simulation of debonding and fracture of a restored tooth.

Concerning the failure prediction of restorations, in the majority of cases, application of the advanced scanning technology is limited to constructing FE tooth models in 2D rather than 3D. The major reason is due to the 3D surface model obtained from the imaging technology being unfavorable in creating a simulation model according to the study interest of particular researchers. Although Boolean operations have been successfully demonstrated for creating tooth models with desired restorations, it is not an efficient and effective approach. The involved mesh model was created based on STL file format, which stores data describing the morphology of the designated tissue in the form of small triangular facets. Small facets may already involve high aspect ratios or sharp angles which would hinder the mesh generation process in creating the FE model. Even a FE model can be generated successfully; tetrahedral elements can be easily subjected to excessive distortion which would cause the analysis to abort. Performing Boolean operations would partition these facets further. Consequently, a higher chance for the model would involve geometry with high aspect ratios and sharp angles, as well as the status of excessive distortion during FE analysis. If any of the mentioned conditions is encountered, the processes involved for realizing the 3D surface model need to be redone from the geometry acquisition process based on the 2D scanned images. Such cycle can be stopped until the model can conduct FE analysis successfully. It is a time-consuming task if a researcher aims to optimize the design of a restoration, where continuous modifications of the parameter are required. As a result, to facilitate the conduction of research in the dental field, an efficient and effective method to build up a CT-based FE model with modification capability is needed.

2.8. Finite Element Theory

FE analysis was theoretically introduced by Turner et al. (1956) and has been applied for structural-mechanical analysis extensively. The FE method is characterized as a stress analysis technique which is capable of determining the overall displacement and stress of an object model. This is done through dividing the model into a finite numbers of elements and performing a dynamic equilibrium calculation among the elements.

To simulate the damage and failure of dental composites at the micro- and macro- scales, removal of the elements is needed. Thus, implicit finite element theory has not been chosen in this study. This is due to the global stiffness matrix being unable to be created under the condition of element deletion. To perform the analysis, the explicit finite element theory has been employed.

Under the explicit finite element theory (Abaqus, 2008), the strain-displacement relation can be considered as linear when small strain is involved. Following the Lagrangian formulation, each element in the analytical model is defined with strain vector, virtual strain vector, and strain-displacement relation. The displacement at a specific instantaneous time is determined through the dynamic equilibrium equations. According to dynamic equilibrium, the total internal virtual work is equivalent to the total external virtual work at time t as follows (Owen and Hinton, 1982):

$$\int_{\Omega} [\delta \boldsymbol{\varepsilon}_t]^T \boldsymbol{\sigma}_t d\Omega = \int_{\Omega} [\delta \mathbf{u}_t]^T [\mathbf{P}_t - c_t \dot{\mathbf{u}}_t - \rho_t \ddot{\mathbf{u}}_t] d\Omega + \int_{\Gamma_s} [\delta \mathbf{u}_t]^T \mathbf{T}_t d\Gamma \quad (2.10)$$

where Ω is a domain bounded by Γ_s and Γ_u . The displacement vector \mathbf{u} is applied on Γ_u while the surface traction vector \mathbf{T} is specified on Γ_s . Regarding the other variables, $\boldsymbol{\sigma}$, \mathbf{P} ,

c , ρ , $\dot{\mathbf{u}}$, and $\ddot{\mathbf{u}}$ are the stress vector, applied body force vector, damping parameter, mass density, velocity vector, and acceleration vector respectively. In the finite element representation, the displacement \mathbf{u} , virtual displacement $\delta\mathbf{u}$, strain vector $\boldsymbol{\varepsilon}$ and virtual strain vector $\delta\boldsymbol{\varepsilon}$ are defined as:

$$\mathbf{u}_t = \sum_{i=1}^n \mathbf{N}_i [\mathbf{d}_i]_t \quad (2.11)$$

$$\delta\mathbf{u}_t = \sum_{i=1}^n \mathbf{N}_i [\delta\mathbf{d}_i]_t \quad (2.12)$$

$$\boldsymbol{\varepsilon}_t = \sum_{i=1}^n \mathbf{B}_i [\mathbf{d}_i]_t \quad (2.13)$$

$$\delta\boldsymbol{\varepsilon}_t = \sum_{i=1}^n \mathbf{B}_i [\delta\mathbf{d}_i]_t \quad (2.14)$$

where i , n , N , B , d , and δd represent the node, total number of nodes, global shape function matrix, strain-displacement matrix, nodal displacement vector, and virtual nodal displacement vector respectively.

A dynamic equilibrium equation for node i at time t can be obtained through substituting equation (2.11), (2.12), (2.13), (2.14) into (2.10) as follows:

$$[\mathbf{F}_i^R]_t = [\mathbf{F}_i^B]_t + [\mathbf{F}_i^T]_t - [\mathbf{F}_i^D]_t - [\mathbf{F}_i^I]_t \quad (2.15)$$

where $[\mathbf{F}_i^R]_t$, $[\mathbf{F}_i^B]_t$, $[\mathbf{F}_i^T]_t$, $[\mathbf{F}_i^D]_t$, and $[\mathbf{F}_i^I]_t$ are the internal resisting forces, consistent forces for the applied body forces, consistent forces for the surface traction, damping forces, and inertia forces. All the mentioned forces can be expressed as below:

$$[\mathbf{F}_i^R]_t = \int_{\Omega} [\mathbf{B}_i]^T \boldsymbol{\sigma}_t d\Omega \quad (2.16)$$

$$[\mathbf{F}_i^B]_t = \int_{\Omega} [\mathbf{N}_i]^T \mathbf{P}_t d\Omega \quad (2.17)$$

$$[\mathbf{F}_i^T]_t = \int_{\Gamma_s} [\mathbf{N}_i]^T \mathbf{T}_t d\Gamma \quad (2.18)$$

$$[\mathbf{F}_i^D]_t = \sum_{j=1}^n [\mathbf{C}_{ij}]_t [\dot{\mathbf{d}}_j]_t \quad (2.19)$$

$$[\mathbf{F}_i^I]_t = \sum_{j=1}^n [\mathbf{M}_{ij}]_t [\ddot{\mathbf{d}}_j]_t \quad (2.20)$$

where $[\mathbf{C}_{ij}]_t$ and $[\mathbf{M}_{ij}]_t$ are the sub-matrices of the damping matrix \mathbf{C}_t and \mathbf{M}_t respectively.

For the displacement vector $[\mathbf{u}^{(e)}]_t$ of an element at time t , it is described as:

$$[\mathbf{u}^{(e)}]_t = \sum_{j=1}^m \mathbf{N}_i^{(e)} [\mathbf{d}_i^{(e)}]_t \quad (2.21)$$

where $\mathbf{d}_i^{(e)}$ and $\mathbf{N}_i^{(e)}$ are the nodal displacement vector and local shape function of an element with m number of nodes.

For an element, the relationship between the strain and nodal displacement is expressed in terms of local strain-displacement matrix $\mathbf{B}_i^{(e)}$ as:

$$[\boldsymbol{\varepsilon}^{(e)}]_t = \sum_{j=1}^m \mathbf{B}_i^{(e)} [\mathbf{d}_i^{(e)}]_t \quad (2.22)$$

The discretized elemental volume $\Omega^{(e)}$ is defined as:

$$d\Omega^{(e)} = \det \mathbf{J}^{(e)} d\zeta d\xi d\eta \quad (2.23)$$

where $\mathbf{J}^{(e)}$ and (ζ, ξ, η) are the Jacobian matrix and iso-parametric element coordinates.

Thus, the dynamic equilibrium equation for a three dimensional iso-parametric element can be obtained through equations (2.16), (2.17), (2.18), (2.19), and (2.20) and the Gauss-Legendre product rules as follows:

$$[\mathbf{F}_i^{R(e)}]_t = [\mathbf{F}_i^{B(e)}]_t + [\mathbf{F}_i^{T(e)}]_t - [\mathbf{F}_i^{D(e)}]_t - [\mathbf{F}_i^{I(e)}]_t \quad (2.24)$$

where the force components can be expressed as:

$$[\mathbf{F}_i^{R(e)}]_t = \int_{-1}^1 \int_{-1}^1 \int_{-1}^1 [\mathbf{B}_i^{(e)}]^T \boldsymbol{\sigma}_t^{(e)} \det \mathbf{J}^{(e)} d\zeta d\xi d\eta \quad (2.25)$$

$$[\mathbf{F}_i^{B(e)}]_t = \int_{-1}^1 \int_{-1}^1 \int_{-1}^1 [\mathbf{N}_i^{(e)}]^T \mathbf{P}_t^{(e)} \det \mathbf{J}^{(e)} d\zeta d\xi d\eta \quad (2.26)$$

$$[\mathbf{F}_i^{T(e)}]_t = \int_{\Gamma_s} [\mathbf{N}_i^{(e)}]^T \mathbf{T}_t^{(e)} d\Gamma \quad (2.27)$$

$$[\mathbf{F}_i^{D(e)}]_t = \sum_{j=1}^n [\mathbf{C}_{ij}^{(e)}]_t [\dot{\mathbf{d}}_j^{(e)}]_t \quad (2.28)$$

$$[\mathbf{F}_i^{I(e)}]_t = \sum_{j=1}^n [\mathbf{M}_{ij}^{(e)}]_t [\ddot{\mathbf{d}}_j^{(e)}]_t \quad (2.29)$$

The dynamic equilibrium equation (2.10) at the time step t can also be expressed as,

$$\mathbf{M} \ddot{\mathbf{d}}_t + \mathbf{C} \dot{\mathbf{d}}_t + \mathbf{K} \mathbf{d}_t = \mathbf{F}_t^{BT} \quad (2.30)$$

where $\ddot{\mathbf{d}}_t$, $\dot{\mathbf{d}}_t$, and \mathbf{d}_t are the global vectors of nodal accelerations, velocities and displacement at the time t respectively. \mathbf{M} , \mathbf{C} , \mathbf{K} , and \mathbf{F}_t^{BT} are the global mass matrix, damping matrix, stiffness matrix, and global vector of the body loads.

Generally, the central difference approximation does not need to be concerned with the convergence problem, so it becomes the main technique in the dynamic analysis for saving computational time. The accelerations and velocities can be expressed as:

$$\ddot{\mathbf{d}}_t = (\mathbf{d}_{t-\Delta t} - 2\mathbf{d}_t + \mathbf{d}_{t+\Delta t})/\Delta t^2 \quad (2.31)$$

$$\dot{\mathbf{d}}_t = (-\mathbf{d}_{t-\Delta t} + \mathbf{d}_{t+\Delta t})/(2\Delta t) \quad (2.32)$$

To satisfy the computational stability, the time increment (Δt) is limited by a critical value Δt_{cr} as follows:

$$\Delta t \leq \Delta t_{cr} = l_{\min} / \sqrt{\rho(1 - \nu^2)/E} \quad (2.33)$$

Substituting equation (2.31) and equation (2.32) into equation (2.30), the recursions at each discrete time step can be written as:

$$\mathbf{u}_{t+\Delta t} = \mathbf{A}\mathbf{u}_t + \mathbf{B}\mathbf{u}_{t-\Delta t} + \mathbf{P} \quad (2.34)$$

where,

$$\mathbf{A} = (4\mathbf{M} - 2\Delta t^2\mathbf{K})/(2\mathbf{M} + 2\Delta t\mathbf{C}) \quad (2.35)$$

$$\mathbf{B} = (2\Delta t\mathbf{C} - 2\mathbf{M})/(2\mathbf{M} + 2\Delta t\mathbf{C}) \quad (2.36)$$

$$\mathbf{P} = -2\Delta t^2\mathbf{F}_t/(2\mathbf{M} + 2\Delta t\mathbf{C}) \quad (2.37)$$

where \mathbf{A} , \mathbf{B} , and \mathbf{P} are the tensorial coefficients. Thus, the displacement at the time step $t + \Delta t$ is given explicitly in terms of the values at the time t and $t - \Delta t$.

Chapter 3. Mechanical Responses Prediction of Particulate Reinforced Dental Composite

In this chapter, the objective is to predict the mechanical properties of particulate reinforced dental composites with various particle morphologies, particle volume fractions, and consideration of interfacial damage. In addition, the stress concentration, stress distribution, and damage mechanism of the composite in micro-scale are also predicted.

The proposed modeling method is developed based on resembling the FE results in the macro-scale and micro-scale by damage coupling. The macro-scale mechanical properties and damage behavior of the dental restoration material are determined from a micro-cell model. To simulate a realistic structure in a dental composite, a 3D model of randomly distributed particles is required. In this study, as shown in Figure 3.1, a random particle distribution was idealized by arranging the particles in a regular packing pattern. The unit cell method lessens the complication of the problem by making an assumption that the dental composite consists of an array of basic components, each component with the same cell geometry, composition, and material properties. To investigate the effect on the mechanical properties of dental composite particles with high particle volume fractions, representative cells were constructed using body centered cubic (BCC) and face centered cubic (FCC) packing architectures instead of traditional simple cubic (SC) architecture, which has low packing efficiency.

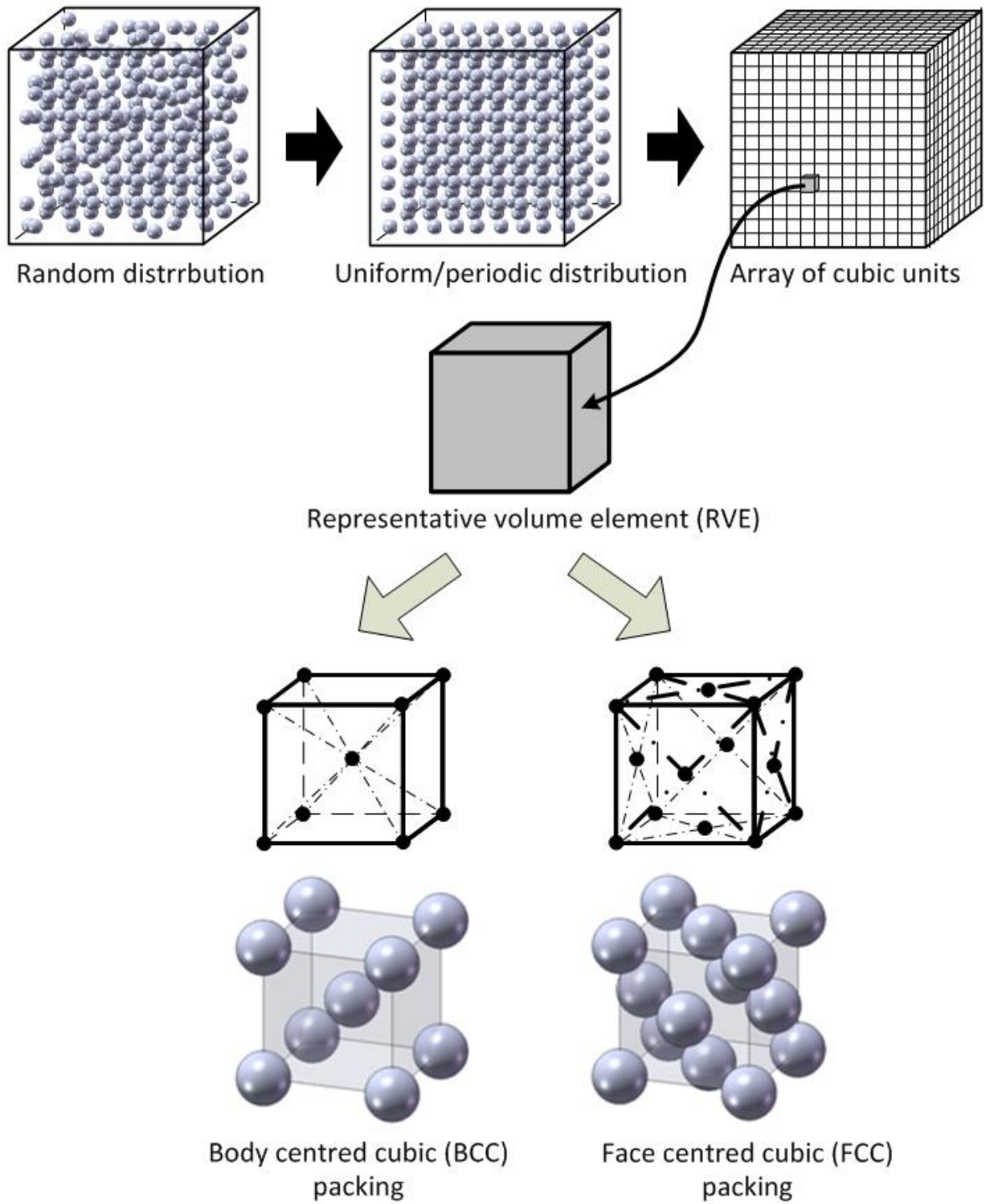


Figure 3.1: Schematic diagram describing different packing systems of RVE

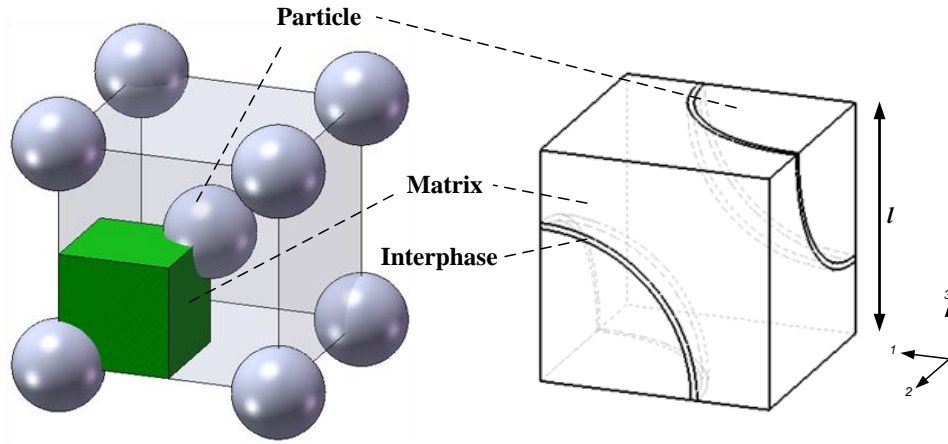


Figure 3.2: Schematic diagram of a unit cell with spherical particles packed in a body centered cubic system

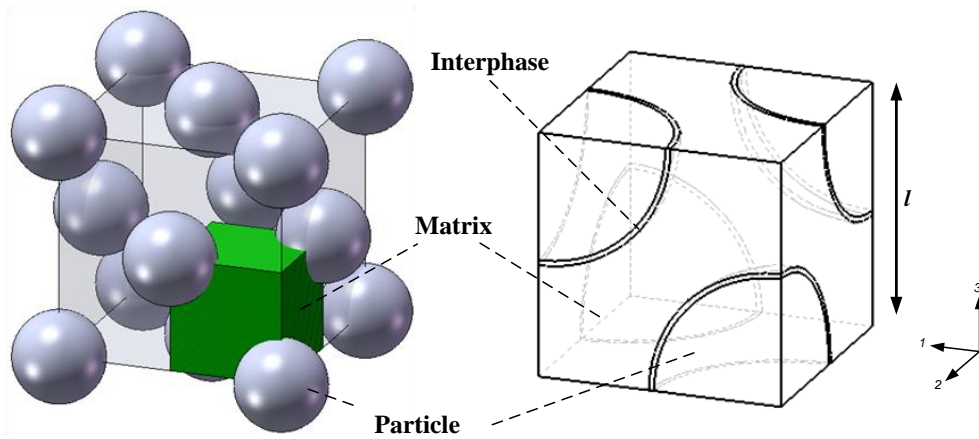


Figure 3.3: Schematic diagram of a unit cell with spherical particles packed in a face centered cubic system

Figure 3.2 and Figure 3.3 describe the cell models with BCC and FCC packing architectures respectively. Assuming the particles have been packed symmetrically and in a cubic array, only one-eighth of the packing, the representative unit cell, is used for analysis. Each unit cell is triphasic, a matrix phase represents the base material; a particle

phase depicts the reinforcement; and an interphase is introduced for modeling the interfacial bonding between the matrix and the reinforcement. The interface layer thickness is defined with a value equals to 1% of the cell length (Wu et al., 2002). The overall damage of the restoration material is considered to be a result of the interfacial debonding damage due to an external load. On application of the FE software (Abaqus 6.8-1) to the heterogeneous mechanistic descriptions of the constitutive behavior of the material elements representing the micro-cell models, the constitutive behavior of the dental restoration composite can be determined. The length scale of the macro- composite structure/micro- unit cell model is about 1000/1 and satisfies the size requirements of the representative volume element (RVE) of a heterogeneous material/structure (Lemaitre, 1992).

3.1. Material Properties and Mechanical Damage Modeling

Recalling the earlier review of dental composites (Section 2.3), compomers are widely used nowadays. In this study, a compomer composite system SrF₂/UEDMA:TCB:TEGDMA was selected. The elastic properties of the composite system are described in Table 3.1. The glass particles are assumed to be purely elastic while the matrix is elastoplastic behavior. Concerning the particle size, the strontium fluoride glass particles inside the compomer composite are claimed, by the manufacturer, Dyract, to have an equivalent spherical diameter value of about 0.8 μ m. The mechanical properties of the interphase are difficult to determine (Lee et al., 2000; Fan et al., 2004b).

The mechanical properties of the interphase are assumed to be the same as those of the matrix stated in Table 3.1, except that it is considered to be damageable.

Table 3.1: Material properties of the compomer composite system

	Elastic modulus (GPa)	Poisson's ratio
Strontium Fluoride Glass (SrF ₂) ^a	89.91	0.25
UEDMA:TCB:TEGDMA ^{b,c}	4.0	0.47

a: (Crystran, 2011); b: (Schulze et al., 2003); c: (Chung et al., 2004)

The interfacial debonding process depends largely on the tensile strength (Tsui et al., 2004; 2005; 2006), therefore, the hydrostatic tensile stress $\bar{\sigma}_H$ failure criterion was adopted for the interfacial elements as follows:

$$\bar{\sigma}_H = \frac{\sigma_1 + \sigma_2 + \sigma_3}{3} \quad (3.1)$$

where σ_1 , σ_2 , and σ_3 are the direct stresses in directions 1, 2, and 3 respectively. Failure of elements in the interface phase is assumed to take place when a critical value σ_c is reached.

3.2. CAD-based Method for Cell Model Construction

To understand the effect of reinforcement geometry on the bulk response of a particulate dental composite, particle morphologies, other than spherical ones, were utilized. To

ensure that the unit cell models have a periodic and repeated structure, three non-spherical particles having a symmetric regular polyhedral geometry of Platonic and Archimedean solids are used (Weisstein, 1999). They are the dodecahedron, truncated octahedron, and cuboctahedron, as shown in Figure 3.4. A dodecahedron is composed of one type of a regular polygon, i.e. pentagon, meeting in identical vertices while each of the remaining two angular particles comprise two types of polygons meeting in identical vertices.

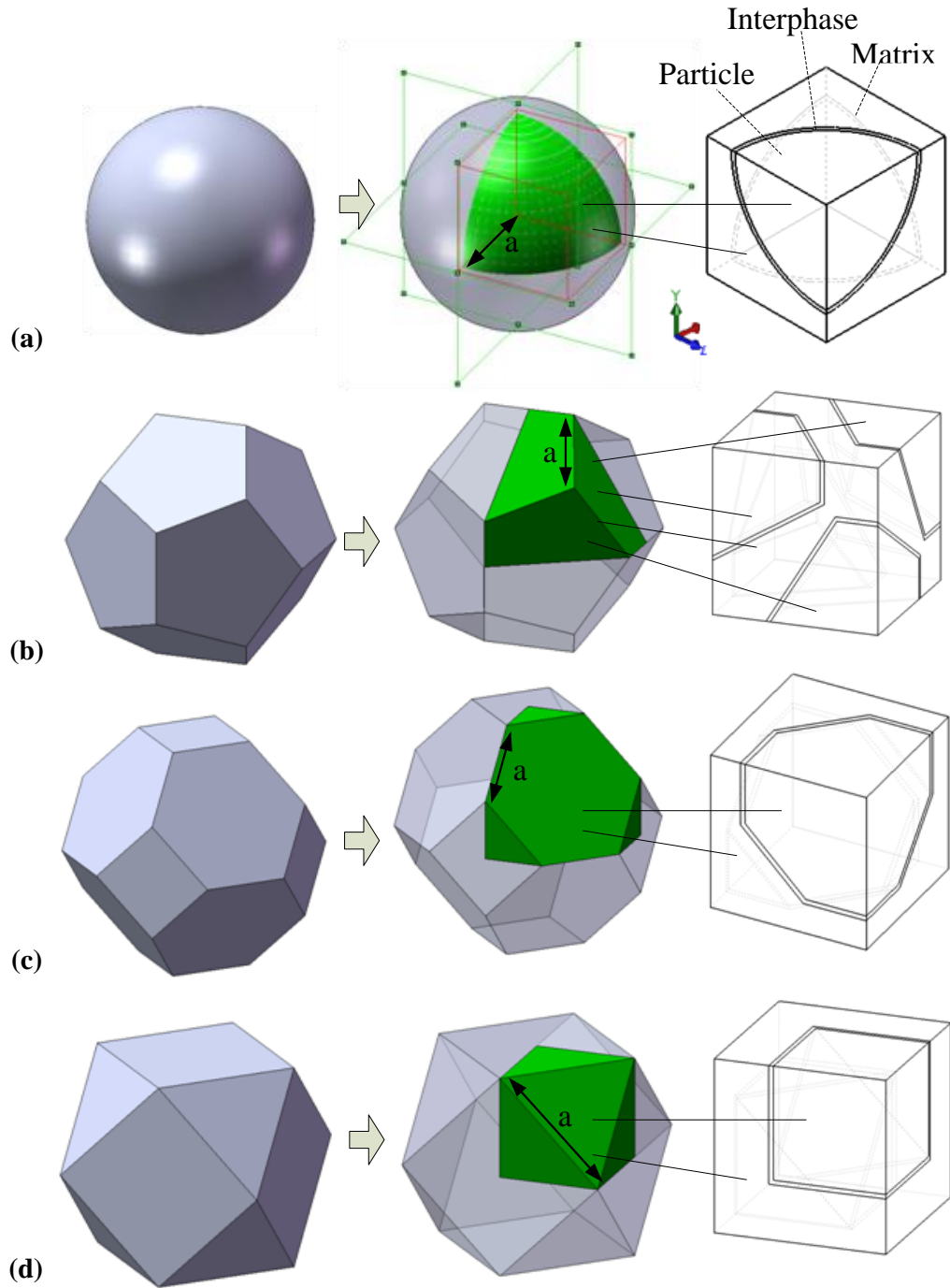


Figure 3.4: Particle geometries being used in this study (a) sphere, (b) dodecahedron, (c) truncated octahedron, and (d) cuboctahedron

To match the high particle volume fraction requirement for dental restoration applications, BCC and FCC packing architectures have been considered. The choice of packing architecture depends on the packing efficiencies of the particles which have different morphology characteristics. Regarding the experimental work from Schulze et al. (2003), the maximal particle volume fraction for a SrF₂/UEDMA:TCB:TEGDMA compomer system is about 57%. To fulfill this requirement, the particle morphology of dodecahedral shapes was modeled by an array of FCC packed architecture while the others were packed using BCC architecture. Since spheres and the three selected polyhedrons have a certain degree of symmetry; thus, cubic unit cell models were constructed using one-eighth of the particles.

To construct the cell models effectively, the inter-part parametric assembly modeling characteristic of CAD tools was employed. The characteristics allow the construction of part geometry based on the context of other parts, that is, definition of new parts with reference to existing parts within the assembly. Inter-part constraint relationships are useful when several dimensions in an assembly depend on some key dimensions. Key dimensions are characterized as the geometric parameters that can be varied, permitting design change while preserving the basic shape or design intent of the assembly. If the value of a key dimension is changed, the whole assembly will be automatically regenerated while conserving the inter-part constraints and relationships. To apply the characteristics in constructing cell models, all the assembly parts, i.e. the particle phase, interphase, and matrix phase, are first constructed and then assembled together according to the assembly specifications. The length of the cell model l is defined as the key dimension. Next, correlation constraints and relationships are set along the contact

surfaces between the particle phases and the interphase as well as the matrix phase and the interphase. Enhanced by the parametric modeling characteristic, models can be constructed in a more effective and efficient manner.

According to the information provided from the compomer dental composite manufacturer, Dyract, strontium fluoride glass particles have an equivalent spherical diameter of about 0.8 μ m. Thus, the corresponding volume V_{sphere} of spherical particle can be calculated using the formula below:

$$V_{sphere} = \frac{4}{3}\pi r^3 \quad (3.2)$$

For ease of comparing the effect of the particle volume fraction on the mechanical properties of dental composite systems, non-spherical particle phases embedded inside the unit cell models are constructed using the edge length a (as shown in Figure 3.4), such that the volume of the non-spherical particle phase is equal to the spherical one. The value of edge length a for different morphologies can be calculated using the formulas below:

For the cuboctahedral case,

$$a = \sqrt[3]{\frac{3V_{sphere}}{5\sqrt{2}}} \quad (3.3)$$

For the truncated octahedral case,

$$a = \sqrt[3]{\frac{V_{sphere}}{8\sqrt{2}}} \quad (3.4)$$

For the dodecahedral case,

$$a = \sqrt[3]{\frac{4V_{sphere}}{15+7\sqrt{5}}} \quad (3.5)$$

Since the size of particle is fixed, unit cells with the desired volume percentage of particle content \emptyset architecture can be obtained through varying the length of unit cell l using the equation below:

For BCC packed unit cell:

$$l = \sqrt[3]{\frac{2\pi r^3}{3\emptyset}} \quad (3.6)$$

For FCC packed unit cell:

$$l = \sqrt[3]{\frac{4\pi r^3}{3\emptyset}} \quad (3.7)$$

When the geometric parameter of the key dimension l is changed, a new model can be automatically generated while the inter-part constraints and relationships are preserved. Figure 3.5 illustrates the case of obtaining a series of unit cell models with a spherical particle phase, with a particle volume fraction that varied from 20% to 60%, through a simple key dimension modification process. The generated solid models can then be exported as geometric information files and used as inputs for the finite element analysis. The damage coupled mechanical properties of the particle, interface, and matrix phases are imported from the finite element computation of the 3D cell models.

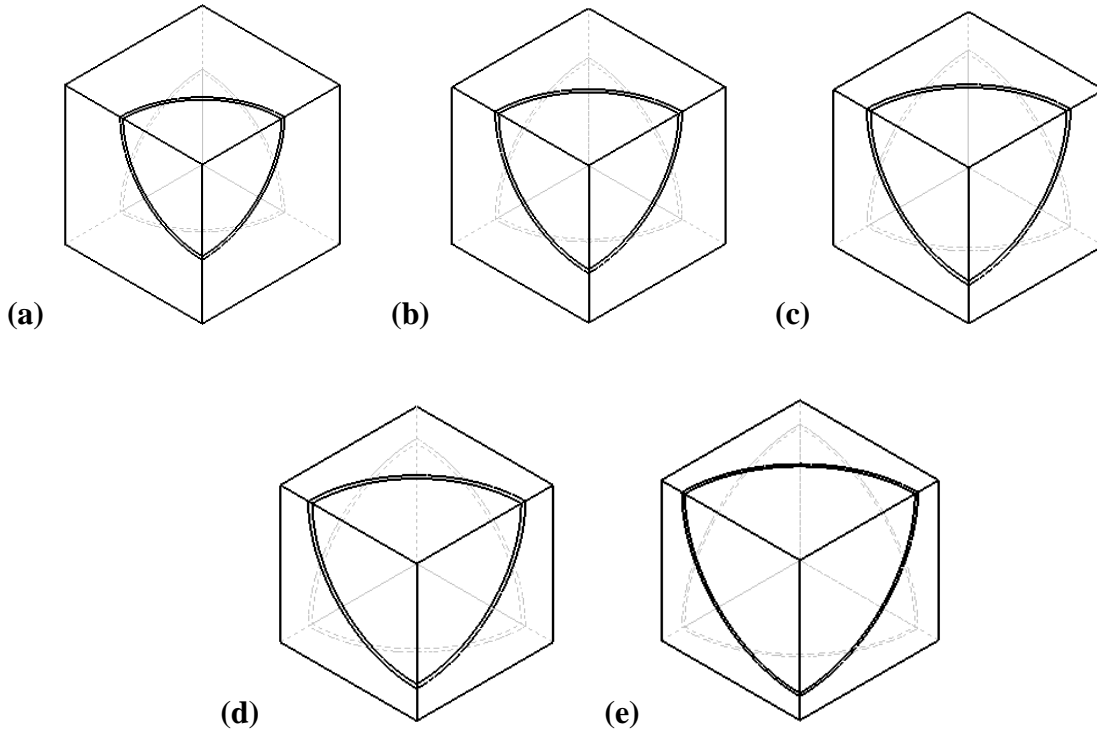


Figure 3.5: Unit cell models with spherical particle phase packed using the body-centered cubic system with a volume fraction of (a) 20%, (b) 30%, (c) 40%, (d) 50%, and (e) 60%

To conduct finite element analysis, unit cell solid models need to be meshed. 3D tetrahedral solid elements (C3D4) are used in this study; an example of a finite element grid of FCC packed dodecahedral particles is shown in Figure 3.6. Explicit finite element theory has been employed, as discussed in Section 2.8. During the finite element analysis, tensile loading is applied on the face A in the 3-direction through a prescribed displacement. To ensure that the composite unit cell model is periodic in nature, all faces of the model need to be constrained parallel to the original position after movement throughout the FE analysis. Boundary conditions are applied so that faces C, E, and F are

fixed and the displacement in their normal direction is set to zero, while faces A, B, and D are constrained to maintain planarity within the loading process.

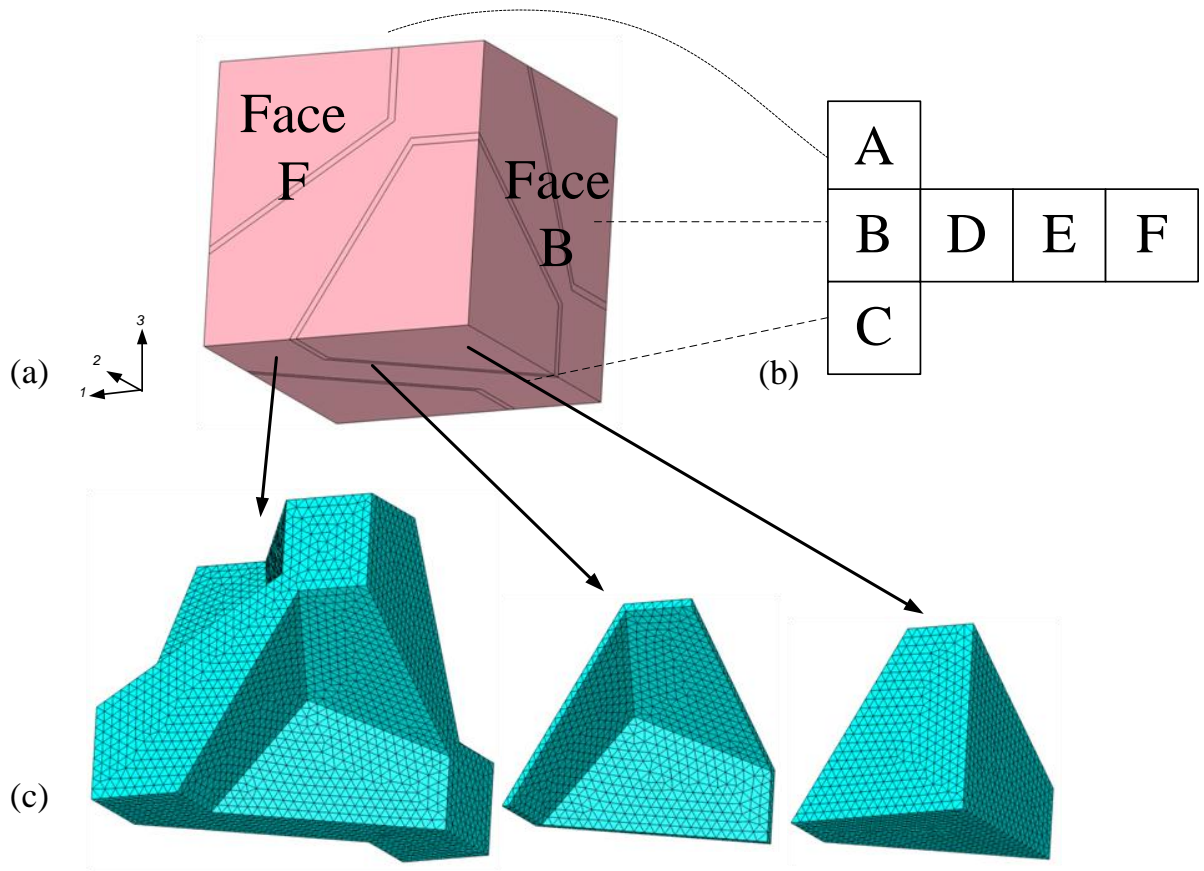


Figure 3.6: (a) Face-centered cubic unit cell model comprising dodecahedral particles, (b) development of the cell model, (c) finite element grid of the matrix, interface, and particle phases

3.3. Micro-damage Mechanism Prediction

3.3.1. Effect of Particle Morphology and Volume Fraction on the Stress Concentration and Distribution

The stress concentration factor (SCF) of the composite used is defined as:

$$SCF = \frac{\sigma_{\psi_{max}}}{\bar{\sigma}_{\psi}} \quad (3.8)$$

where $\sigma_{\psi_{max}}$ is the maximum direct stress and $\bar{\sigma}_{\psi}$ is the average applied stress in the ψ -direction. The changes of the SCF with the four particle morphologies and particle volume fraction from 20% to 60% are shown in Figure 3.7 and Figure 3.8 respectively.

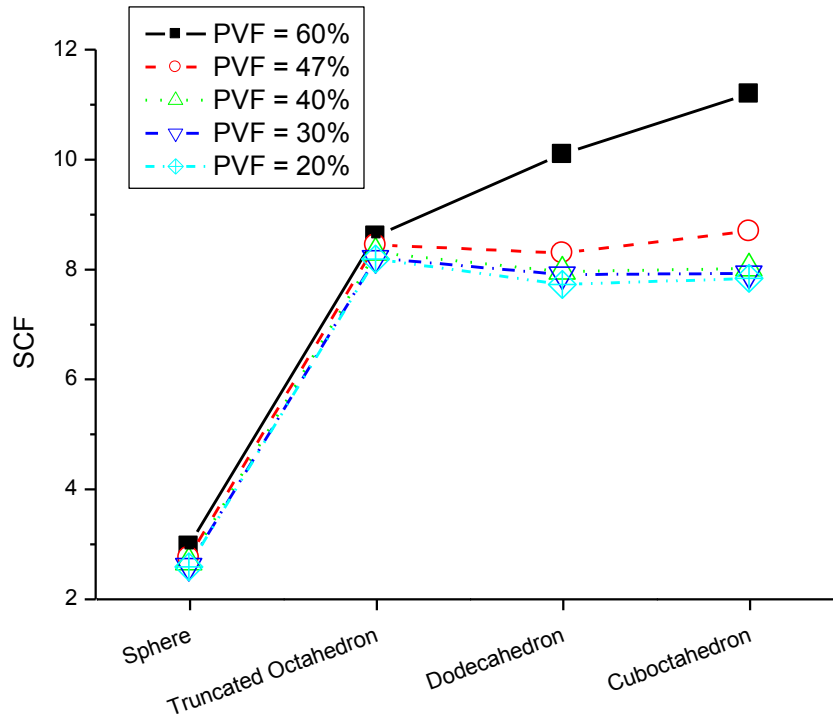


Figure 3.7: FEM calculated stress concentration factor (SCF) vs. four particle morphologies

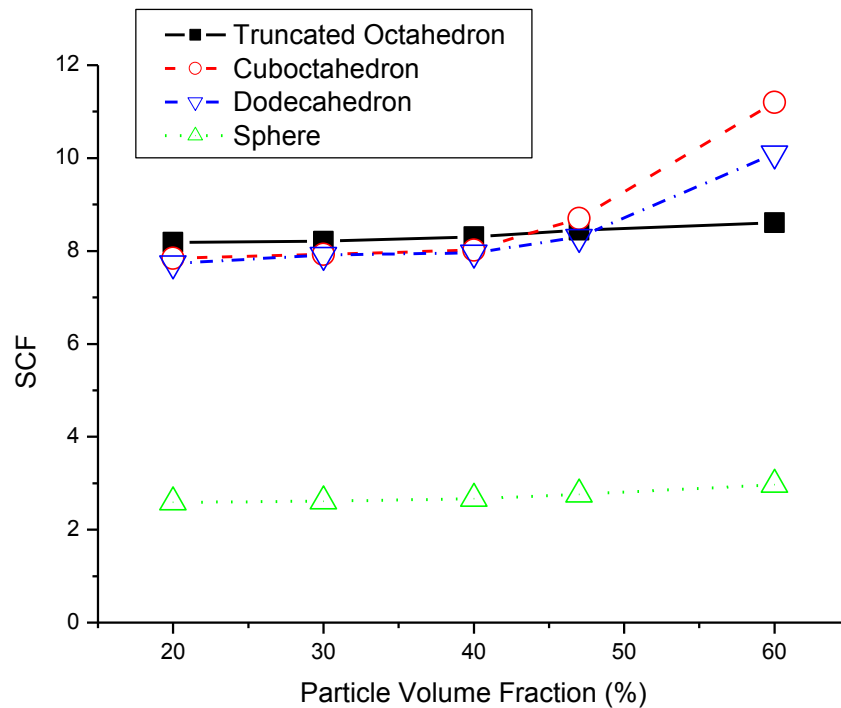


Figure 3.8: FEM calculated stress concentration factor (SCF) vs. various particle volume fractions

SCF is sensitive to both particle volume fraction and particle morphology. In general, SCF increases with increased particle volume fraction. In the case of the spherical and truncated octahedral particles, the values of SCF increase mildly with respect to particle volume fraction, but steadily for the dodecahedral and cuboctahedral particles especially after particle volume fraction values above 40%. This can be explained by the increased interaction between the stress fields among the particles as they get closer. Inclusions having dodecahedral and cuboctahedral morphologies are more sensitive to the interaction among particles than spherical and truncated octahedral ones.

To further investigate the large discrepancy on the SCF values among the spherical and non-spherical inclusions, the stress contours, as well as the deformed particle, interphase, and matrix phases of the unit cell models with different particle morphologies, are plotted in Figures 3.9-3.12. All the unit cells have a particle volume fraction of 20% and are loaded under tensile deformation at a strain value of 0.3%, which is before the occurrence of interfacial debonding damage. In the figures, the location and the value of the maximum direct stress of the three phases are highlighted.

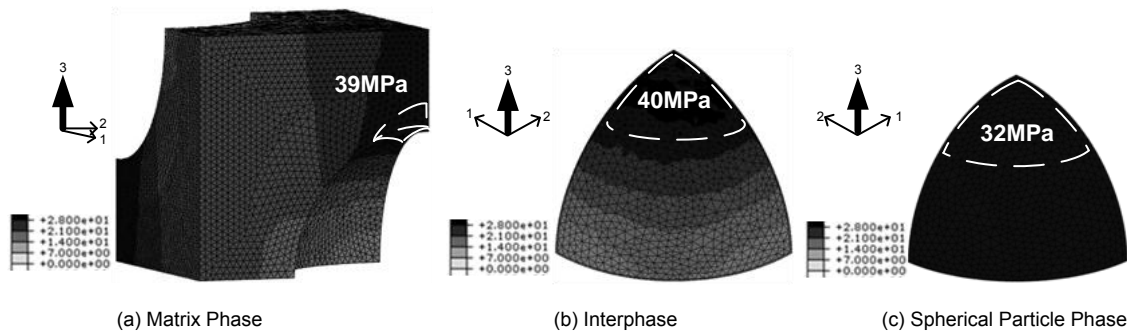


Figure 3.9: Predicted stress distribution in the (a) matrix, (b) interphase, and (c) particle phases in the compomer dental system with PVF=20% for spherical particles under tensile deformation with strain value of 0.3%. (in each phase, the bold arrow shows the loading direction; the region wrapped by the dotted lines describes the areas having high stress concentration value)

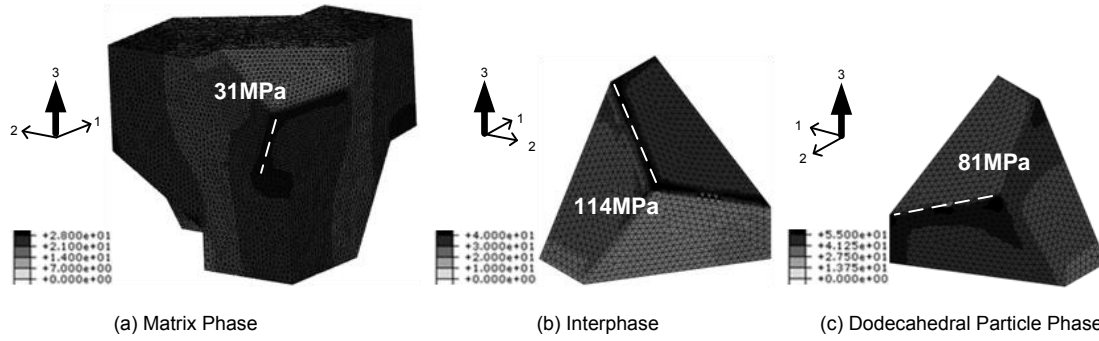


Figure 3.10: Predicted stress distribution in the (a) matrix, (b) interphase, and (c) particle phases in the compomer dental system with PVF=20% for dodecahedral particles under tensile deformation with strain value of 0.3%. (in each phase, the bold arrow shows the loading direction; the dotted line highlights the position with high stress concentration value)

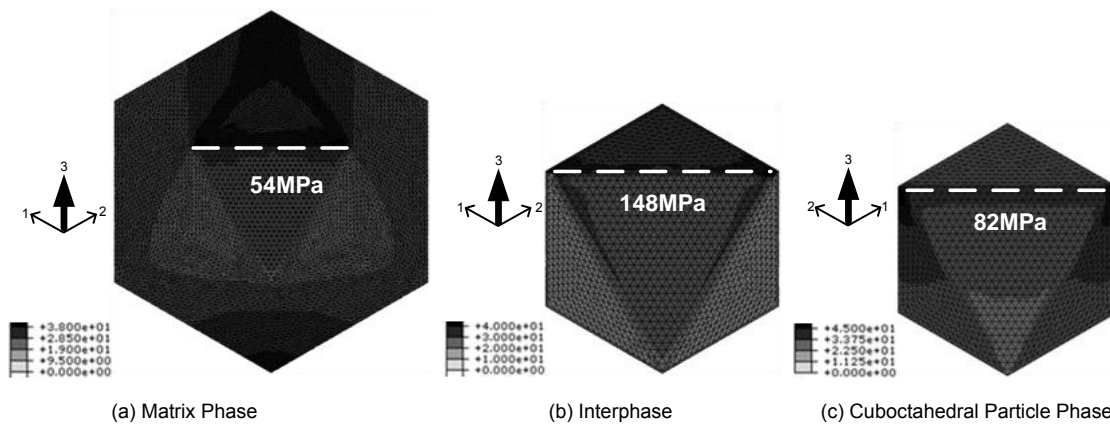


Figure 3.11: Predicted stress distribution in the (a) matrix, (b) interphase, and (c) particle phases in the compomer dental system with PVF=20% for cuboctahedral particles under tensile deformation with strain value of 0.3%. (in each phase, the bold arrow shows the loading direction; the dotted line highlights the position with high stress concentration value)

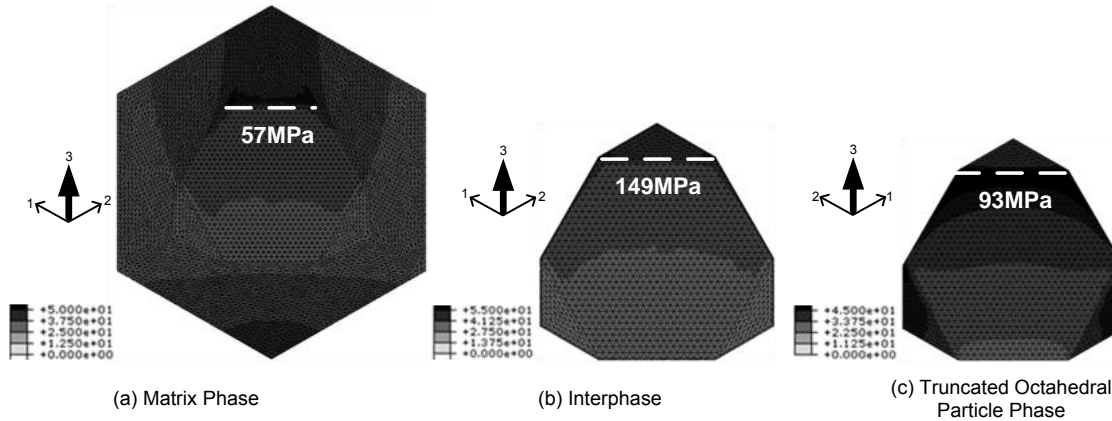


Figure 3.12: Predicted stress distribution in the (a) matrix, (b) interphase, and (c) particle phases in the compomer dental system with PVF=20% for truncated octahedral particles under tensile deformation with strain value of 0.3%. (in each phase, the bold arrow shows the loading direction; the dotted line highlights the position with high stress concentration value)

For all the considered particle morphologies, it is found that the maximum direct stress values of the composite are located at the interphase. This can be explained by the interphase region being assigned the same material properties as the matrix before the occurrence of damage. The interphase has the mechanical properties disparity problem, with the particle phase. The disparity problem leads to the concentration of stress in the interphase region. For non-spherical cases, the position of the maximum direct stress appears at the edge of the interphase, lying close to the matrix cell boundaries along the loading direction. For spherical particles, the maximum value appears in the polar region and is distributed more evenly. Thus, the maximum for spherical morphologies is lower than those obtained from non-spherical morphologies.

The high stress concentration being calculated in the interphase region, probably would lead to its failure. The initiation and propagation of damage in the compomer composite system is predicted using a stress-based criterion, and details are discussed in the next section.

3.3.2. Effect of Particle Morphology and Volume Fraction on the Interfacial Debonding Damage Process and the Stress Distribution

To investigate the process of interfacial debonding damage, a hydrostatic tensile stress $\bar{\sigma}_H$ failure criterion has been adopted for the interfacial elements and set as 60% of the matrix strength (Asmussen and Peutzfeldt, 1998), and the reason for choosing the value is discussed in Section 3.4.1.2.

The cell models with the four particle morphologies and particle volume fractions from 20% to 60% have been loaded to different strain values. For models with the same particle morphology but different particle volume fraction, a similar debonding process is observed. The only difference is that damage is initiated earlier for a model having a higher particle volume fraction. This can be explained due to the increased interaction between the stress fields among the particles as they were closer. As discussed in the previous section, a higher SCF would be obtained, thus, the interfacial element would reach the critical stress value σ_c earlier and initiate damage at a relatively lower strain value.

Figures 3.13-3.16 describe the initiation and propagation of interfacial debonding damage of compomer dental composites with spherical, cuboctahedral, dodecahedral, and truncated octahedral particle morphologies respectively.

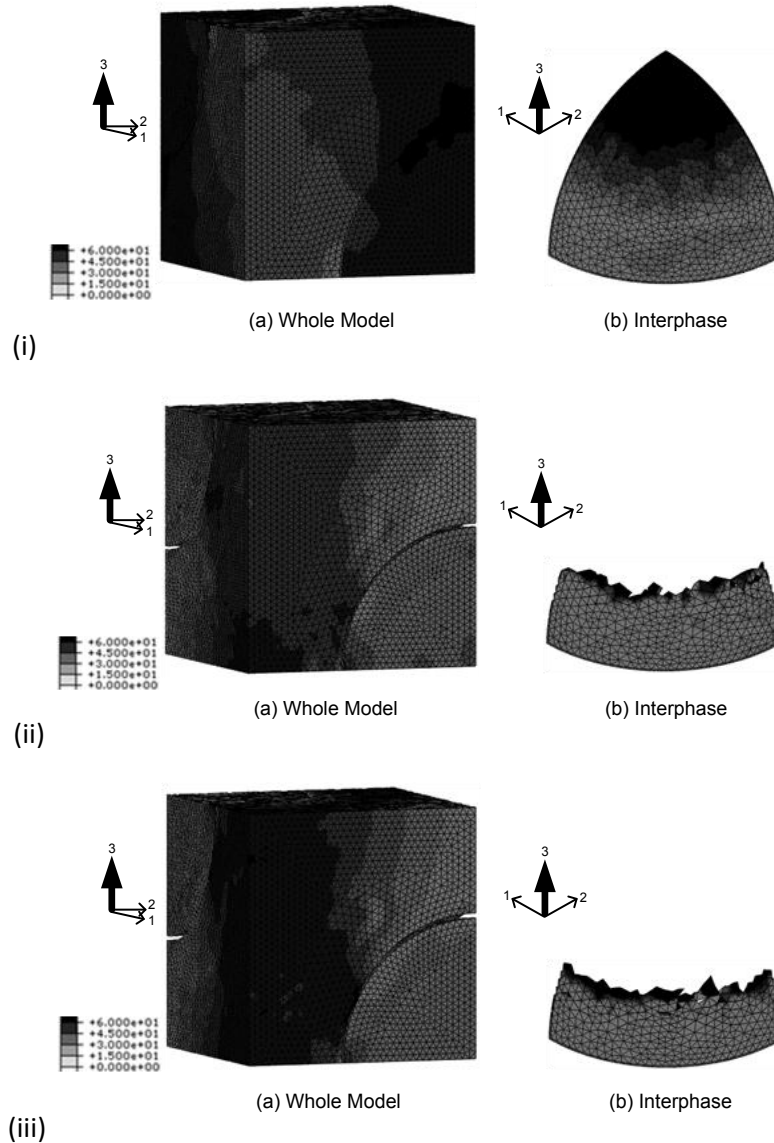


Figure 3.13: Predicted stress distribution in the (a) whole unit cell model with spherical particle morphology and the corresponding (b) interphase at various strain value: (i) 0.75%, (ii) 2.5%, and (iii) 3%. (the bold arrow indicates the loading direction)

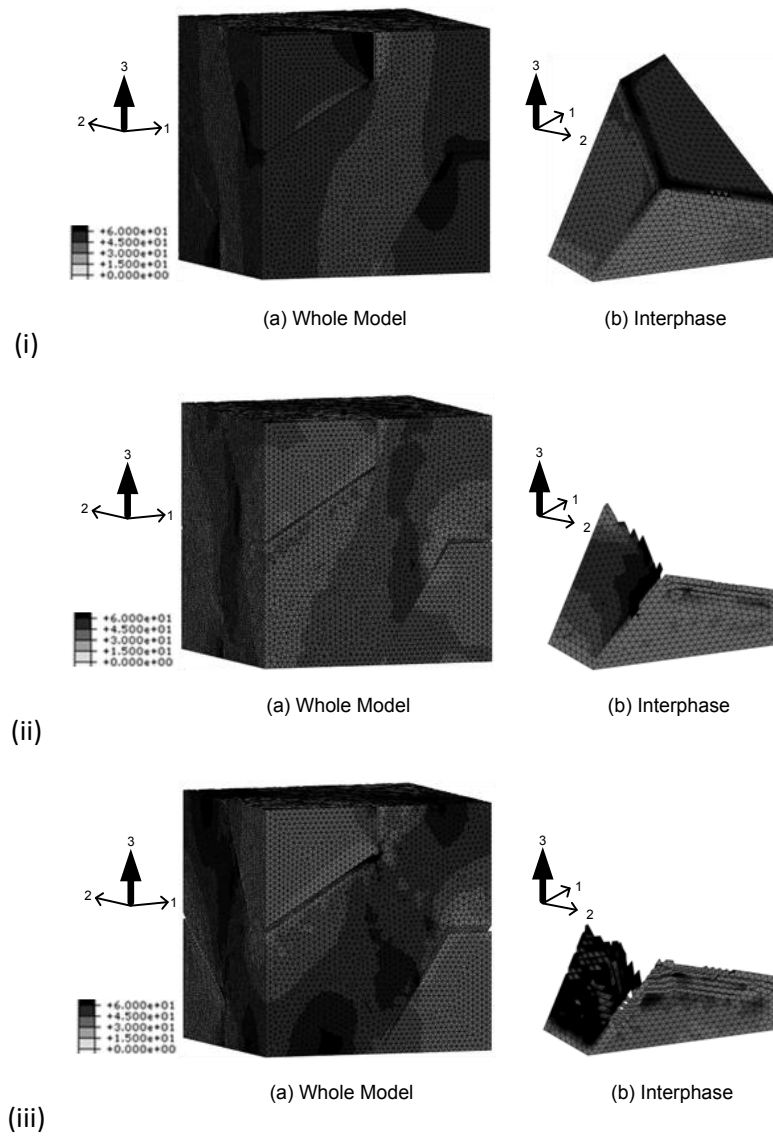


Figure 3.14: Predicted stress distribution in the (a) whole unit cell model with dodecahedral particle morphology and the corresponding (b) interphase at various strain value: (i) 0.6%, (ii) 1.1%, and (iii) 3%. (the bold arrow indicates the loading direction)

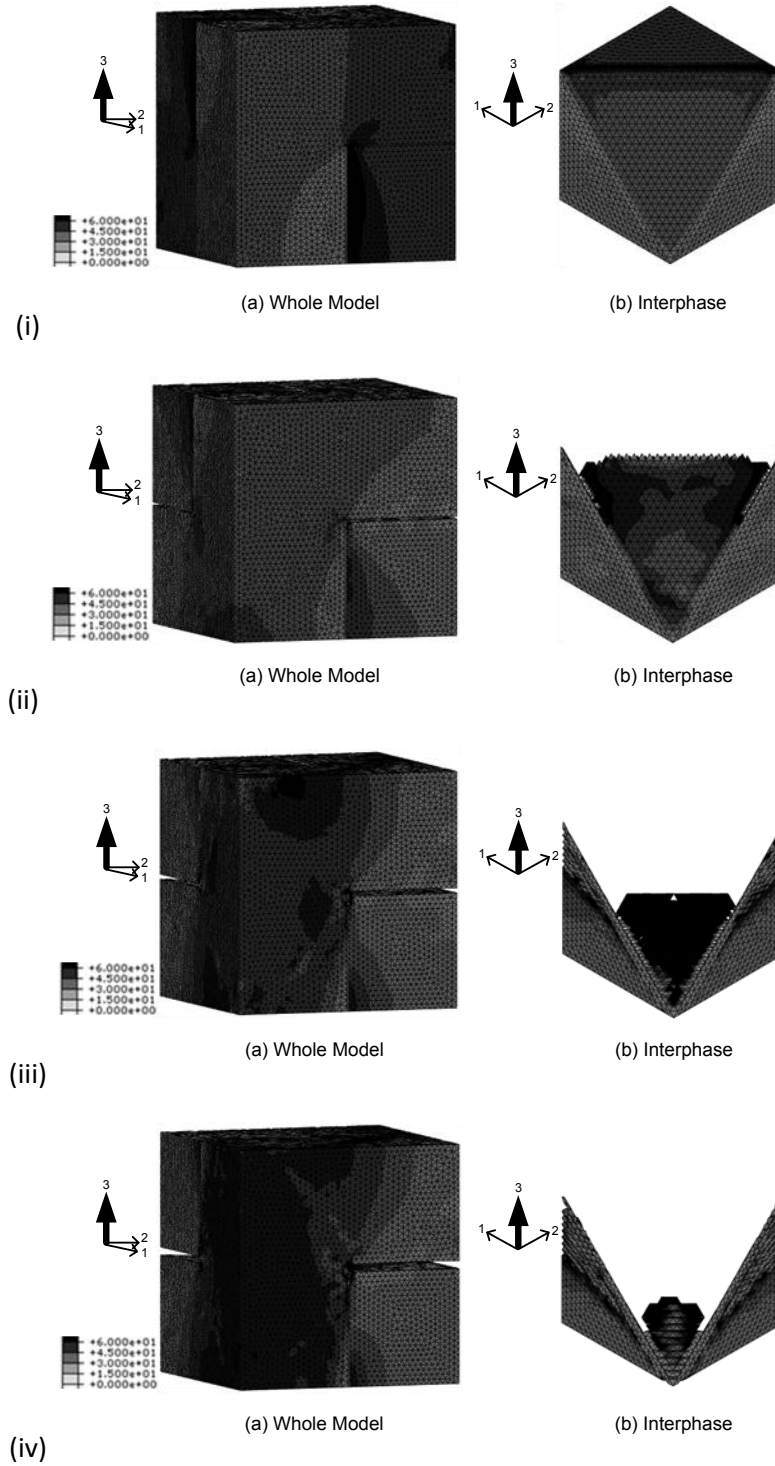


Figure 3.15: Predicted stress distribution in the (a) whole unit cell model with cuboctahedral particle morphology and the corresponding (b) interphase at various strain value: (i) 0.45%, (ii) 0.6%, (iii) 1.65%, and (iv) 3%. (the bold arrow indicates the loading direction)

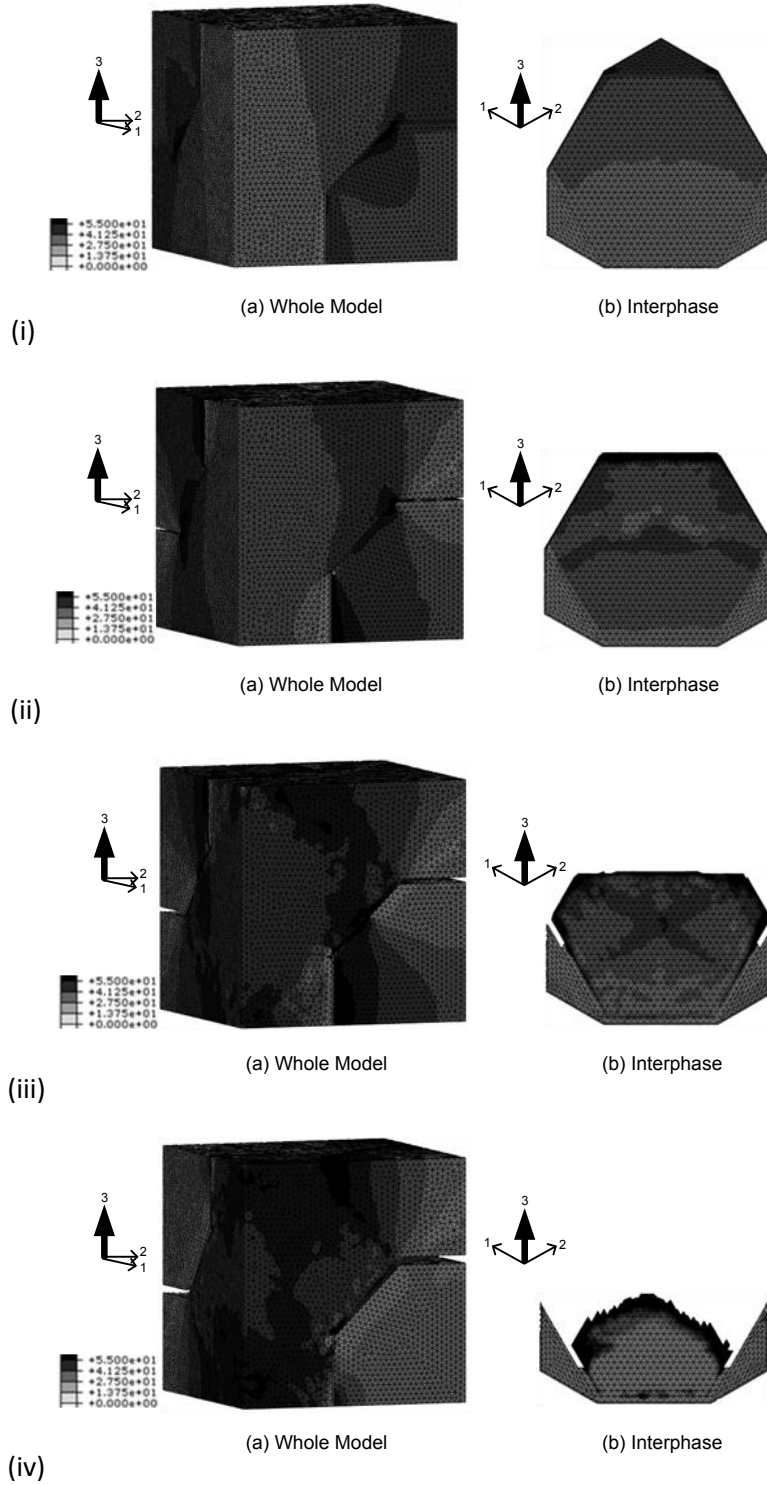


Figure 3.16: Predicted stress distribution in the (a) whole unit cell model with truncated octahedral particle morphology and the corresponding (b) interphase at various strain value: (i) 0.3%, (ii) 0.6%, (iii) 1.65%, and (iv) 3%. (the bold arrow indicates the loading direction)

Under small strain values, as shown in the (i) part of each figure, the compomer composite are in an intact state since none of the elements in the interphase has exceeded the hydrostatic critical value σ_c . In such state, in the particle phase, it is found that most of the loading is sustained on the faces in contact with the interphase. Concerning the interphase and matrix phases, more stresses are observed in the region above the polar part of the particle along the loading direction. This is in a good agreement with the previous study conducted by Balać et al. (2001) on the stress analysis in hydroxyapatite reinforced composites.

The cell models are further stretched, part (ii) of each figure represents the moment where damage is initiated. Values of $\bar{\sigma}_H$ of the interfacial elements exceeding σ_c are removed from the mesh. For non-spherical cases, interfacial elements covering the face located nearest to the polar zone, with the edge having the maximum direct stress value (discussed in the previous section, Figure 3.10-3.12) are removed simultaneously. For spherical particles, interfacial elements in the polar region have been removed. Such region is the same as the region identified as having the highest stress concentration value. Based on the computational results, the onset of debonding damage under the lowest value of strain is for the unit cell model with truncated octahedral shaped particles followed by cuboctahedral, dodecahedral, and spherical shaped particles. Such sequence is the same as the predicted SCF from the largest to lowest, as shown in Figure 3.8 in the previous section. Concerning the stress distribution, stresses are concentrated around the debonded tips in the interphase. Moreover, the matrix phase above the debonded region sustained less stress in comparison with the bonded region.

When the cell models are continued to be stretched, the composite would be in a partially debonded state, as depicted in the (iii) and (iv) parts of each figure. In the unit cell model with either spherical or non-spherical particles, interfacial debonding propagated progressively from the polar region to the equatorial region of the interphase. Among the non-spherical groups, truncated octahedral shaped particles give the slowest rate of damage propagation. At the strain value of 1.65%, it is observed that over half of the interphase elements for the cuboctahedral and dodecahedral shaped particles have been deleted while about three-fourth interphase elements still remained for truncated octahedral shapes. Besides, the stress distributions in the interphase and matrix phase are changed and follow the pattern described previously. The void owing to interfacial debonding increased in dimension with increase in strain. This is in a good agreement with the experimental study conducted by Tsui et al. (2006) on glass bead filled composites.

3.4. Macro-structural Behavior Prediction

3.4.1. Effect of Particle Morphology and Micro-damage on the Mechanical Properties

3.4.1.1. Elastic Modulus

Before the occurrence of interfacial debonding damage, the predicted elastic moduli E_{FE} at various particle morphologies having particle volume fractions of 47% are calculated (as shown in Figure 3.17). The choice of the particle volume fraction is due to the availability of the experimental data from the literature, which involved the commercially

available dental composite (Xu and Burgess, 2003). The elastic modulus E_{FE} of the composite is defined as:

$$E_{FE} = \frac{\bar{\sigma}_3}{\varepsilon_3} \quad (3.9)$$

where $\bar{\sigma}_3$ is the applied stress obtained by averaging the stress value of each element on face A in the 3-direction, and ε_3 is the applied strain.

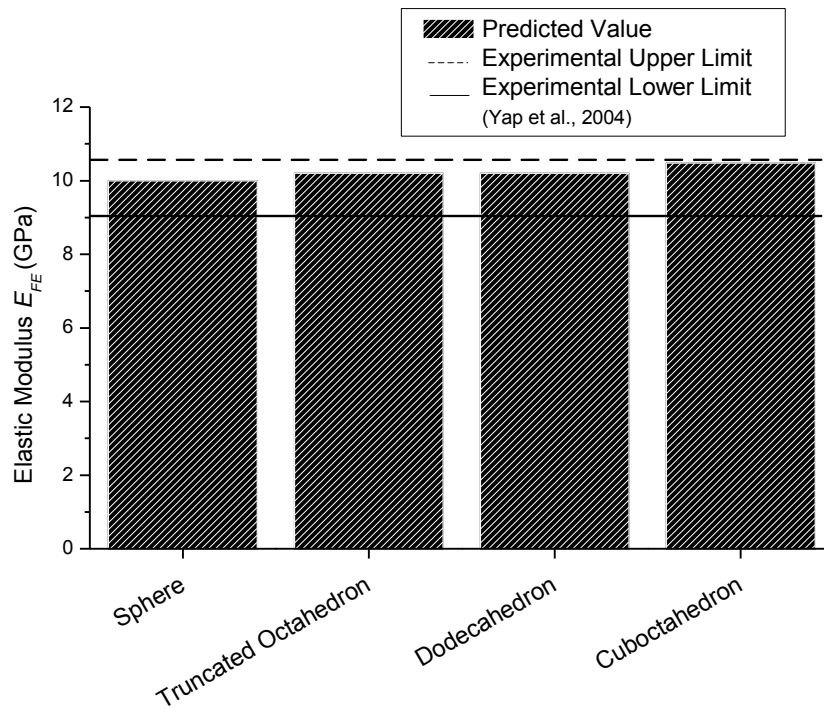


Figure 3.17: Comparison between the predicted elastic moduli of the dental composites with different particle morphologies and the experimental data

To verify the unit cell model predictions, comparison is made between the predicted elastic modulus and experimental data (Yap et al., 2004). All the predicted values are found to fall within the experimental limits. This finding suggests the appropriateness of

using the four particle morphologies for representation of the various shaped particles inside the dental composites. In addition, it appears that the elastic modulus of composites is nearly independent of particle morphology.

3.4.1.2. Stress-strain Relation

To study the effect of interfacial damage and particle morphology on stress-strain relation, unit cell models with spherical, dodecahedral, cuboctahedral, and truncated octahedral shaped particles have been used. The value of σ_c in the interface elements has been set as 60% of the matrix strength. Figure 3.18 shows the effect of particle morphology on the predicted stress-strain ($\bar{\sigma}_3 - \varepsilon_3$) curves from the unit cell model with 60% particle volume fraction.

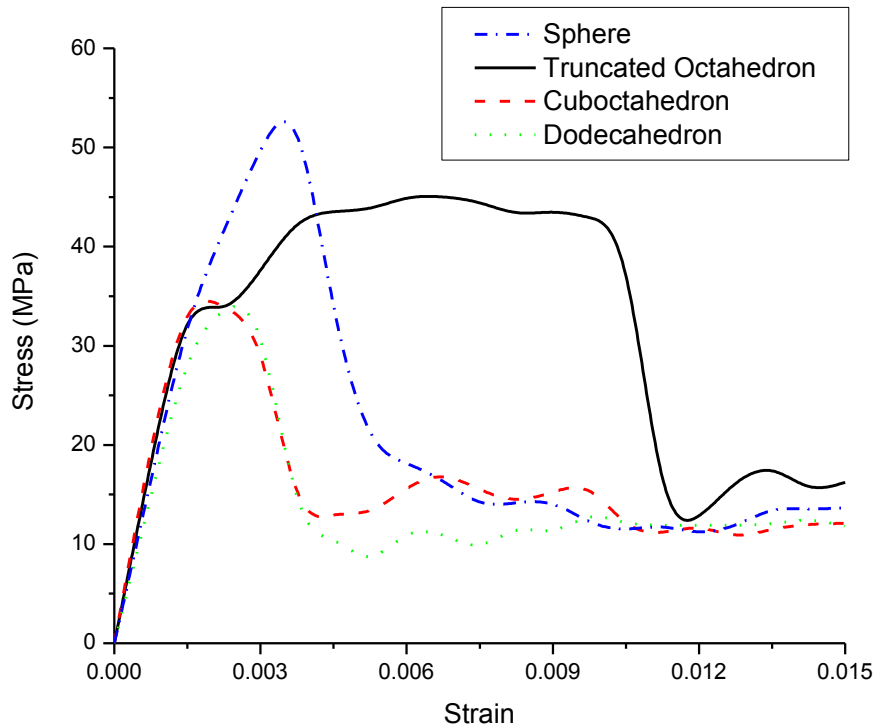


Figure 3.18: Predicted stress-strain curves of the compomer composite with particle volume fraction of 60% and different particle morphologies

During the elastic portion, no obvious effect on the composite stiffness was found through using different particle morphologies. Within the plastic deformation range, the compomer composite gives a higher stress value for the unit cell model with spherical shaped particles, followed by truncated octahedrals, cuboctahedrals, and dodecahedral shaped particles. For the case of truncated octahedrals, the shape of the predicted stress-strain curve is slightly different from the common type. This is due to its special morphological characteristics which let the interfacial damage propagate slowly, as discussed in Section 3.4.2. Among the non-spherical group, models with cuboctahedral

and dodecahedral shaped particles have nearly the same stress-strain relations, similar to the normal ones. Dodecahedral morphology was selected as the representative morphology for predicting the mechanical behavior of dental composites with non-spherical inclusions (please read the explain in section 3.4.2.3).

To study the effect of interfacial adhesion on the stress-strain relation and to inversely identify the interfacial strength of the compomer dental composite, the value of σ_c was varied. Additionally, an extreme case with no interfacial debonding has also been taken into account for comparison.

Figure 3.19 depicts the influence of different interfacial strengths on the predicted stress-strain ($\bar{\sigma}_3 - \varepsilon_3$) curves for the unit cell model with dodecahedral particles and 47% particle volume fraction. In the elastic range, no apparent effect on the composite stiffness is observed through varying the interfacial strength. Within the plastic deformation range, a composite defined with a larger σ_c gives a higher stress value than that with a smaller σ_c . Additionally, the stress-strain curve of the compomer composite with σ_c equal to 60% of the matrix strength (Asmussen and Peutzfeldt, 1998) gives a tensile strength in agreement with the experimental data (Schulze et al., 2003). Therefore, σ_c was set as 60% of the matrix strength in this study.

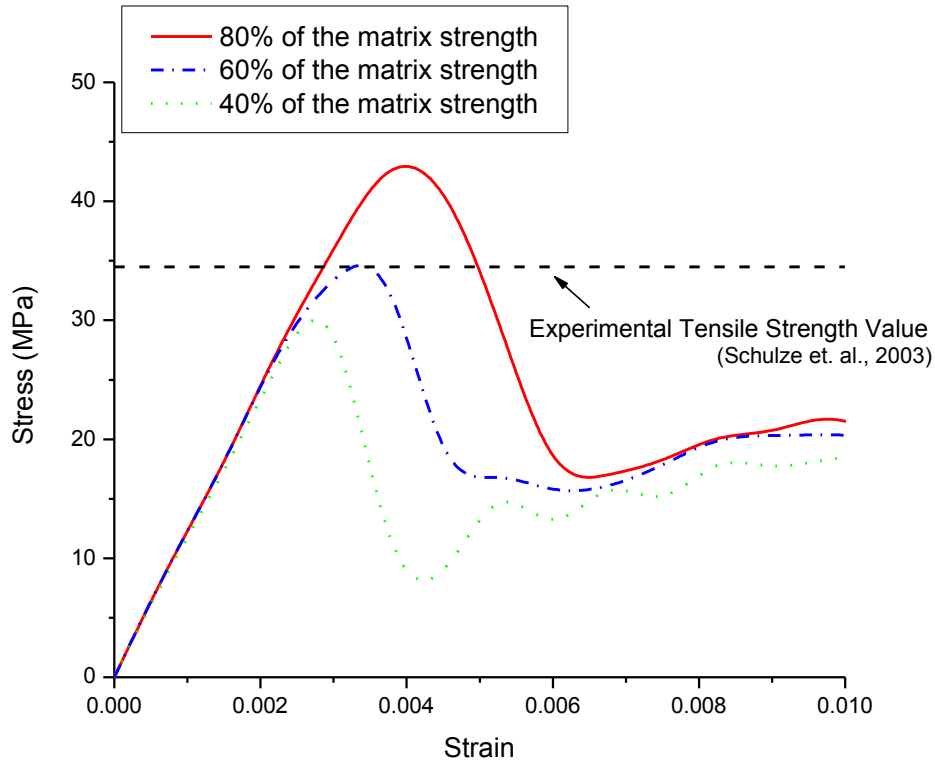


Figure 3.19: Predicted stress-strain curves of the compomer composite with dodecahedral shaped particle, particle volume fraction of 47%, and different interfacial strength values

3.4.1.3. Tensile Strength

To study the effect of interfacial adhesion and particle morphology on tensile strength, unit cell models with spherical, dodecahedral, cuboctahedral, and truncated octahedral shaped particles were used. In consideration of debonding damage, the value of σ_c in the interface elements has been set at 60% of the matrix strength.

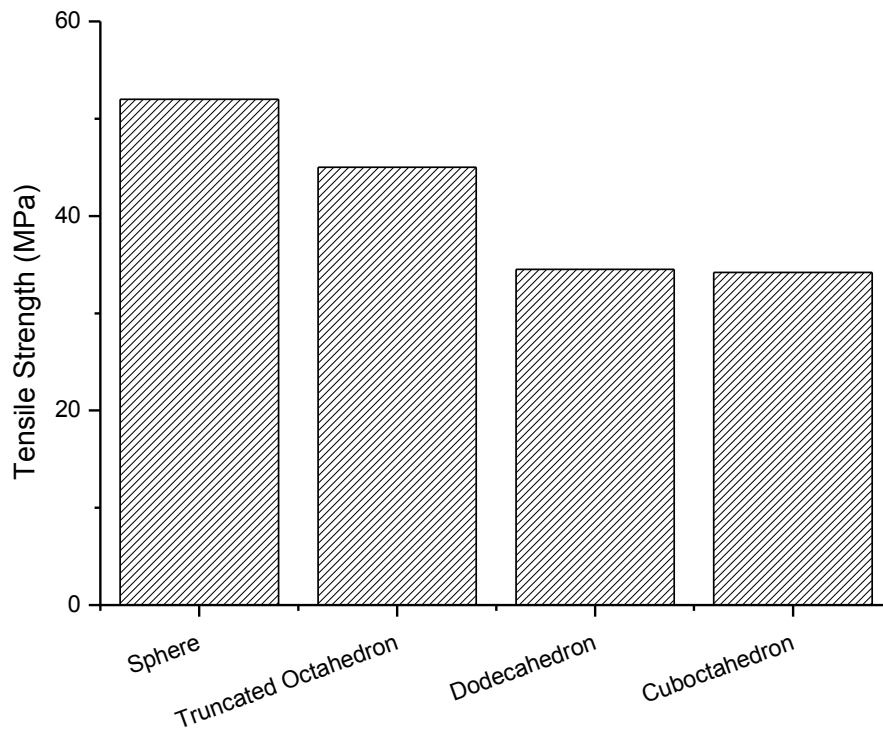


Figure 3.20: Predicted tensile strength of the compomer composite vs. various particle morphologies

Figure 3.20 shows the influence of interfacial adhesion on the predicted tensile strength from the unit cell model with 60% particle volume fraction. From the consideration of damage, it is observed that composite with spherical particles have a higher tensile strength than non-spherical ones. Among the three considered non-spherical particles, truncated octahedron gives a higher tensile strength. For particles having dodecahedral and cuboctahedral morphologies, they present with similar value.

3.4.2. Effect of Particle Volume Fraction and Micro-damage on the Mechanical Properties

3.4.2.1. Elastic Modulus

Before the occurrence of interfacial debonding damage, the predicted elastic modulus E_{FE} of the composite is calculated using equation (3.9). To verify the unit cell model predictions, a comparison is made between the predicted elastic modulus and the experimental data (Schulze et al., 2003), as shown in Figure 3.21. Good agreement between the predicted and experimental results can be observed. It is also observed that E_{FE} of the composite is nearly directly proportional to the particle volume fraction and appears to be nearly independent of particle morphology (Figure 3.22).

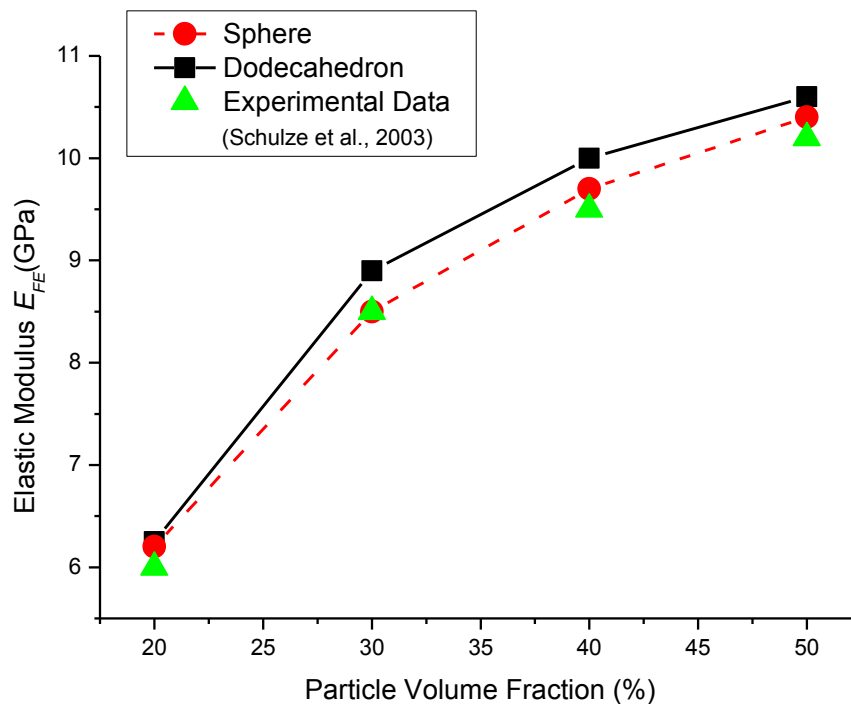


Figure 3.21: Comparison between the predicted elastic moduli of the dental composites with different particle loadings and the experimental data

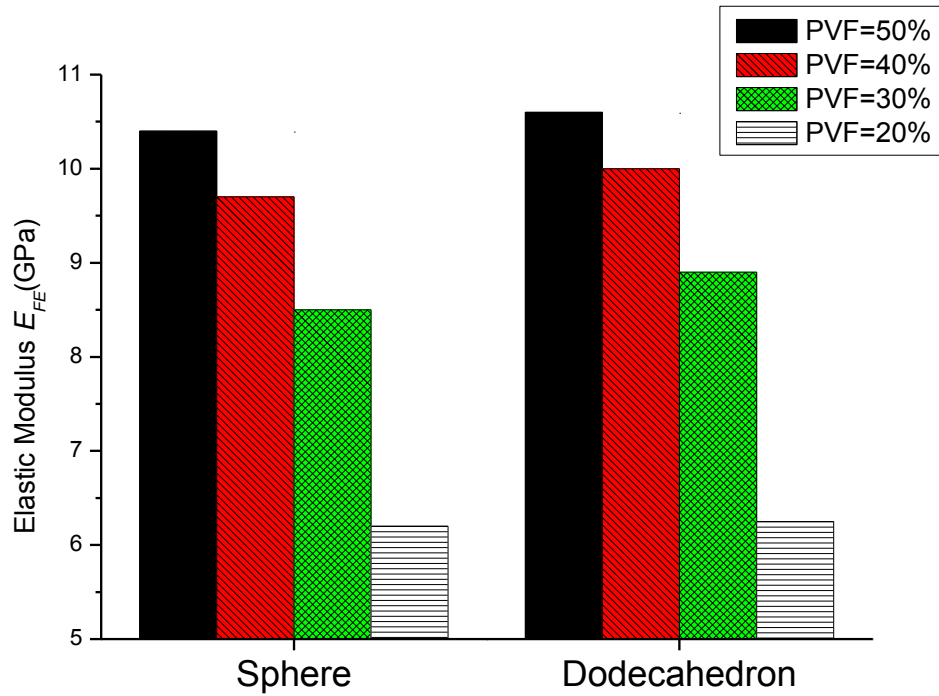


Figure 3.22: Predicted elastic modulus for particle with spherical and dodecahedral morphologies

3.4.2.2. Stress-strain Relation

To study the effect of interfacial debonding damage and particle volume fraction on the stress-strain relation of the compomer dental composite with non-spherical shaped inclusions, unit cell models with dodecahedral shaped particles having different particle volume fractions have been used, with the σ_c set to 60% of the matrix strength. Figure 3.23 depicts the influence of different particle volume fractions on the predicted stress-strain ($\bar{\sigma}_3 - \epsilon_3$) curves.

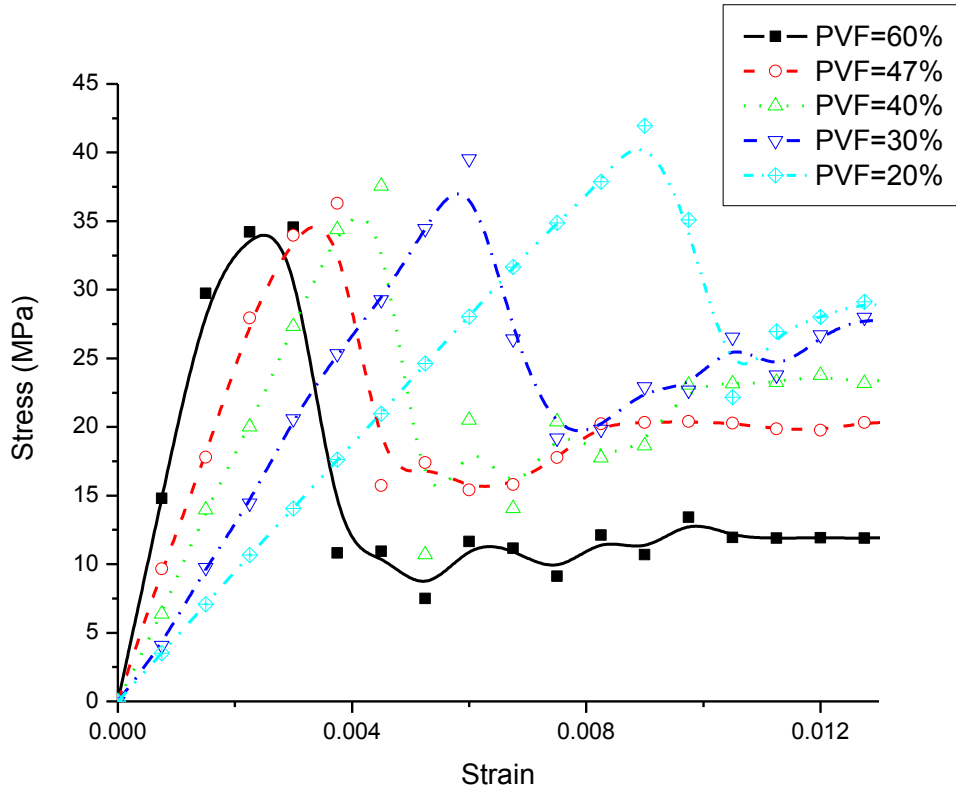


Figure 3.23: Predicted stress-strain curves of the compomer composite with dodecahedral shaped particle, σ_c equals to 60% of matrix strength, and different particle volume fractions

During the elastic portion, the stiffness of the composite with a higher particle volume fraction becomes significantly higher than that with a lower volume fraction. Further increase in the strain, the composites undergo damage softening. A composite with higher particle volume fraction often exhibits the softening behavior at a lower value of the strain.

3.4.2.3. Tensile Strength

To study the effect of debonding damage and particle volume fraction on tensile strength, unit cell models with spherical, unit cell models with dodecahedral shaped particles having different particle volume fractions have been used. The value of σ_c in the interface elements has been set at 60% of the matrix strength.

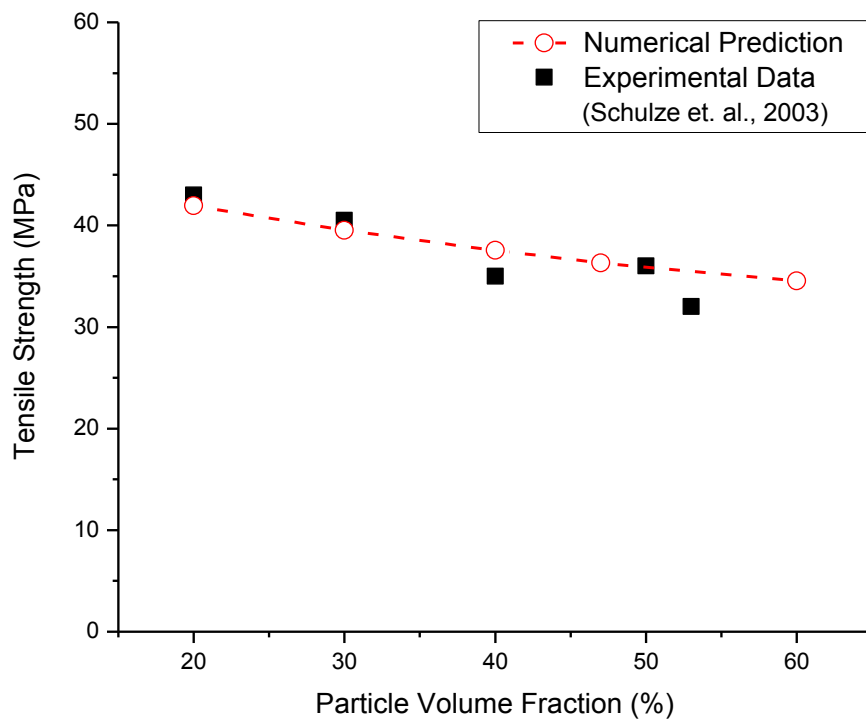


Figure 3.24: Predicted tensile strength of the compomer composite vs. various particle volume fractions

Figure 3.24 describes the influence of different particle volume fractions on the predicted tensile strength. The tensile strength decreases with increased particle volume fraction.

The predicted results give a good agreement with the experimental data (Schulze et al., 2003). This finding suggests the appropriateness of using dodecahedral particles as the representative morphology for the compomer composite involving non-spherical inclusions, and the definition of 60% of the matrix strength for the value of σ_c as the hydrostatic stress failure criteria in modeling interfacial debonding damage.

Chapter 4. Determination of the Mechanical Properties of Enamel and Dentin in Multi-scale

In this chapter, the objectives are to determine the isotropic mechanical properties of micro-scale constituents of a tooth and to determine the anisotropic mechanical properties of enamel and dentin in bulk. Regarding the bulk properties, they are determined based on interactions between micro-scale and macro-scale stresses and strains. In the macro-level, enamel and dentin behave with a sort of anisotropy. Figure 4.1(a) and Figure 4.1(b) show the SEM images of coronal section of enamel and dentin while Figure 4.1(c) and Figure 4.1(d) present the images of their bucco-lingual sections respectively. In the micro-scale, enamel and dentin can be viewed as a composite with continuous fiber reinforcement. In relation to several tubules, the plane parallel to the coronal surface can be defined as a plane of isotropy. Consequently, the anisotropic responses of dentin are modeled as transversely isotropic. For the case of enamel, rods are regarded as cylindrical fibers immersed in the matrix of the interrod constituents. Rods are parallel to each other and perpendicular from the occlusal enamel surface to dentin enamel junction (DEJ). For the case of dentin, a hollow tubule enclosed by the peritubular constituents can be regarded as a cylindrical fiber which immerses in the intertubular constituents formulating the matrix. Each tubule extends continuously from the DEJ to the pulp. Similarly, for several rods, the plane parallel to the occlusal surface can be defined as a plane of isotropy. Thus, the anisotropic responses of enamel are modeled as transversely isotropic.

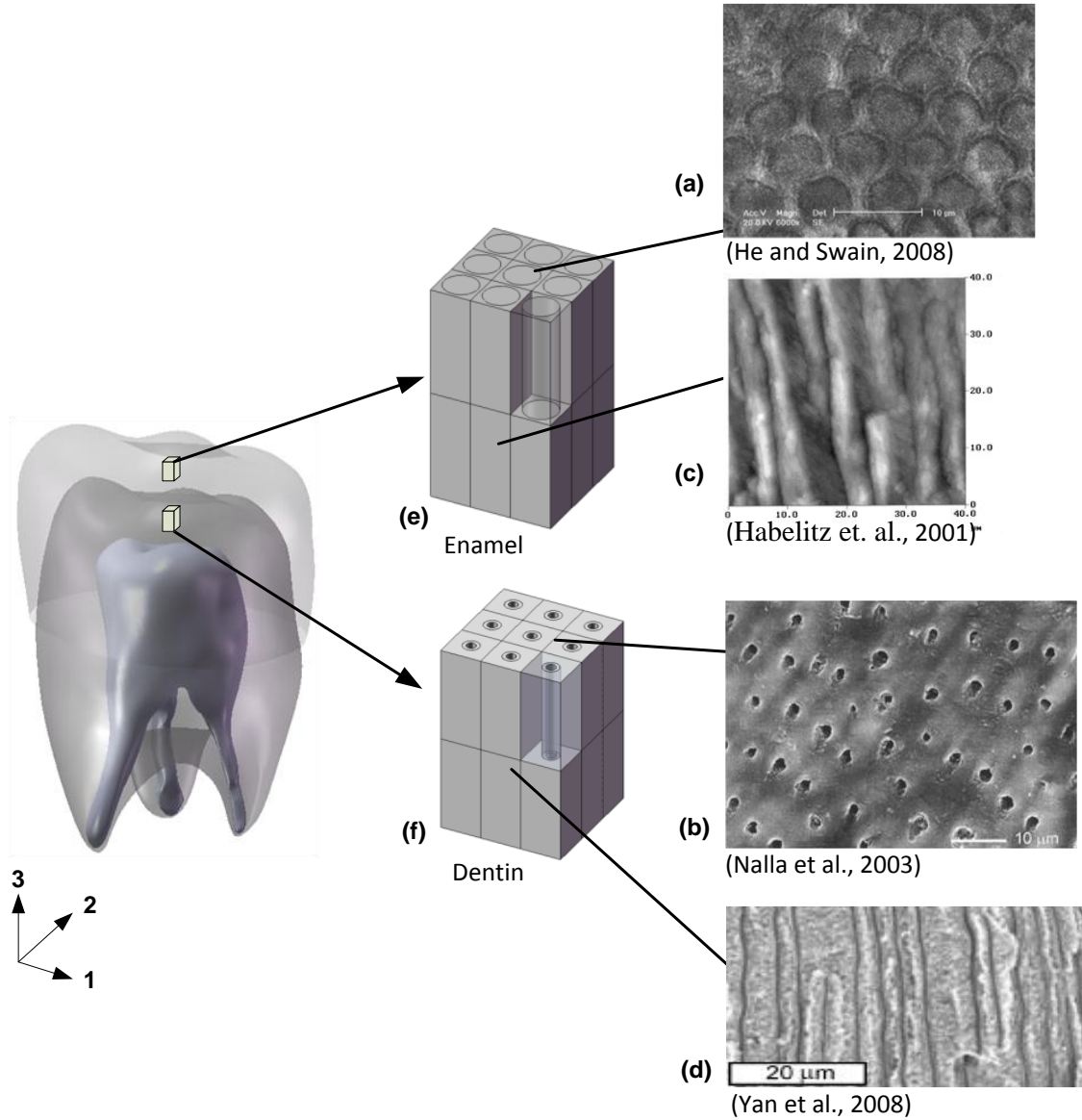


Figure 4.1: SEM images in different sectional views of enamel and dentin in micro-scale

In view of the hierarchical structure of enamel and dentin, unit cell models have been designed to investigate their anisotropic mechanical behavior from their isotropically behaved constituents. The models for enamel and dentin are biphasic and are represented by 3D solid models using CAD software package, SolidWorks® Office Premium 2007,

as shown in Figure 4.1(e) and 4.1(f) respectively. The enamel model consists of the rod and interrod phases while dentin consists of peritubular and intertubular phases. The 3D solid models have been converted to become a FE repeated cell model using the technique previously developed by investigators (Spears 1997; Fan et al., 2004a,b; Tsui et al., 2004; 2005; 2006). Using this technique, the complete 3D solid models are partitioned into repeated cells of a similar structure for FE analysis to determine the nodal displacement and velocity vectors. On application of the FE software (Abaqus 6.8-1) to the heterogeneous mechanistic descriptions of the isotropic elastoplastic properties of the material elements representing the micro-cell models, anisotropic elastoplastic stress-strain relations of enamel and dentin can be determined through conducting uniaxial tensile and shear simulations.

Another aim is to determine the isotropic elastoplastic properties of the four micro-scale constituents of a tooth, which are utilized to define the material properties of different phases in the cell models. This is done through combining nanoindentation, finite element modeling, and artificial neural network techniques. The elastic moduli of the constituents are firstly calculated using the method proposed by Oliver and Pharr (1992). The artificial neural modeling technique has been employed for the functional approximation between the nanoindentation load-displacement responses and the elastoplastic mechanical properties. Four neural networks have been built, and the data obtained from the finite element analyses have been utilized for network training and validating. Based on the neural models, the desired mechanical properties of the four tooth constituents have been determined.

4.1. Determination of the Isotropic Elastoplastic Parameters of Micro-scale Tooth Constituents

4.1.1. Nanoindentation Experiment

Nanoindentation experiments were performed using a Triboscope Nanomechanical Testing System (Hysitron, Minneapolis, MN). An optical microscope was utilized to observe the morphology of specimen surface and make indentations on the desired locations. A Berkovich indenter, a three-sided pyramid with a total included angle of 142.2 degrees, was used. Surface topology can be measured without causing any damage to the surface using the in situ imaging method through applying a very light loading force (0-1 μ N). Nanoindentation tests were then conducted using a loading and unloading rate of 500 μ N/s. The loading time, holding time, and unloading time were 5s, 3s, and 5s respectively. The maximum loading was 2500 μ N.

Concerning the nanoindentation experiment, indentation responses are usually quantified using the loading-unloading curve. A schematic illustration of a typical loading–unloading curve is shown in Figure 4.2, where P_{max} , h_l , h_h , and h_u , are maximum indentation load, maximum indentation depth in the loading phase, maximum indentation depth in the holding phase, and final indentation depth in the unloading phase, respectively. Figure 4.3 shows a schematic representation of the indentation describing a variety of quantities used in the analysis. The area under the loading curve is called the work in the loading phase W .

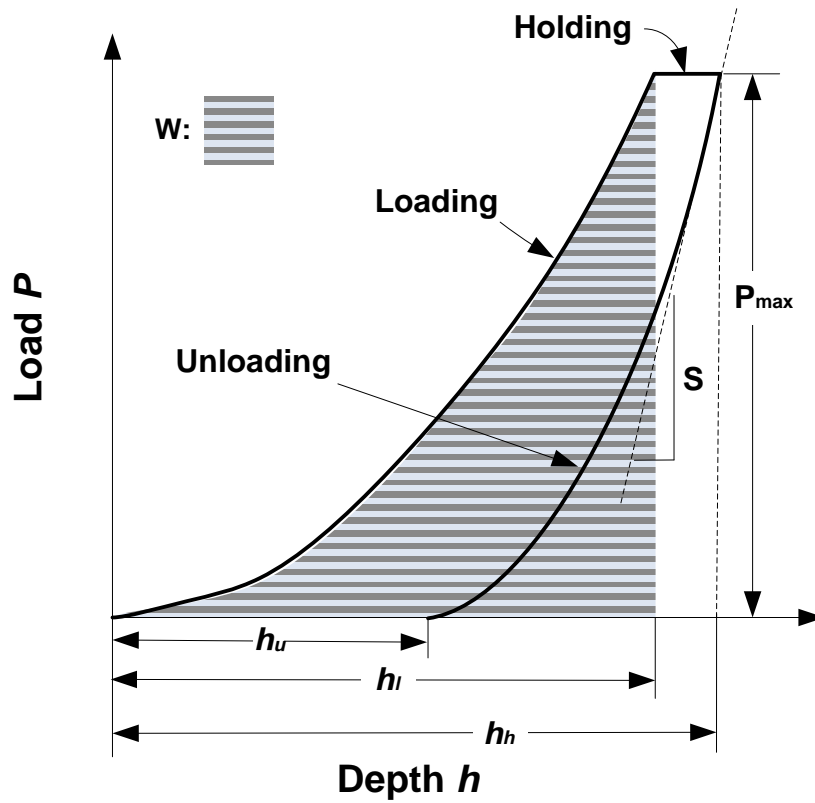


Figure 4.2: A typical load-displacement curve

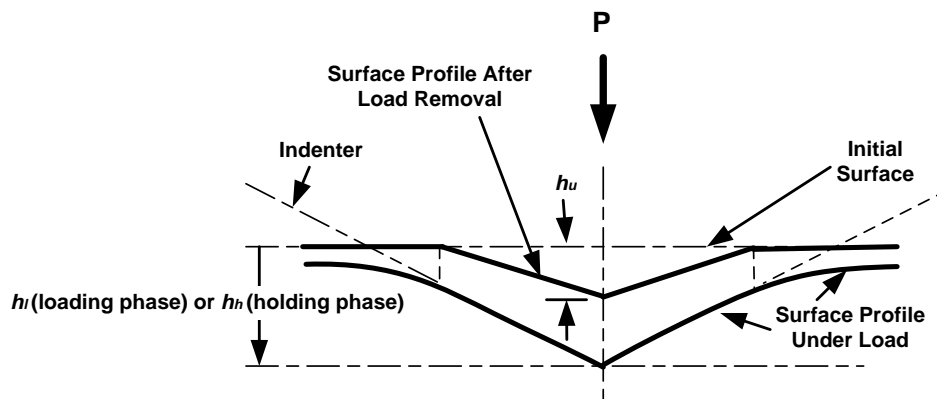


Figure 4.3: A schematic representation of indentation showing a variety of quantities used in the analysis

Regarding indentation theories, the loading-depth response in general follows Kick's law as stated below (Sneddon, 1965), in the loading phase:

$$P = \alpha h_i^2 \quad (4.1)$$

where α is a material constant which does not depend on the indentation depth but depends on the geometry of the indenter tip and material properties. At the peak load of the unloading phase, the unloading curve slope gives a measure of the contact stiffness, which can be utilized with the area of contact to calculate the reduced elastic modulus (E_r) (Bulychev et al., 1975; 1976). Using the Oliver-Pharr formulation for contact mechanics, the elastic modulus of the indented material can be calculated through using the experimentally obtained reduced modulus.

$$\frac{1}{E_r} = \frac{(1-\nu_i^2)}{E_i} + \frac{(1-\nu_s^2)}{E_s} \quad (4.2)$$

The subscript i and s indicate the indenter material and testing specimen respectively. For a diamond indenter tip, E_i is 1140 GPa and ν_i is the Poisson's ratio having a value of 0.07.

Indentation tests were performed on the enamel and dentin of the specimen in ambient air. To investigate the indentation responses of dentin, indentation tests were conducted along the bucco-lingual cross section surface of dentin irrespective of tubule orientation and location, as depicted in Figure 4.4. For enamel, indentation tests were conducted along the bucco-lingual cross section of the enamel as well as the bucco-lingual side surface. On the enamel, indentations were made irrespective of the rod and interrod constituents. To make consecutive indents, the current nanoindentation apparatus offers freedom of

movement for specimens in the translation dimension. Conventionally, to collect the n -th number of indentation responses on the convex curved surface of a material, n specimens need to be prepared. To save time and the cost involved in preparing multiple specimens for the collection of the indentation responses of enamel along the curved bucco-lingual side surface, a fixture with a rotational degree of freedom was designed and used, as shown in Figure 4.5. To use the fixture in performing multi-indentations, it was placed on the sample holder of the indentation device while the specimen was mounted on the sample holder of the fixture.

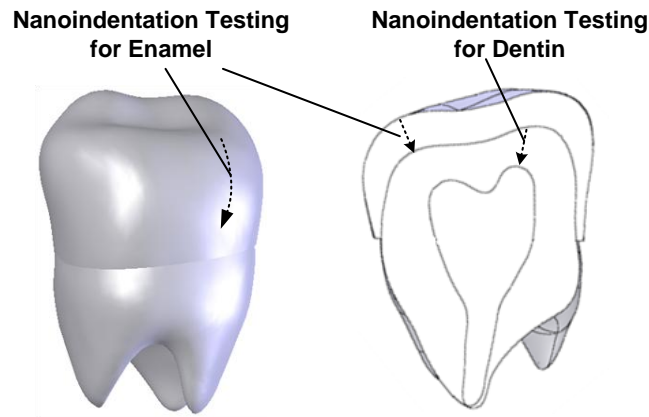


Figure 4.4: Schematic diagram illustrating the indentation paths for nanoindentation tests

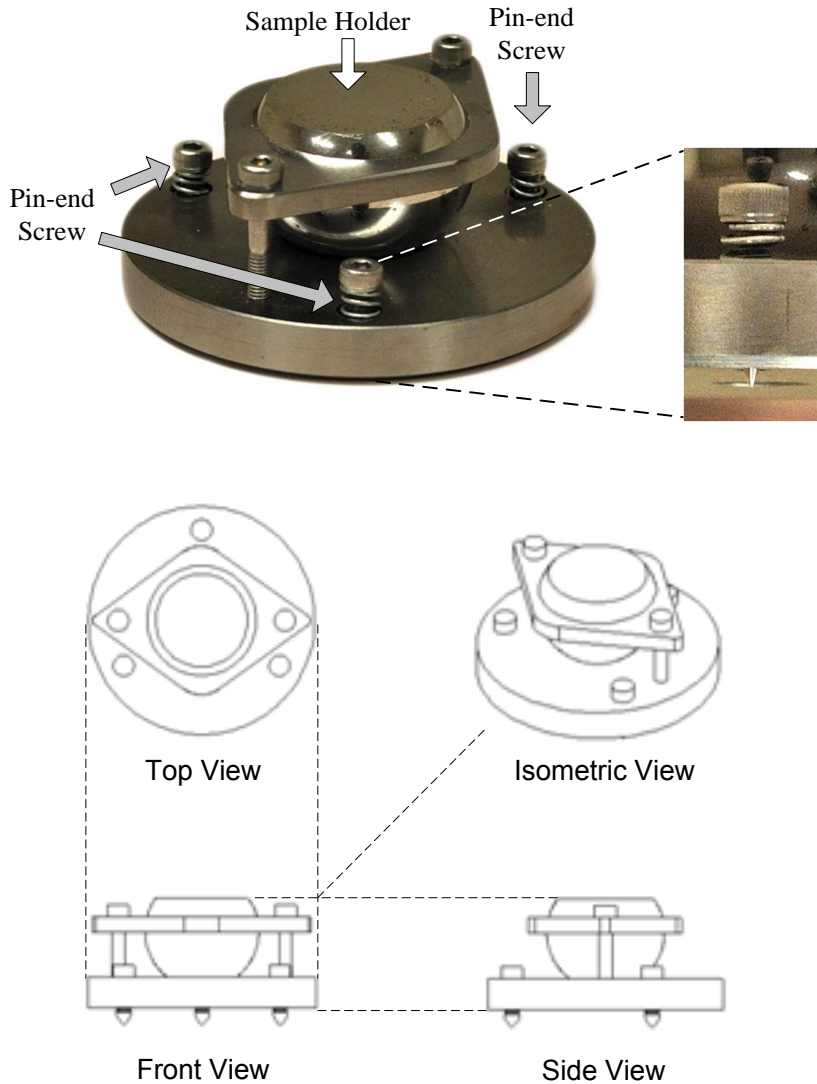


Figure 4.5: The designed fixture for measuring indentation responses of specimens with curved surfaces

The designed fixture contains three pin-end screws, which can be adjusted and can hold a specimen stationary, like the principle of a tripod. The ball-shaped sample holder is capable of rotating to give a robust adjustment of the specimen while the three screws are for refining adjustment to tilt the targeted curved surface to a level favorable for

performing the indentation. For each adjustment, a computational program is run to move the nanoindenter around the targeted region. A favourable condition is assumed to be fulfilled when no crashing is detected between the indenter and the specimen. Through the use of the rotational equipment, multi-indentations were made on the bucco-lingual surface of the enamel in one prepared specimen. On the other hand, to conduct nanoindentation testing on the cross-sectional surface of the tooth specimen, a computational program was written to drive the nanoindenter to perform the indentation automatically. For consecutive indents, they are separated by at least 80 μm to avoid the indentation response being affected by the hardening caused by the previous indents.

To characterize the representative indentation responses of the micro-scale tooth constituents, two processes have been carried out due to the structural characteristics of enamel and dentin. In the dentin region, tubule lumen is exhibited as a cylindrical hollow. Besides, as a natural material, the peritubular and intertubular constituents in dentin as well as the rod and interrod constituents in enamel are bounded seamlessly. Thus, the collected indentation responses may be located purely at a constituent, or near the edge of the hollow tubule (Figure 4.6(a)), or near the interface of the constituents (Figure 4.6(b)). It is obvious that the obtained indentation responses are affected when indentations are not made purely at a constituent.

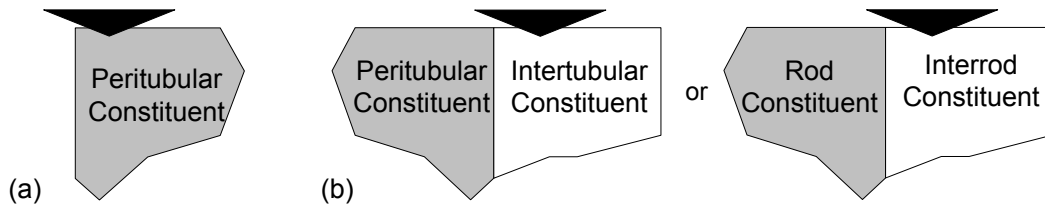


Figure 4.6: Indentations being made (a) near the edge of the hollow tubule and (b) near the interface among the constituents

For the case of having an indent near the edge of the hollow tubule, it is expected that the loading curve would not follow the Kick's law, as shown in Figure 4.7. To exclude such effects, all the obtained loading curves were fitted with the Kick's law, equation (4.1), and indent data having a coefficient of determination (R-squared) less than 0.9 were filtered. The Oliver-and Pharr method (1992) was then used to manipulate the remained experimentally obtained data to the required elastic modulus. Figure 4.8 shows the variations of the calculated elastic moduli in the enamel region with respect to their relative distances from occlusal edge to DEJ along the bucco-lingual section surface, while Figure 4.9 depicts those of dentin with respect to their relative distance from DEJ to the pulp, along the bucco-lingual section surface.

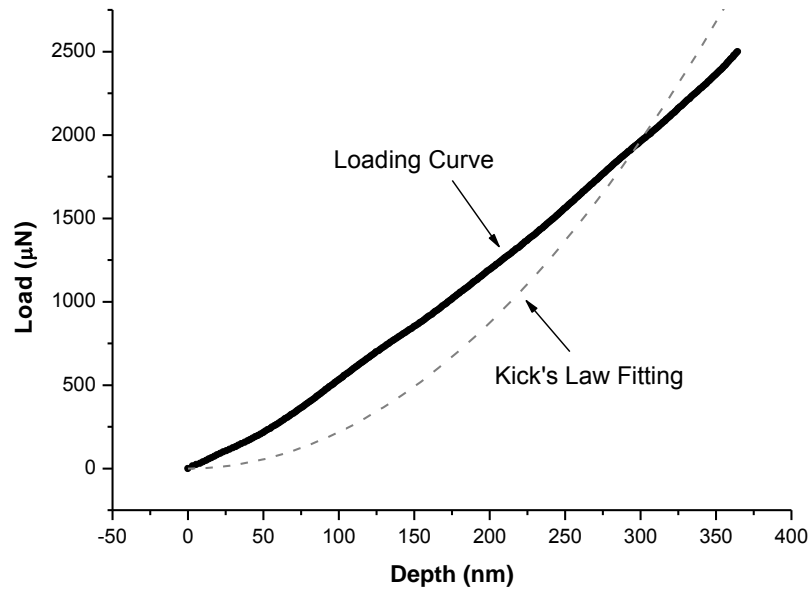


Figure 4.7: Loading curve for a nanoindent located near a free edge

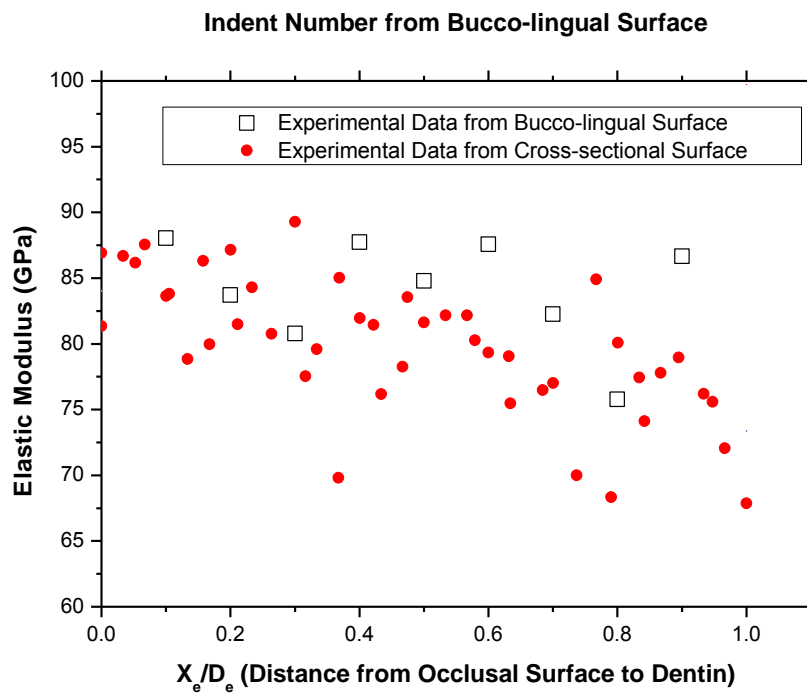


Figure 4.8: Calculated elastic modulus of enamel along the bucco-lingual surface and cross-sectional surface

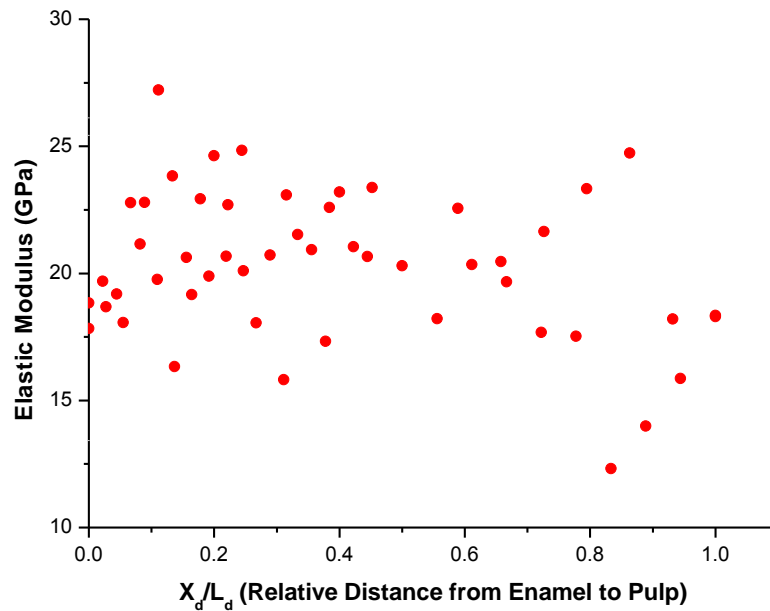


Figure 4.9: Calculated elastic modulus of dentin versus relative distance from DEJ to pulp

For the case of having an indent near the interface of the constituents, it is supposed that they would have an intermediate elastic modulus value. From the literature, it is known that in the enamel region, the elastic modulus of the rod has a larger value than the interrod, with variations of 6% and 3% respectively (Habelitz et al., 2001). For the dentin region, the elastic modulus of the peritubular constituent gives a higher value than the intertubular constituent, with variations of 2% and 4% respectively (Kinney et al., 1999). The representative elastic modulus of the rod, interrod, peritubular, intertubular constituents were then obtained accordingly through calculating the average, as shown in Table 4.1. The modulus values were within the ranges reported from 1961 to 2008 for the

experimental observation of enamel (Craig et al., 1961; Roy and Basu, 2008), and from 1952 to 2011 for dentin (Peyton et al., 1952; Ziskind et al., 2011). The representative indentation responses of the constituents in the enamel and dentin regions are shown in Figure 4.10.

Table 4.1: The representative elastic moduli of the four tooth constituents

	Elastic Modulus (GPa)
Rod Constituent	86.60
Interrod Constituent	69.61
Peritubular Constituent	27.21
Intertubular Constituent	12.32

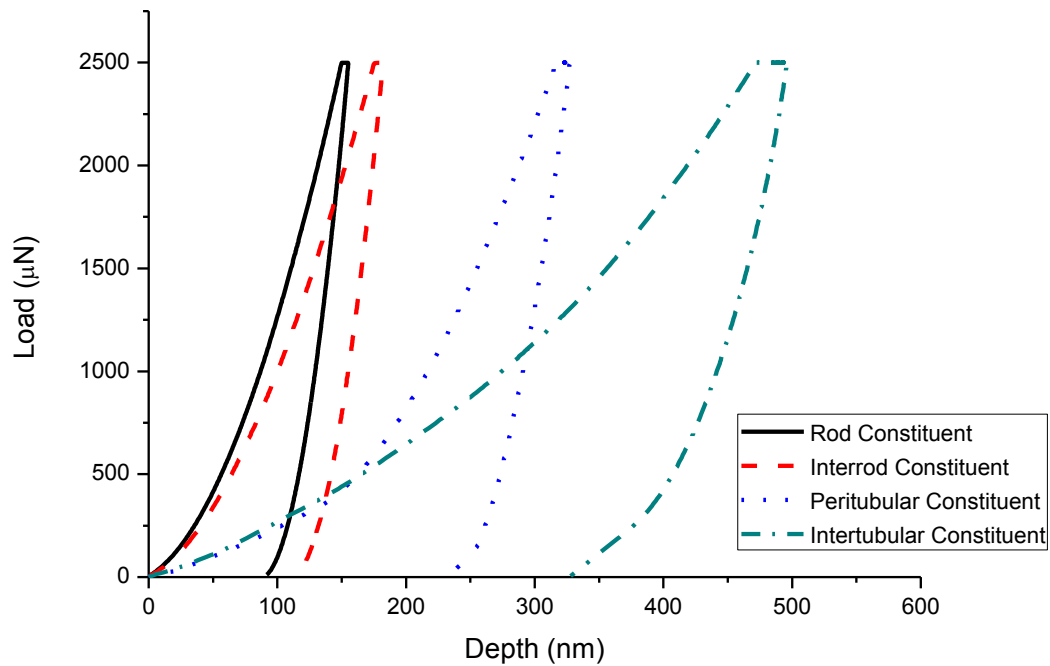


Figure 4.10: The representative indentation responses of tooth constituents

4.1.2. Finite Element Modeling of Indentation

Numerical finite element models were constructed to mimic the nanoindentation experiment and simulate the indentation responses of elastoplastic behaved materials. FE analysis was adopted due to its capability in offering an efficient channel to examine the indentation responses of the specimens. In addition, the effects of different specimen properties on the indentation responses can easily be investigated through assigning interested material description parameters to the indentation computation model. The FE analysis simulations were performed using the commercial software package, Abaqus 6.8-1. Since the considered indentation analysis is a contact problem, large deformation theory with geometrical and material non-linearity was adopted.

To mimic the nanoindentation experiment, 3D FE models were constructed to simulate the nanoindentation response of elastoplastic material using a Berkovich indenter. The geometry of the indenter is shown in Figure 4.11(a). It is a three-sided (triangular-based) pyramidal diamond and has an angle of 76.9° between the edge and normal, and was a nominal angle of 130.6° between the edges in the side face. The indenter has been defined as a rigid body with a perfectly sharp tip and meshed with R3D4 elements. The whole indenter is modeled with the aim of visualization. Figure 4.11(b) illustrates the FE model adopted for nanoindentation. Bucaille et al. (2003) and Balać et al. (2006) pointed out that specimen models having dimensions of $L=R=20\mu\text{m}$ are large enough to approximate the behavior of a semi-infinite half-space. In terms of ratios, it has been reported that the diameter of the specimen should be at least 50 times larger than the maximum indentation depth, i.e., $2R/h_n \geq 50$. This ratio has been identified as the rule to follow in constructing the indentation models. Due to the symmetry of the Berkovich

indenter, only one-third of the specimen is modeled. The one-third cylindrical model is meshed using C3D8R brick solid elements. To save computational time, a finer mesh was utilized near the indenter contact region and gradually coarser meshes were adopted in the region away from contact. Symmetrical boundary conditions were defined in the two end planes. The bottom plane of the indented material was constrained in the axial direction. The FE model was determined to be insensitive to far field boundary conditions and well-tested for convergence.

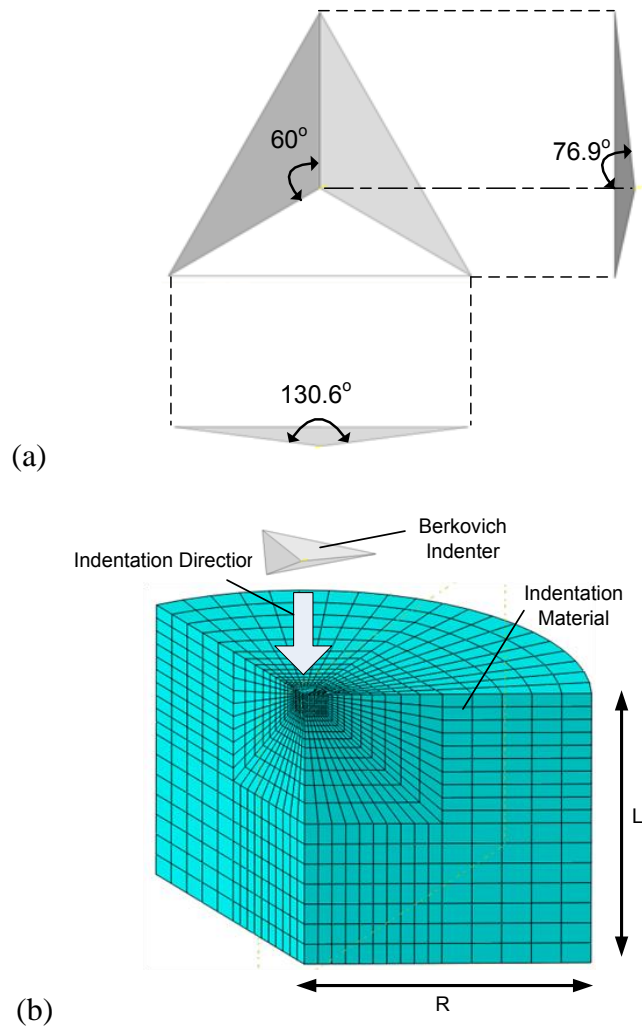


Figure 4.11: (a) Geometry of the Berkovich indenter; (b) A schematic illustration of indentation FE model

The specimen models for the four tooth constituents were modeled as isotropic elastoplastic solids using the power law plasticity model with the von Mises criterion.

The constitutive behavior of the material utilized for FE modeling can be defined as:

$$\sigma = \begin{cases} E\varepsilon, & \sigma \leq \sigma_y \\ R\varepsilon^n, & \sigma \geq \sigma_y \end{cases} \quad (4.3)$$

where E , R , and n are the elastic modulus, strength coefficient, and strain hardening exponent respectively. σ_y is the initial yield stress while ε_y is the corresponding yield strain such that:

$$\sigma_y = E\varepsilon_y = R\varepsilon_y^n \quad (4.4)$$

The total effective strain ε comprises two parts ε_y and ε_p as follows:

$$\varepsilon = \varepsilon_y + \varepsilon_p \quad (4.5)$$

where ε_p is the nonlinear plastic part of the total effective strain accumulated beyond the yield strain. The incremental theory of plasticity with von Mises effective stress (J_2 flow theory) is assumed. When $\sigma > \sigma_y$, the total effective stress can be expressed as follows, through substituting equation 4.4 and 4.5 into equation 4.3.

$$\sigma = \sigma_y \left(1 + \frac{E}{\sigma_y} \varepsilon_p \right)^n \quad (4.6)$$

Concerning Poisson's ratios, they have been presumed for the four tooth constituents. Cheng and Cheng (1999), Mesarovic and Fleck (2000), Tunvisut et al. (2001), Cheng and Cheng (2004), and Luo and Lin (2007) have claimed that Poisson's ratio is a minor factor in indentation experiments. They have also stated that it is impossible to predict an

accurate Poisson's ratio using the nanoindentation technique and most of the engineering materials have $\nu \approx 0.3$. Hence, 0.3 was chosen as Poisson's ratios for modeling purposes.

For each of the tooth constituents, a parametric study of 60 simulations was conducted. The elastic moduli E for the four constituents were defined according to the experimental findings as stated in Table 4.1. He and Swain (2009) have regarded tooth material as a metallic-like deformable bio-composite, while Dao et al. (2001) stated that the minimal yield stress value for metals and alloys is 30 MPa. The simulation cases were adopted with σ_y ranging from 30MPa to 1GPa and n ranging from 0 to 0.8.

The effect of indentation friction has been examined by Mesarovic and Fleck (2000), Cheng and Cheng (2004), and Wang and Rokhlin (2005). It has been observed that friction has a very minor effect, so a friction coefficient value of 0.1 (Coulomb's friction law) was adopted between the contact surfaces (Zhao et al., 2006; Yan et al., 2007).

4.1.3. Artificial Neural Modeling

Artificial neural network (ANN) models were used for the inverse mapping of indentation responses to plastic properties of the four tooth constituents. The ANN model is a parallel processing architecture composing interconnected processing elements, called neurons, organized in hidden layers. The ANN modeling technique is adopted due to its capability to learn and generalize from examples and experiences, as well as to adapt to changing circumstances after a training procedure. Such technique is not only good at mapping effect from cause for prediction, it is also characterized to map from effect to possible causes (Jenkins, 1997). A feed-forward back-propagation supervised

training model is designed by using an ANN package, MATLAB 6.5. The establishment of proper ANN architecture depends on the problem to be represented by the network. In general, two procedures are involved, namely, design and training.

The basic aim of the design procedure is to identify the input and output quantities. It is observed that using the finite element modeling technique to mimic the indentation experiment for the four tooth constituents, indentation responses (α , h_l , h_u , and W) vary when the plastic characteristics of the indented material change (σ_y and n). Since the purpose is to determine the plastic properties of the specimen inversely, σ_y and n are assigned as the output quantities. As input quantities, the material constant α , maximum indentation depth in the loading phase h_l , final indentation depth h_u , and loading work done W were considered. To minimize the effect of the roughness of the specimen, the two inputs, h_l and h_u , were combined as a quantity, i.e. $h_l - h_u$.

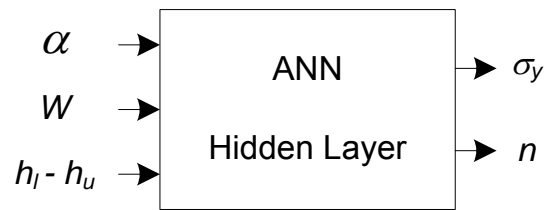


Figure 4.12: Mapping of input and output quantities

The training procedure aims at adjusting the NN characteristics which include the quantity of hidden layers, the quantity of neurons in each hidden layer and the values of the connections/ weight between neurons. Thus, the best architecture of ANN is unknown in advance. During the training procedure, adjustments were made on the weights of the connections having the purpose to minimize the discrepancies between the network outputs and the targeted outputs, as shown in Figure 4.12. Each neuron owns a weighted sum of the inputs p_i which are the outputs from the neurons in the prior layers and a threshold value b_i as follows:

$$q_s = \sum_{i=1}^R w_i p_i + b_i \quad (4.7)$$

where w_i is the network weight and R is the number of elements in the previous layer, as shown in Figure 4.13. The input signals accumulated are activated by a function to generate an ANN output y_m as below:

$$y_s = f(q_s) \quad (4.8)$$

The sigmoid activation function, equation (4.9), has been adopted because it is capable of describing nearly constant, linear, and curvilinear behavior.

$$f(q_s) = \frac{2}{1+e^{-2q_s}} - 1 \quad (4.9)$$

ANN modeling for indentation was to establish functional relationships among the input and output quantities, which represents indentation responses versus plastic properties of materials. Such knowledge is represented and stored through the weights of internal connections among neurons (Hambi et al., 2006).

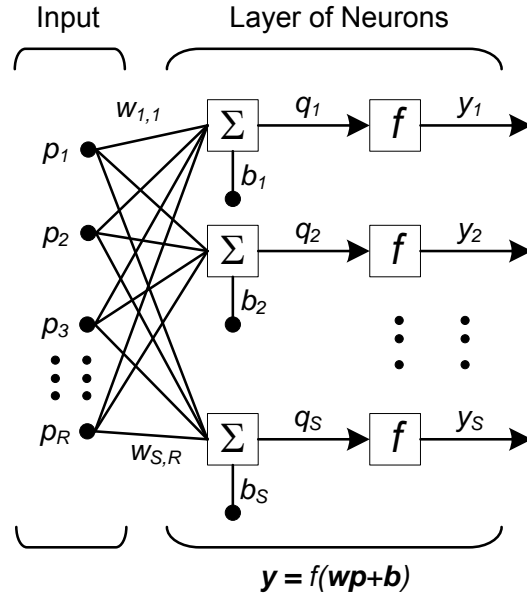


Figure 4.13: A hidden layer of an ANN model with S neurons and R inputs

4.1.4. Results and Discussions

Using the indentation finite element modeling technique, indentation responses of the four tooth constituents with different plastic properties have been simulated. Figure 4.14 shows an example of the von Mises stress distribution of an indentation model with parameters describing the mechanical behavior of the peritubular constituent, having σ_y and n equal to 30MPa and 0.2 respectively, during the indentation process of the initial, maximum loading, and fully unloading stages. Facilitated by the indentation model, the required indentation responses for ANN modeling could be obtained through tracing the indentation depth with the load history. For illustration purpose, Figure 4.15 shows the numerical results representing the peritubular constituent, with σ_y of 30MPa and 90MPa. It is observed that indentation materials with the same E and σ_y under the same load

would give a higher value of h_l for a lower n value. For materials having the same E and n values, h_l decreases proportionally to σ_y . Figure 4.16 describes the changes for h_u with variation of σ_y and n . In general, for indentation material with the same E and n values but a lower σ_y , a higher h_u is observed. On the other hand, h_u illustrates a decreasing trend while n is raised.

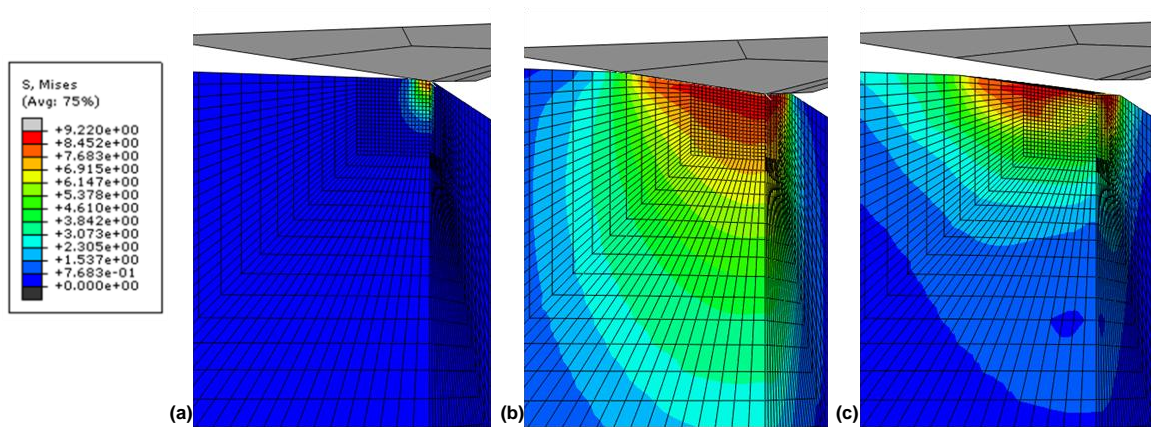


Figure 4.14: The von Mises stress distribution of the FE model with a mechanical parameter set of ($E=27.21\text{GPa}$, $\sigma_y = 30\text{MPa}$, $n=0.2$) in the period of (a) $t=0.5\text{s}$, (b) $t=5\text{s}$, (c) $t=13\text{s}$

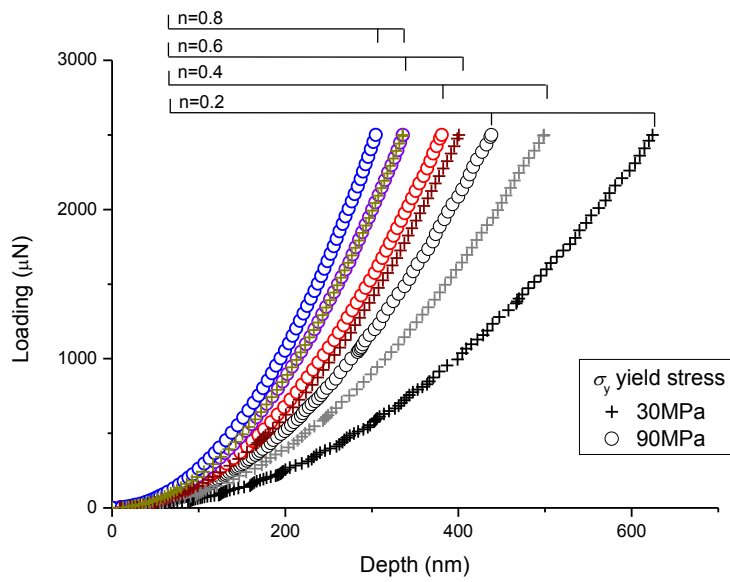


Figure 4.15: Examples of the indentation loading curves obtained from FE analysis for the peritubular constituent having various plastic properties

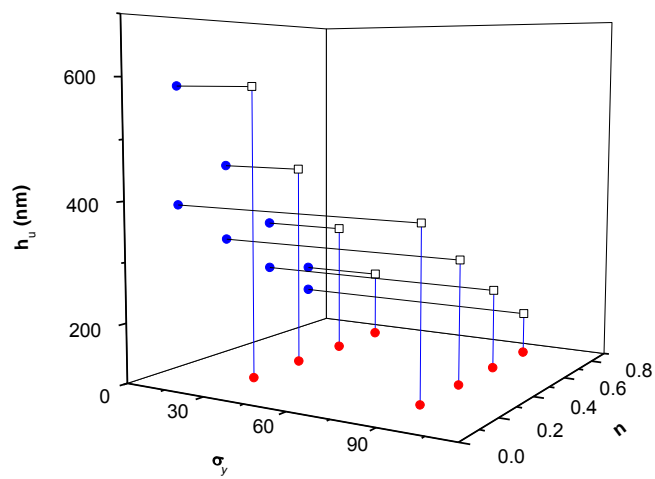


Figure 4.16: Changes of final indentation depth h_u for a peritubular constituent with various σ_y and n values

FE simulation results supply the training data for artificial neural network modeling. Training of different ANN architectures for the four tooth constituents was based on 240 datasets. As discussed in the FE modeling procedures, the four constituents were modeled with experimentally determined E while σ_y ranged from 30MPa to 1GPa and n ranged from 0 to 0.8. These datasets were obtained by collecting different indentation responses which correspond to different material plastic properties.

To evaluate the abilities of different ANN architectures in generalizing the effects of input quantities (α , $h_l - h_u$, and W) on the output quantities (σ_y and n), a testing procedure was performed. A total of 80 test datasets for the four constituents were formed and extracted similarly from the indentation FE analyses but were not used for the training procedure. This means the datasets were unknown to the trained ANN models with different architectures. Figure 4.17 illustrates the percentage error values between the output σ_y from prediction using two example trained ANN architectures and the test datasets, while Figure 4.18 presents those for n . In general, ANN architecture B gives lower percentage error in prediction than architecture A. Thus, architecture B is more suitable for plastic properties prediction. The preferred ANN architecture for the four tooth constituents was identified for each of the constituents when the average of percentage error (APE) was obtained with minimum value among the trained ANN architectures, defined as follows:

$$APE = \frac{1}{T} \frac{1}{N} \sum_{t=1}^T \sum_{i=1}^N \left(\frac{O_i - D_i}{O_i} \right)^2 \quad (4.10)$$

where T , N , O_i , and D_i are the total number of test datasets, number of output nodes, output quantity predict from the ANN architecture, and the corresponding desired output

from the datasets respectively. The preferred architecture was selected with an APE value of 9%.

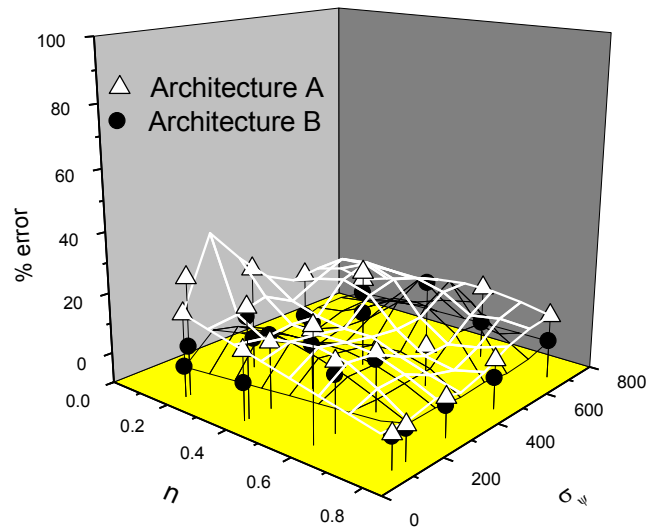


Figure 4.17: The squared normalized error values between the output yield stresses from prediction using various trained ANN architectures and the tested datasets

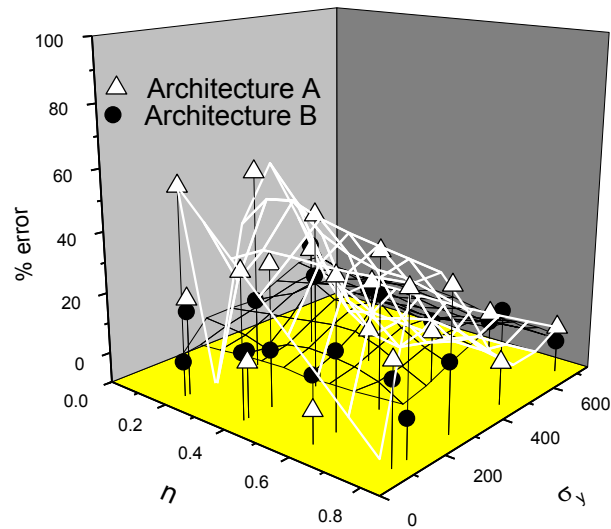


Figure 4.18: The squared normalized error values between the output hardening index from prediction using various trained ANN architectures and the tested datasets

After the ANN models for the four tooth constituents were satisfactorily trained and tested, they were able to generalize functional rules and responses to input quantities in order to predict the required plastic properties. Through the established functional relationships for the four different tooth constituents using the ANN modeling, the desired plastic properties (Table 4.2) can be found through inputting their represented indentation responses. The determined plastic yield stresses for the rod and interrod constituents within the enamel region are reasonable, and fall within the range from 330MPa to ~0.9GPa (Staines et al., 1981; Ang et al., 2010) while the peritubular and intertubular constituents within the dentin region fall within the range of 75MPa to 159MPa (Nalla et al., 2003; Yan et al., 2008). This has demonstrated the feasibility of

integrating nanoindentation, finite element modeling, and artificial neural network modeling techniques to determine the plastic properties of peritubular and intertubular constituents of dentin.

Concerning the hardening index, experimental data can hardly be found in the open literature. Due to the lack of knowledge about this parameter, dentin always assumed as elastic isotropic materials. The proposed method offers a scientific means for the determination of the hardening index, where it is difficult to quantify using conventional testing method.

Table 4.2: The determined plastic properties of the four tooth constituents

	Yield Stress σ_y (MPa)	Hardening Index n
Rod Constituent	952	0.11
Interrod Constituent	363	0.2
Peritubular Constituent	157	0.43
Intertubular Constituent	100	0.21

The determined elastoplastic isotropic properties of the four tooth micro-constituents in the micro-scale were then utilized to predict the elastoplastic anisotropic properties of enamel and dentin in the macro scale. The unit cell modeling method, which is capable of predicting the macroscopic mechanical properties of enamel and dentin using their constituents, with considerations of their geometry and size effects, was employed. Through performing tensile and shearing tests using the unit cell models, with the aid of

the finite element technique, the required parameters for describing the anisotropic elastoplastic behavior of macroscopic enamel and dentin can be found.

4.2. Determination the Anisotropic Stress-strain Relations of Enamel and Dentin

4.2.1. Finite Element Modeling

4.2.1.1. Representative Volume Element for Enamel and Dentin

As presented in Figure 4.1, macroscopic enamel and dentin are regarded as composites with continuous fiber reinforcements, which are assumed to have even distributions. Based on this assumption, macroscopic enamel and dentin are regarded being comprised of repeating units, i.e. representative volume elements (RVE).

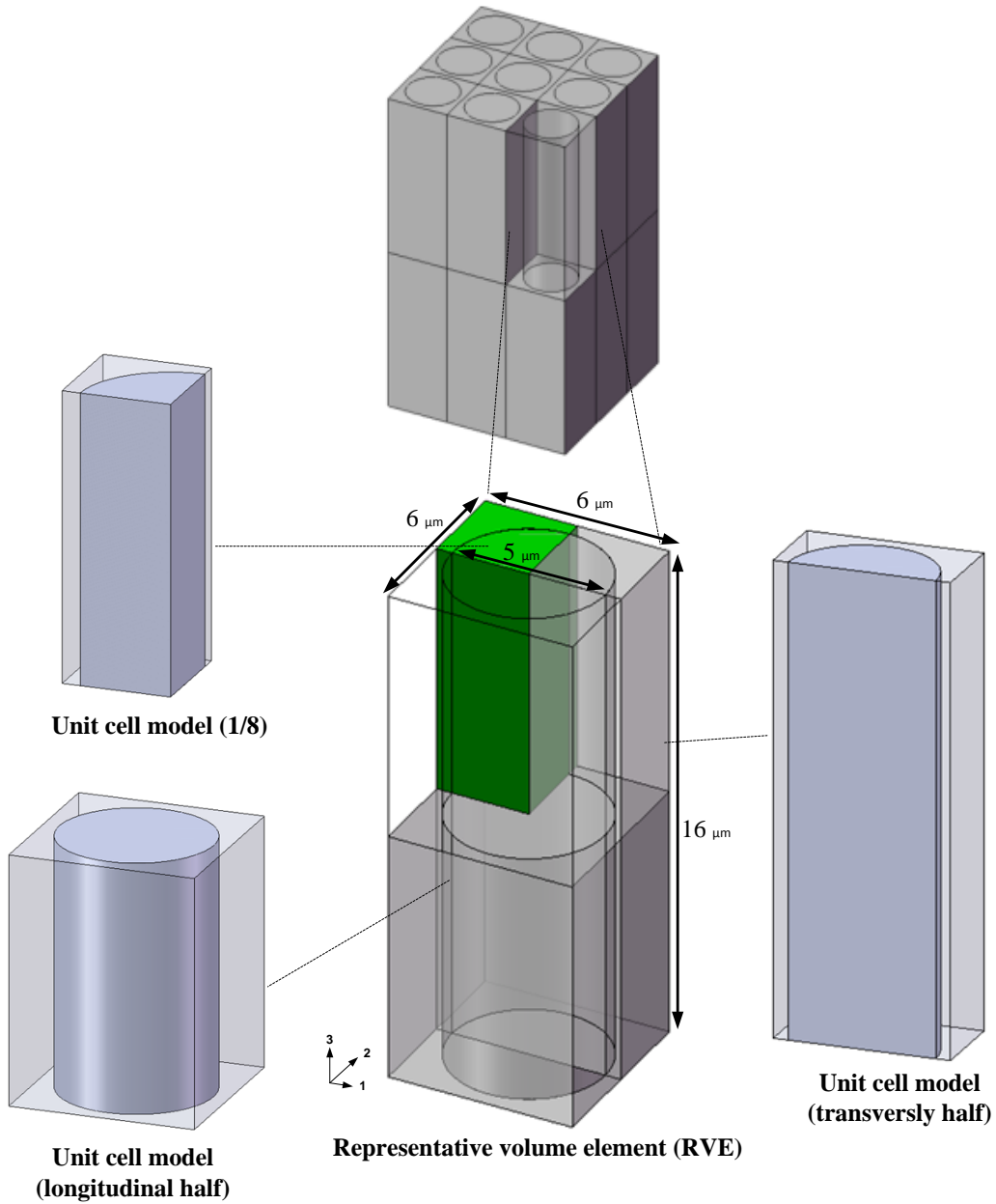


Figure 4.19: The unit cell models for enamel

RVE of enamel is shown in Figure 4.19. The RVE enamel model comprises two phases, a matrix phase representing the interrod region and a fiber phase depicting the rod region. After review of the literature (Simmelink, 1987; Spears, 1997; He et al., 2008), the dimensions of the RVE are set as follows: the diameter of the fiber phase is 5 μm; the

minimum distance between the fiber and the edge of the matrix phases is $0.5 \mu\text{m}$; and the height is $16 \mu\text{m}$.

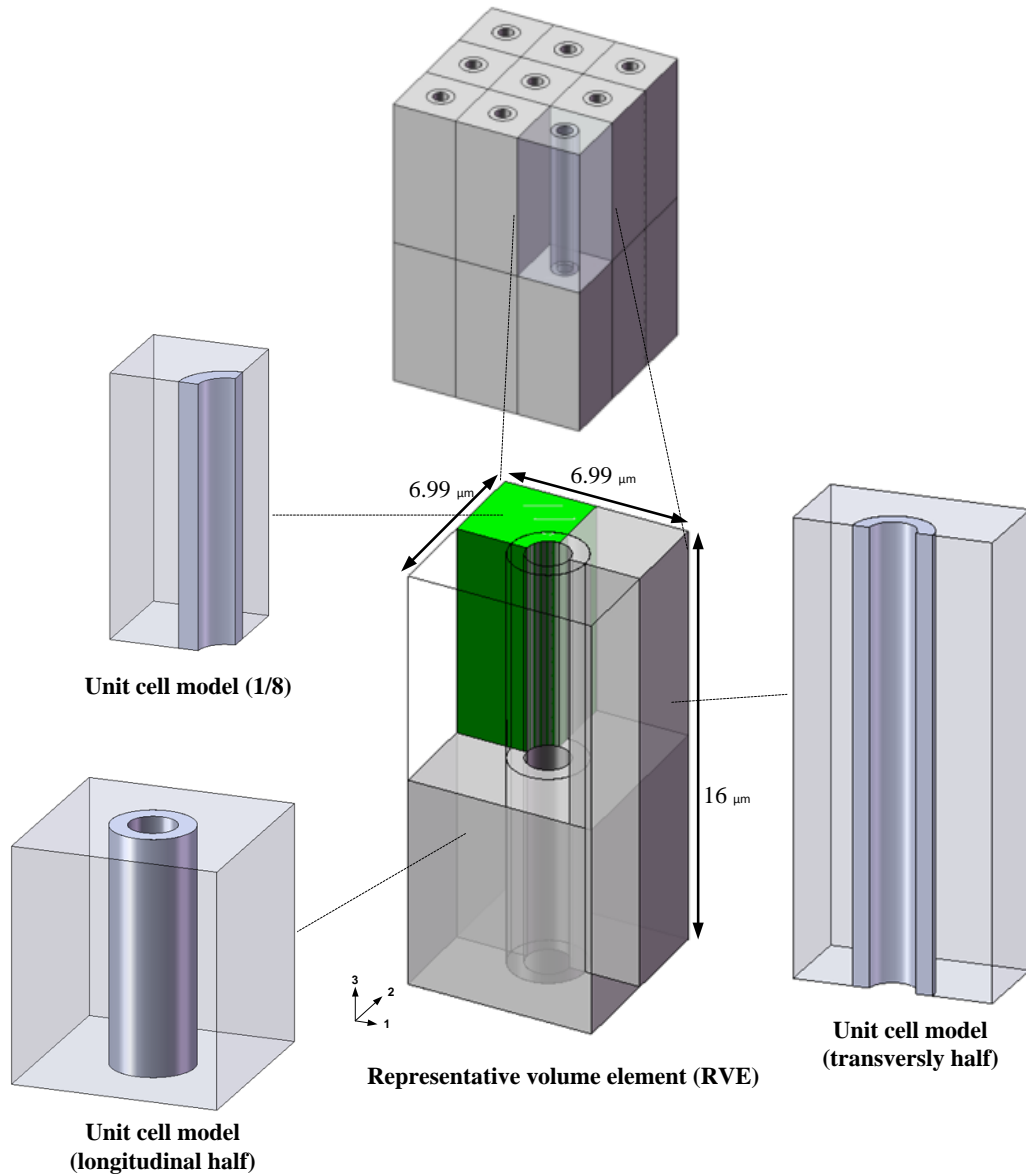


Figure 4.20: The unit cell models for dentin

RVE of dentin is illustrated in Figure 4.20. Similarly, the RVE dentin model consists of two phases, a matrix phase representing the interrod region and a hollow fiber phase

depicting the peritubular region. Through averaging the dimensions obtained from the literature (Garberoglio and Brannstorm, 1976; Pashley, 1948), the diameter of the dentinal tubule hollow, the diameter of the peritubular phase, and the width and the length of the RVE are set as 1.63 μm , 2.83 μm , 6.99 μm and 6.99 μm . Having a similar nature to enamel, the height of dentin RVE is set as 16 μm .

Because of the assumed symmetry for the packing of the fiber reinforcement, only part of the RVEs of enamel and dentin are utilized to construct the unit cell models for conducting uniaxial tensile and shear simulations respectively. In general, one-eighth of the RVE is used for the case of uniaxial stressing, while half of the RVE is used for the case of shearing. The unit cell models are assumed to have perfect bonding between the fiber and the matrix phases. In addition, the two phases are assumed to behave isotropically. The isotropic elastoplastic mechanical properties of the rod, interrod, peritubular, and intertubular phases are listed in Table 4.1. Applications of the partitioned cell models as well as the definitions of loading and boundary conditions for conducting the two tests are further discussed in detail below.

4.2.1.2. Tensile Testing

Figure 4.21 and Figure 4.22 show the two unit cell models constructed to represent enamel and dentin respectively. For each of the models, two uniaxial tensile tests along the direction-2 and direction-3 are simulated.

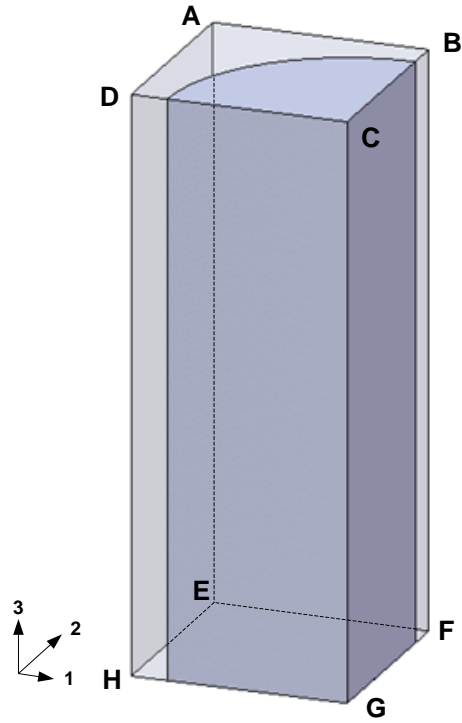


Figure 4.21: The one-eighth unit cell model of enamel for tensile test analysis

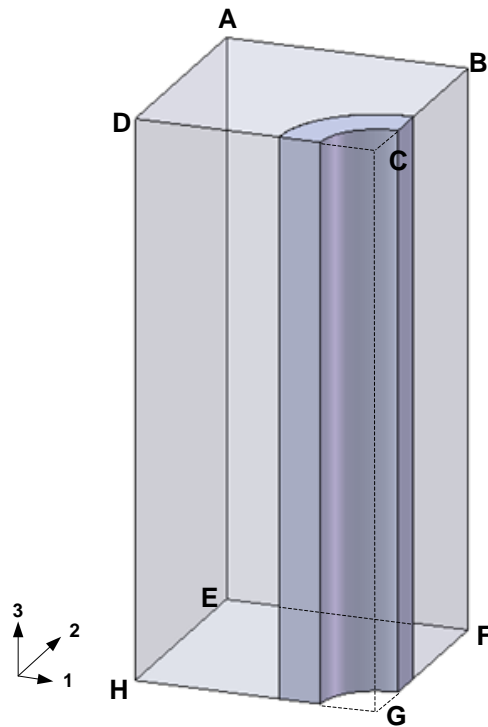


Figure 4.22: The one-eighth unit cell model of dentin for tensile test analysis

To conduct the tensile test along direction-2, tensile loading was applied on face ABEF in direction-2 through a prescribed displacement. Due to the assumption of the regular packing of particles in the unit cell model, faces CDGH, BCFG, and EFGH are fixed and the displacement in their normal direction is set as zero. On the other hand, faces ABCD, ABEF and ADEH are constrained to maintain planarity within the loading process. To mesh the unit cell models, 3D brick solid elements (C3D8) were used.

The tensile stress of the unit cell model $\bar{\sigma}_{22}$ is calculated using the formula below:

$$\bar{\sigma}_{22} = \frac{\int_A \sigma_{22} dA}{A} = \frac{\sum_{i=1}^n (\sigma_{22})_i A_i}{A} \quad (4.11)$$

where $(\sigma_{22})_i$ is the stress component in the i th element of the face ABEF with area A_i , and n is the total number of elements in the face ABEF.

On the other hand, the tensile strain of the model ε_{22} is defined as:

$$\varepsilon_{22} = \frac{(u_{22})_{face\ ABEF}}{l_{initial}} \quad (4.12)$$

where $(u_{22})_{face\ ABEF}$ is the prescribed displacement on the face ABEF and $l_{initial}$ is the initial length of the edge along the loading direction.

Similarly, to conduct the tensile test along direction-3, tensile loading was applied on face ABCD in direction-3 through a prescribed displacement, while the boundary conditions were defined exactly the same as the tensile test along the direction-2. The tensile stress $\bar{\sigma}_{33}$ and tensile strain ε_{33} are calculated using Equations (4.13) and (4.14) respectively.

$$\bar{\sigma}_{33} = \frac{\int_A \sigma_{33} dA}{A} = \frac{\sum_{i=1}^n (\sigma_{33})_i A_i}{A} \quad (4.13)$$

$$\varepsilon_{33} = \frac{(u_{33})_{face\ ABCD}}{l_{initial}} \quad (4.14)$$

4.2.1.3. Shear Testing

In the case of the shear test, half of the RVE is used for unit cell model construction. Figure 4.23 and Figure 4.24 present the longitudinal half of the unit cell models for enamel and dentin for conducting shear tests in the plane 1-2, while Figures 4.25 and 4.26 show the transverse half of the unit cell models for shearing in the plane 1-3. The unit cell models are meshed using the 3D brick solid elements (C3D8).

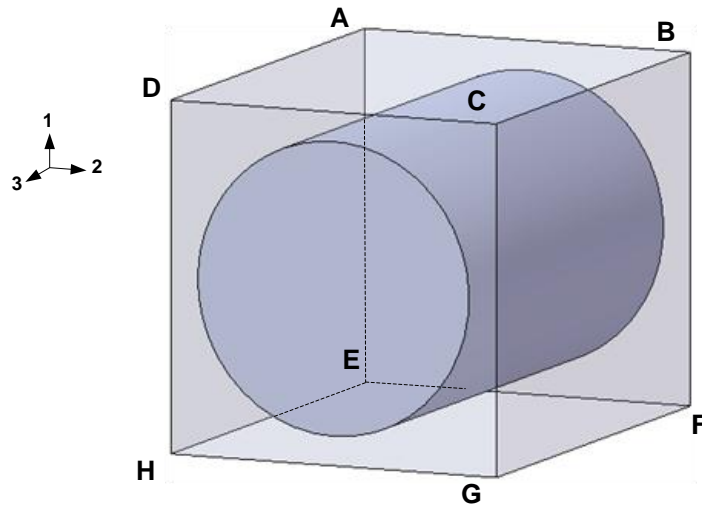


Figure 4.23: The longitudinal half unit cell model of enamel for shear test analysis

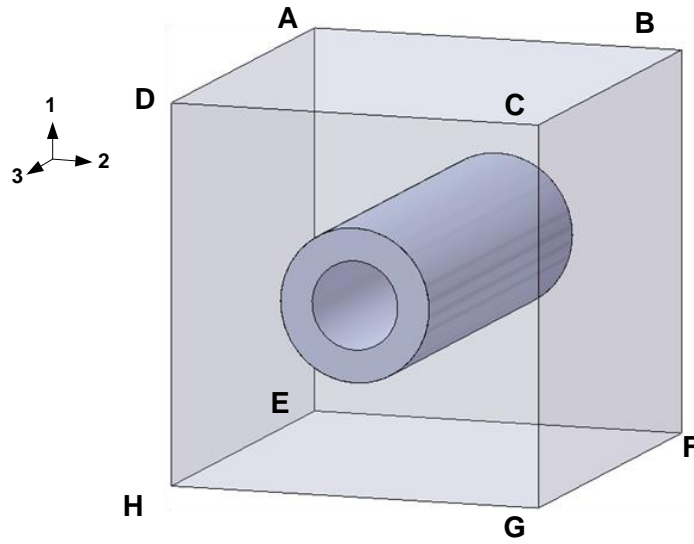


Figure 4.24: The longitudinal half unit cell model of dentin for shear test analysis

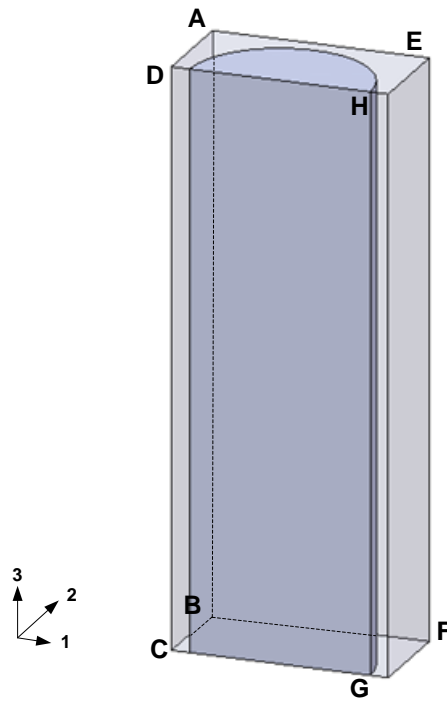


Figure 4.25: The transverse half unit cell model of enamel for shear test analysis

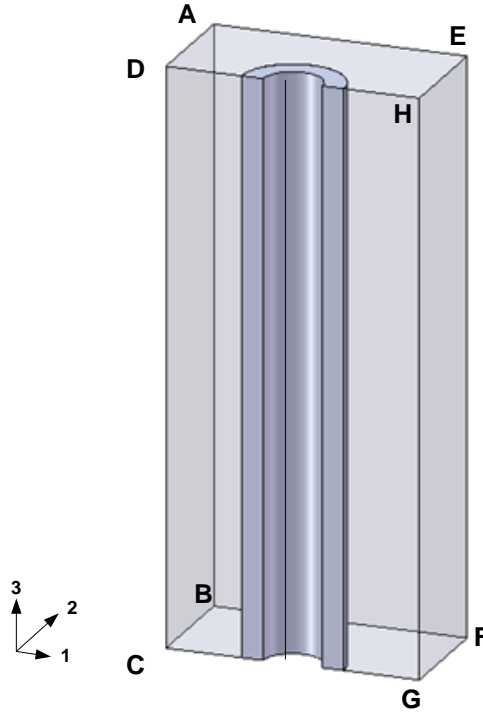


Figure 4.26: The transverse half unit cell model of dentin for shear test analysis

For conducting shearing on the 1-2 plane, firstly, the faces CDGH and ABEF are fixed in direction-3 in a way that the normal displacements of these faces follow the relation below.

$$(u_{33})_{face\ CDGH} = (u_{33})_{face\ ABEF} = 0 \quad (4.15)$$

Secondly, the faces ABCD and EFGH are constrained to movement in directions -1 and -3 in such a way that Equation (4.16) is used for the description of the normal displacements of these faces.

$$(u_{11})_{face\ ABCD} = (u_{33})_{face\ ABCD} = (u_{11})_{face\ EFGH} = (u_{33})_{face\ EFGH} = 0 \quad (4.16)$$

Thirdly, constraints are set to the faces BCFG and ADEH in order that they remain flat and parallel with each other while shearing is performed.

Concerning the loading condition, displacement u_{22} is added on the face ABCD in direction-2. On the other hand, displacement of the same magnitude is applied on face EFGH but in the opposite direction. These relations can be described as:

$$(u_{22})_{face\ ABCD} = u_{22}, (u_{22})_{face\ EFGH} = -u_{22} \quad (4.17)$$

The shear stress $\bar{\sigma}_{12}$ of the unit cell model in the 1-2 plane is defined as the averaged shear stress in the 1-2 plane on face ABCD, calculated using the formula below:

$$\bar{\sigma}_{12} = \frac{\int_A \sigma_{12} dA}{A} = \frac{\sum_{i=1}^n (\sigma_{12})_i A_i}{A} \quad (4.18)$$

where $(\sigma_{12})_i$ is the stress component in the i th element of face ABCD with area A_i , and n is the total number of elements in face ABCD.

On the other hand, the shear strain of the model ε_{12} is defined as the tangent of the shear angle θ in the 1-2 plane as follows:

$$\varepsilon_{12} = \tan \theta = \frac{(u_{12})_{face\ ABCD}}{l_{initial}} \quad (4.19)$$

Similarly, to conduct shear tests in the 1-3 plane, the boundary and loading conditions are defined as follows:

$$(u_{22})_{face\ CDGH} = (u_{22})_{face\ ABEF} = 0 \quad (4.20)$$

$$(u_{11})_{face\ ABCD} = (u_{22})_{face\ ABCD} = (u_{11})_{face\ EFGH} = (u_{22})_{face\ EFGH} = 0 \quad (4.21)$$

$$(u_{33})_{face\ ABCD} = u_{33}, (u_{33})_{face\ EFGH} = -u_{33} \quad (4.22)$$

In addition, constraints are set to faces BCFG and ADEH in order that they remain flat and parallel with each other while shearing is performed.

The shear stress $\bar{\sigma}_{13}$ and shear strain ε_{13} of the unit cell model in the 1-3 plane are defined using Equations (4.23) and (4.24):

$$\bar{\sigma}_{13} = \frac{\int_A \sigma_{13} dA}{A} = \frac{\sum_{i=1}^n (\sigma_{13})_i A_i}{A} \quad (4.23)$$

$$\varepsilon_{13} = \tan \theta = \frac{(u_{13})_{face\ ABCD}}{l_{initial}} \quad (4.24)$$

4.2.2. Calibration of Mechanical Parameters

To describe the stress-strain relations of enamel and dentin parametrically in bulk, a constitutive law has been employed. Regarding their hierarchical structure, as shown in Figure 4.1, the 1-2 plane is taken as the transverse plane of isotropy. Consequently, the mechanical property description parameters have the relationships as follows:

$$E_T = E_{11} = E_{22} \quad (4.25)$$

$$\nu_{TT} = \nu_{12} = \nu_{21} \quad (4.26)$$

$$\nu_{LT} = \nu_{31} = \nu_{32} \quad (4.27)$$

$$\nu_{TL} = \nu_{13} = \nu_{23} \quad (4.28)$$

where E is the elastic modulus, ν is Poisson's ratio, and the subscripts T and L represent the transverse and longitudinal directions respectively. Following the above relationships, the corresponding stress-strain ($\sigma - \varepsilon$) relations describing the elastic behavior of enamel and dentin can be expressed as:

$$\begin{pmatrix} \varepsilon_{11} \\ \varepsilon_{22} \\ \varepsilon_{33} \\ \varepsilon_{12} \\ \varepsilon_{13} \\ \varepsilon_{23} \end{pmatrix} = \begin{pmatrix} \frac{1}{E_T} & -\frac{\nu_{TT}}{E_T} & -\frac{\nu_{LT}}{E_L} & 0 & 0 & 0 \\ -\frac{\nu_{TT}}{E_T} & \frac{1}{E_T} & -\frac{\nu_{LT}}{E_L} & 0 & 0 & 0 \\ -\frac{\nu_{TL}}{E_T} & -\frac{\nu_{TL}}{E_T} & \frac{1}{E_L} & 0 & 0 & 0 \\ 0 & 0 & 0 & \frac{1}{G_{TT}} & 0 & 0 \\ 0 & 0 & 0 & 0 & \frac{1}{G_{TL}} & 0 \\ 0 & 0 & 0 & 0 & 0 & \frac{1}{G_{TL}} \end{pmatrix} \begin{pmatrix} \sigma_{11} \\ \sigma_{22} \\ \sigma_{33} \\ \sigma_{12} \\ \sigma_{13} \\ \sigma_{23} \end{pmatrix} \quad (4.29)$$

In general, the quantities ν_{LT} and ν_{TL} are not equal and are related by equation (4.30).

The in-plane (1-2) shear modulus can be expressed using equation (4.31).

$$\frac{\nu_{TL}}{E_T} = \frac{\nu_{LT}}{E_L} \quad (4.30)$$

$$G_{TT} = \frac{E_T}{2(1+\nu_{TT})} \quad (4.31)$$

Regarding the plastic yielding of an anisotropic body, Hill's potential function (1948) has been used for the calculation of the effective yield stress (equation (4.32)).

$$f = \sqrt{A(\sigma_{11} - \sigma_{22})^2 + B(\sigma_{22} - \sigma_{33})^2 + B(\sigma_{33} - \sigma_{11})^2 + 2C\sigma_{12}^2 + 2D\sigma_{13}^2 + 2D\sigma_{23}^2} \quad (4.32)$$

where A to D are the dimensionless parameters and are defined as:

$$A = \frac{\sigma_0^2}{\sigma_{0T}^2} - \frac{\sigma_0^2}{2\sigma_{0L}^2}, B = \frac{\sigma_0^2}{2\sigma_{0L}^2}, C = \frac{\sigma_0^2}{2\sigma_{0TT}^2}, D = \frac{\sigma_0^2}{2\sigma_{0TL}^2} \quad (4.33)$$

where σ_0 , σ_{0T} , σ_{0L} , σ_{0TT} , and σ_{0TL} are the reference yield stress, yield stress along the transverse, longitudinal, in-plane shear, and out-of-plane shear directions respectively. Such function has also been adjusted to define the yield criterion as stated in equation (4.34):

$$f - \sigma_0 \geq 0 \quad (4.34)$$

For the post yielding behavior, the associated flow rule is:

$$\boldsymbol{\varepsilon}^p = \bar{\lambda} \frac{\partial f}{\partial \boldsymbol{\sigma}} = \frac{\bar{\lambda}}{f} \mathbf{b} \quad (4.35)$$

where $\bar{\lambda}$ is the plastic multiplier and \mathbf{b} is defined as:

$$\mathbf{b} = \begin{pmatrix} -B(\sigma_{33} - \sigma_{11}) + A(\sigma_{11} - \sigma_{22}) \\ B(\sigma_{22} - \sigma_{33}) - A(\sigma_{11} - \sigma_{22}) \\ -B(\sigma_{22} - \sigma_{33}) + B(\sigma_{33} - \sigma_{11}) \\ 2C\sigma_{12} \\ 2D\sigma_{13} \\ 2D\sigma_{23} \end{pmatrix} \quad (4.36)$$

To describe the stress-strain relations of either enamel or dentin in bulk using the constitutive law, definitions of twelve parameters are required, i.e. seven for elasticity (E_T , E_L , ν_{TT} , ν_{TL} , ν_{LT} , G_{TT} , G_{TL}) and five for plasticity (σ_{0T} , σ_{0L} , σ_{0TL} , σ_{0TT} and $\bar{\lambda}$).

Before the calculation of the seven elastic parameters, some manipulations of the equations are needed. Recalling equation 4.29, the strain component ε_{33} obtained when tensile loadings were applied on the 1-2 plane along the 3-direction can be written as

$$\varepsilon_{33} = -\frac{v_{TL}\bar{\sigma}_{11}}{E_T} - \frac{v_{TL}\bar{\sigma}_{22}}{E_T} + \frac{\bar{\sigma}_{33}}{E_L} \quad (4.37)$$

Transforming equation (4.30), gives

$$v_{TL} = \frac{E_T v_{LT}}{E_L} \quad (4.38)$$

Substituting (4.38) into (4.37), gives

$$\varepsilon_{33} = g(E_L, v_{LT}) = -\frac{v_{LT}\bar{\sigma}_{11}}{E_L} - \frac{v_{LT}\bar{\sigma}_{22}}{E_L} + \frac{\bar{\sigma}_{33}}{E_L} \quad (4.39)$$

Using equation (4.39), E_L and v_{LT} can be determined as the best-fit parameters through the nonlinear regression method using the data describing the elastic portion of the tensile test. Such method involves an iterative process to minimize the value of merit function $a(E_L, v_{LT})$, giving

$$a(E_L, v_{LT}) = \sum_{i=1}^N \left[\frac{\varepsilon_{33i} - g_i(E_L, v_{LT})}{e_i} \right] \quad (4.40)$$

where e_i is the standard deviation of the i -th data point.

The shear moduli, G_{TT} and G_{TL} , can be determined through equations (4.41) and (4.42) using the simulation results from shear testing where the shearing loading is applied along the direction-1 on the 1-2 plane and 1-3 plane respectively.

$$G_{TT} = \frac{\bar{\sigma}_{12}}{\bar{\varepsilon}_{12}} \quad (4.41)$$

$$G_{TL} = \frac{\bar{\sigma}_{13}}{\bar{\varepsilon}_{13}} \quad (4.42)$$

Transforming equation (4.31), gives

$$v_{TT} = \frac{E_T}{2G_{TT}} - 1 \quad (4.43)$$

Transforming equation (4.30), gives

$$v_{LT} = \frac{E_L v_{TL}}{E_T} \quad (4.44)$$

Through conducting tensile testing along direction-3 on the 1-2 plane, the strain component ε_{22} can be defined as

$$\varepsilon_{22} = -\frac{v_{TT} \bar{\sigma}_{11}}{E_T} + \frac{\bar{\sigma}_{22}}{E_T} - \frac{v_{LT} \bar{\sigma}_{33}}{E_L} \quad (4.45)$$

Substituting (4.43) and (4.44) into (4.45), gives

$$\varepsilon_{22} = h(E_T) = -\frac{\bar{\sigma}_{11}}{2G_{TT}} + \frac{\bar{\sigma}_{11}}{E_T} + \frac{\bar{\sigma}_{22}}{E_T} - \frac{v_{TL} \bar{\sigma}_{33}}{E_T} \quad (4.46)$$

By substituting the known quantities (v_{TL} and G_{TT}) and applying the nonlinear regression method using the data describing the elastic portion of the tensile test, E_T can be determined. The regression method involves the minimization of the value of merit function

$$b(E_T) = \sum_{i=1}^N \left[\frac{\varepsilon_{22i} - h_i(E_T)}{e_i} \right] \quad (4.47)$$

Through substituting the known quantities into equations (4.38) and (4.43), values of v_{TL} and v_{TT} can be determined.

Regarding the plastic parameters, the yield stress along the transverse σ_{0T} , longitudinal σ_{0L} , in-plane shear σ_{0TT} , and out-of-plane shear σ_{0TL} directions were obtained from the stress-strain curves calculated through conducting tensile testing on the 1-2 plane along direction-3, tensile testing on the 1-3 plane along direction-2, shear testing on the 1-2 plane along direction-1, and shear testing on the 1-3 plane along direction-1 respectively. Plastic coefficients A-D could then be calculated accordingly.

The plastic multiplier $\bar{\lambda}$ was estimated through averaging the six plastic multiplier components as shown in equation (4.48). Since the 1-2 plane is the transverse plane of isotropy, the plastic multiplier components have the relationships as stated in (4.49) and (4.50).

$$\bar{\lambda} = \frac{\lambda_{11} + \lambda_{22} + \lambda_{33} + \lambda_{12} + \lambda_{13} + \lambda_{23}}{6} \quad (4.48)$$

$$\lambda_{11} = \lambda_{22} \quad (4.49)$$

$$\lambda_{13} = \lambda_{23} \quad (4.50)$$

Regarding the plastic part of the stress-strain data, strain component ϵ_{33} follows the constitutive law (4.36) as stated in equation (4.51). For the plastic multiplier component λ_{33} , it was determined using the non-linear regression method, equation (4.52), with the post-yielding portion of stress-strain relation data of the tensile test along direction-3 on the 1-2 plane. Similarly, equation (4.53) presents the post-yielding stress-strain relations of ϵ_{22} under tensile testing along direction-2 on the 1-3 plane while (4.54) describes the non-linear regression equation being adopted to calculate λ_{22} .

$$\varepsilon_{33} = m(\lambda_{33}) = \frac{\lambda_{33}}{f} (-B(\bar{\sigma}_{22} - \bar{\sigma}_{33}) + B(\bar{\sigma}_{33} - \bar{\sigma}_{11})) \quad (4.51)$$

$$m(\lambda_{33}) = \sum_{i=1}^N \left[\frac{\varepsilon_{33i} - m_i(\lambda_{33})}{e_i} \right] \quad (4.52)$$

$$\varepsilon_{22} = n(\lambda_{22}) = \frac{\lambda_{22}}{f} (B(\bar{\sigma}_{22} - \bar{\sigma}_{33}) - A(\bar{\sigma}_{11} - \bar{\sigma}_{22})) \quad (4.53)$$

$$n(\lambda_{22}) = \sum_{i=1}^N \left[\frac{\varepsilon_{22i} - n_i(\lambda_{22})}{e_i} \right] \quad (4.54)$$

Equations (4.55) and (4.57) give the post-yielding stress-strain relations of $\bar{\varepsilon}_{12}$ and $\bar{\varepsilon}_{13}$ in the shear test along direction-1 on the 1-2 plane and 1-3 plane respectively. (4.56) and (4.58) describes the non-linear regression equations being adopted to calculate λ_{12} and λ_{13} respectively.

$$\varepsilon_{12} = p(\lambda_{12}) = \frac{\lambda_{12}}{f} (2C\sigma_{12}) \quad (4.55)$$

$$p(\lambda_{12}) = \sum_{i=1}^N \left[\frac{\varepsilon_{12i} - p_i(\lambda_{12})}{e_i} \right] \quad (4.56)$$

$$\varepsilon_{13} = q(\lambda_{13}) = \frac{\lambda_{13}}{f} (2D\sigma_{13}) \quad (4.57)$$

$$q(\lambda_{13}) = \sum_{i=1}^N \left[\frac{\varepsilon_{13i} - q_i(\lambda_{13})}{e_i} \right] \quad (4.58)$$

4.2.3. Results and Discussions

Table 4.3 lists the elastoplastic transverse isotropic parameters of enamel and dentin. Regarding the tensile properties, the determined elastic moduli of enamel in the longitudinal and transverse directions are 80.5GPa and 71.6GPa respectively, which fall within the ranges reported from 1961 to 2008 for the experimental observation of enamel (Craig et al., 1961; Roy and Basu, 2008). The determined yield stresses of dentin in the longitudinal and transverse directions are 421MPa and 365MPa respectively which fall within the reported range from 330MPa to ~900MPa (Staines et al., 1981; Ang et al., 2010).

Table 4.3: The determined transverse isotropic parameters of enamel and dentin

Transverse isotropic parameters of enamel		Transverse isotropic parameters of dentin	
E_T	71.6GPa	E_T	12.3GPa
E_L	80.5GPa	E_L	13.8GPa
ν_{TT}	0.34	ν_{TT}	0.23
ν_{TL}	0.28	ν_{TL}	0.28
ν_{LT}	0.32	ν_{LT}	0.32
G_{TT}	26.8GPa	G_{TT}	4.97GPa
G_{TL}	30.3GPa	G_{TL}	5.46GPa
σ_{0T}	365MPa	σ_{0T}	82.3MPa
σ_{0L}	421MPa	σ_{0L}	87.0MPa
σ_{0TT}	92.2MPa	σ_{0TT}	25.2MPa
σ_{0TL}	88.8MPa	σ_{0TL}	36.0MPa
λ	1.27	λ	0.19

The values of the elastic moduli of dentin in the longitudinal and transverse directions are 13.8GPa and 12.3GPa respectively which falls within the range reported from 1952 to 2011 for the experimental observation of dentin (Peyton et al., 1952; Ziskind et al., 2011). The determined yield stresses of dentin in the longitudinal and transversely directions are 87MPa and 82MPa respectively which fall within the reported range of 75MPa to 159MPa (Nalla et al., 2003; Yan et al., 2008).

Concerning the shear properties, experimental data for both enamel and dentin can rarely be found in the open literature. This is due to the difficulties in conducting conventional shearing test on specimens of small volumes. Using the proposed finite element unit cell modeling method, the anisotropic elastoplastic stress-strain relations of shearing can be predicted numerically. This can facilitate further research in the dental field with a much more accurate result.

Chapter 5. Failure Prediction of Dental Restoration Using a CT-based Finite Element Tooth Model

The purpose of this chapter is to develop a computational approach for failure prediction of dental restoration, so that experimental effort can be minimized. The first objective is to develop a 3D assembly FE model for a restored tooth and its corresponding mandible based on CT images. The second objective is to conduct stress analysis and failure prediction of a dental restoration using the established 3D assembly FE model, where the restoration material is modeled using the determined stress-strain relation, with consideration of internal damage; enamel and dentin are modeled with anisotropic behavior, considering the radial variation structure and using the determined anisotropic mechanical properties.

To create 3D models for a restored tooth with a mandible, a method is proposed to process 2D scanned images of anatomical tissues into 3D FE models through the sequential operations of several software packages, as shown in Figure 5.1. An assembly model, comprising of a tooth and a mandible sub-models, has been constructed. The tooth sub-model is a triphasic one, consisting of enamel, dentin, and pulp phases, and has been incorporated with a Class II mesio-occlusal (MO) restoration structure using CAD software package.

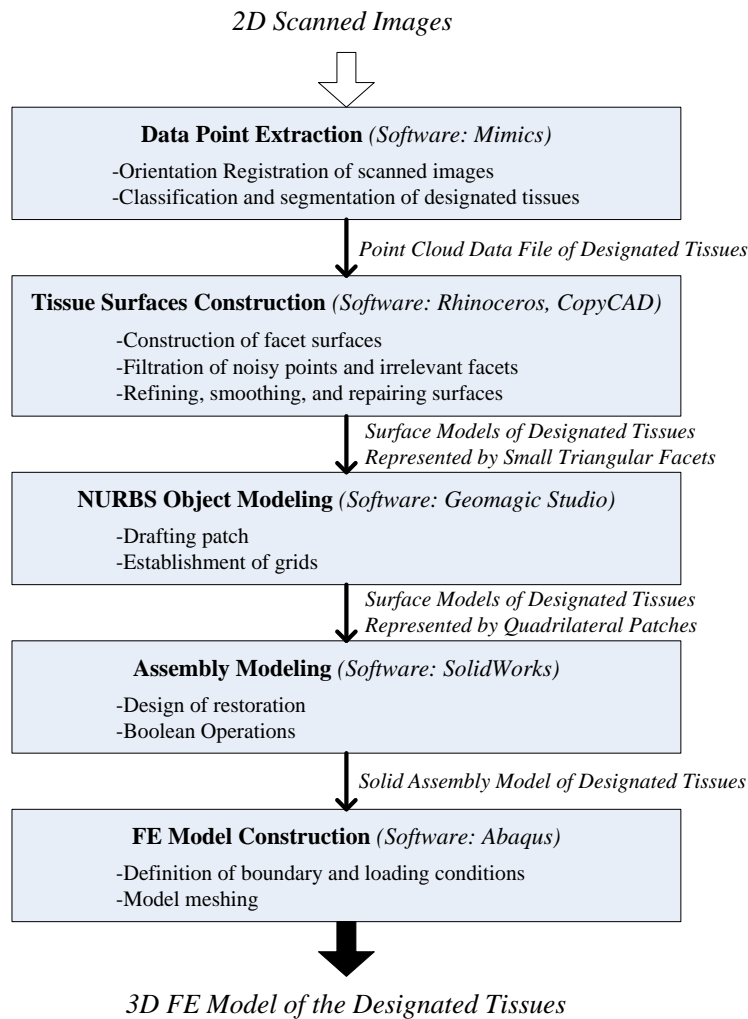


Figure 5.1: The five-stage method in generating a 3D CT-based FE model from 2D scanned images

Concerning the material properties, as shown in Figure 5.2, the elastoplastic mechanical behavior of a dental composite is investigated through resembling the FE results at the macro-scale and micro-scale by damage coupling using a unit cell model, as described in Chapter 3. On the other hand, enamel and dentin are regarded as anisotropic elastoplastic

behaved materials. Their corresponding stress-strain relations are based on the findings in Chapter 4, which are determined using the hierarchical unit cell modeling approach. The length scale of the macro- composite structure/micro- unit cell model is about 1000/1 and satisfies the size requirements of the representative volume element (RVE) of a heterogeneous material/structure (Lemaitre, 1992). The failure damage of the restoration is considered to be a result of the debonding damage in the interphase between the tooth and the restoration material due to an external load.

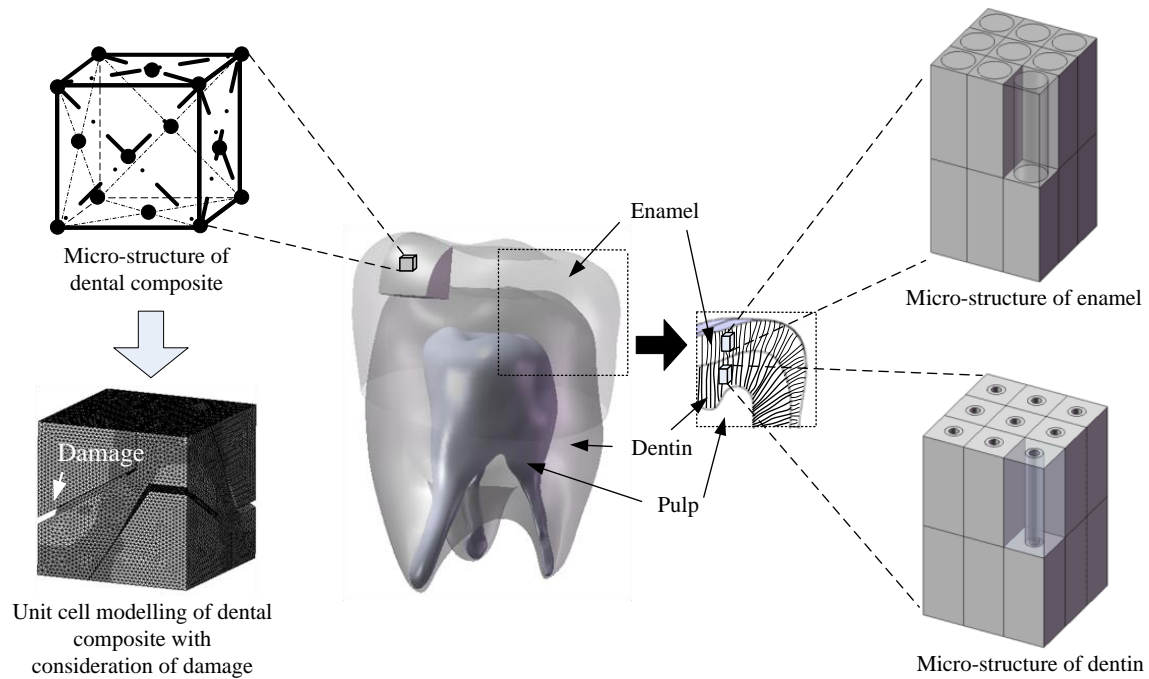


Figure 5.2: Schematic illustration of the proposed approach in creating a more accurate model of a Class II MO restored molar with consideration of materials' micro-structure in defining properties

On application of the FE software (Abaqus 6.8-1) to the heterogeneous mechanistic descriptions of the constitutive behavior of the material elements representing the enamel, dentin, pulp, mandible, dental composite and adhesive material, the stress distribution and restoration failure under mastication forces have been predicted.

5.1. CT-based FE Model Construction for a Class II MO Restored Tooth and a Mandible

5.1.1. Data Point Extraction

This stage is to align the discrete 2D scanned images into one 3D coordinate system. In addition, it is aimed at extracting the geometric data of the designated tissues from the processed images and storing them in a point cloud format.

In this study, the primary input is the CT scan images. A CT scanner, Bright Speed ct 99 (GE Medical System), was used to obtain the skull images of a 20 years old male. The voltage used was 120 kV, and the current was 300mA. The slice thickness was 1.250mm, and the pitch ratio was 0.875:1. The scan option was 0.8s, and a total of 180 images were obtained in 60s. The sets of anatomical images acquired from different 2D perspectives (i.e. top, front and side) were stored in the DICOM format. The sliced images in the top view were organized in sequence and some are shown in Figure 5.3.

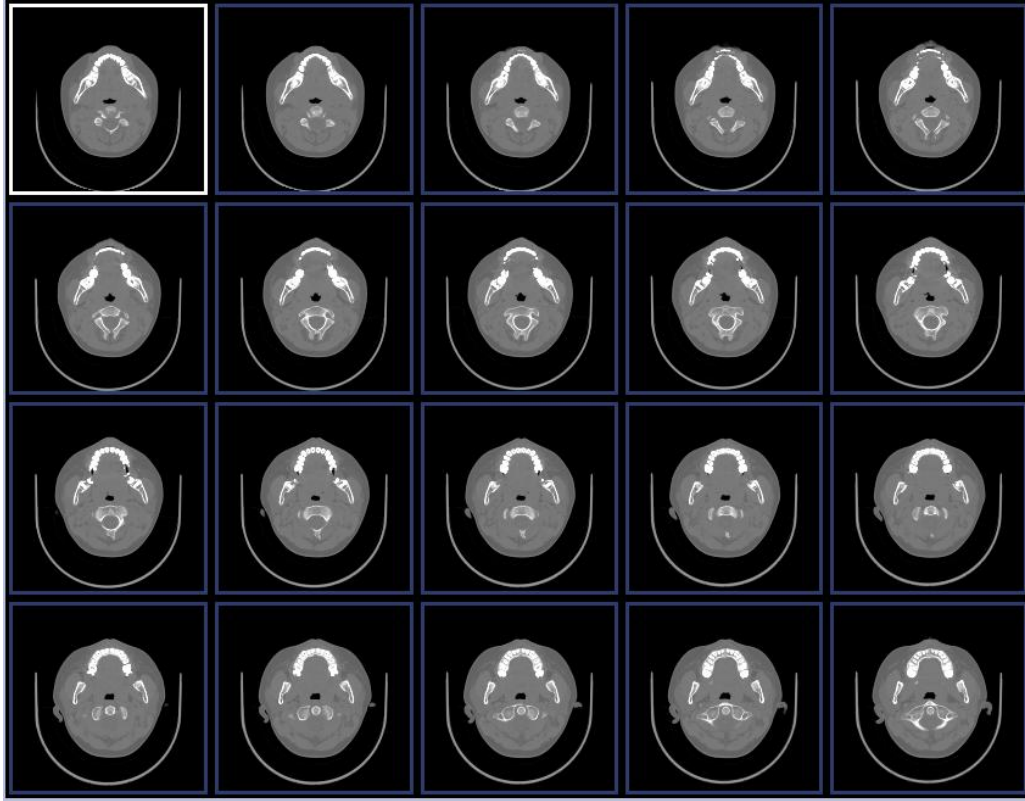


Figure 5.3: Part of the organized CT images in the top view

The organized images are then imported into the software package, Mimics 10.01, to perform the orientation registration process. The process involves the assignment of orientation parameters, top (T), bottom (B), left (L), right (R), anterior (A) and posterior (P), to each anatomical image (Figure 5.4). In addition, the separation distance for each consecutive scanned image was also specified. In this study, the distance was set as 1.25mm.

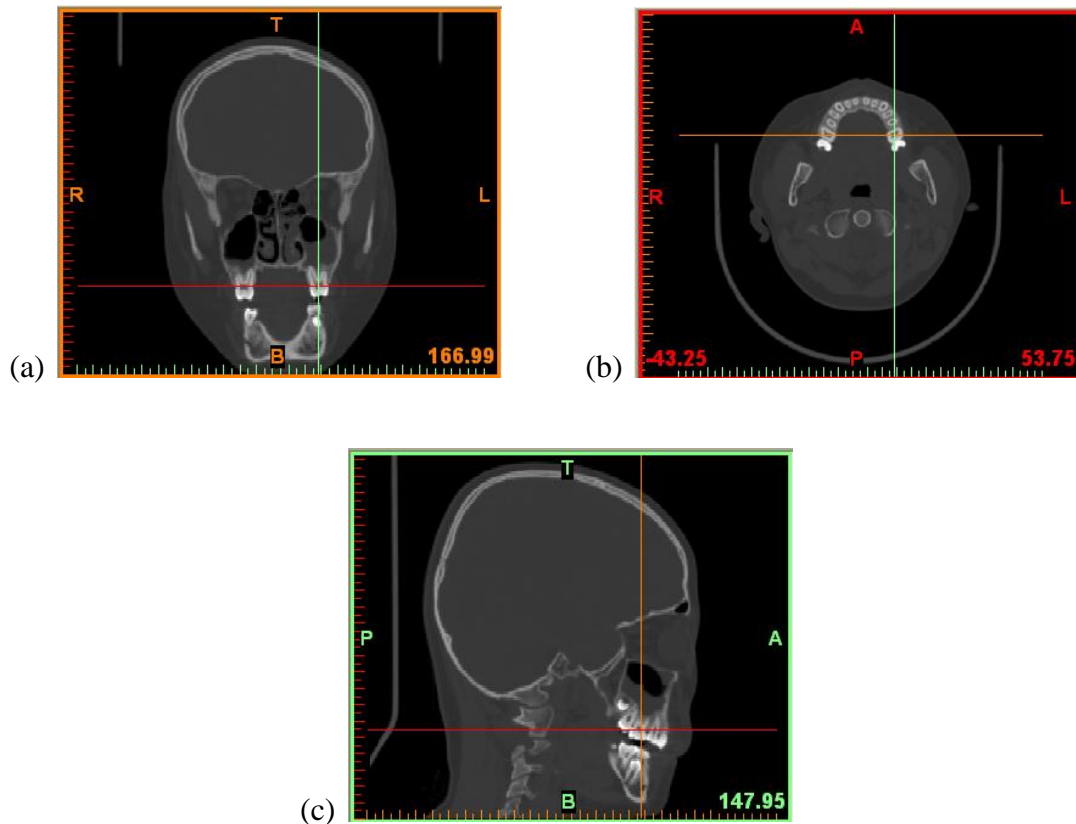


Figure 5.4: Orientation parameters registration, top T, bottom B, left L, right R, anterior A, and posterior P, for (a) front view images; (b) top view images; and (c) side view images

Data on the designated tissues has been extracted through classification and segmentation processes. Each 2D image slice can be regarded as a pixel map of the radiation attenuation tissue coefficient. The level of attenuation can be measured in Hounsfield Units (*HU*). *HU* is a normalized unit whereby water has a value of 0 while air has a value of -1024. The classification process aims at identifying the *HU* value describing the targeted tissue in each scanned image, while segmentation is a process of identifying the *HU* value representing the inner and outer surface boundaries of the tissue. To do so, a

profile line was firstly constructed on a scanned image. The upper and lower limits in terms of the HU values describing the designated tissues were determined from the profile map. Figure 5.5 shows a slice of a scanned image and the corresponding variations of HU along the profile line. Through the classification and segmentation functions of Mimics, the geometric data of the desired anatomical tissue can be preliminary extracted. To extract the geometric data for the mandible, dentin and pulp, an HU value within the range of 176-2176 has been used while 2042-3071 has been defined for enamel. Figure 5.6 presents the preliminarily geometric descriptions, in which the descriptions are transformed and presented in point cloud format.

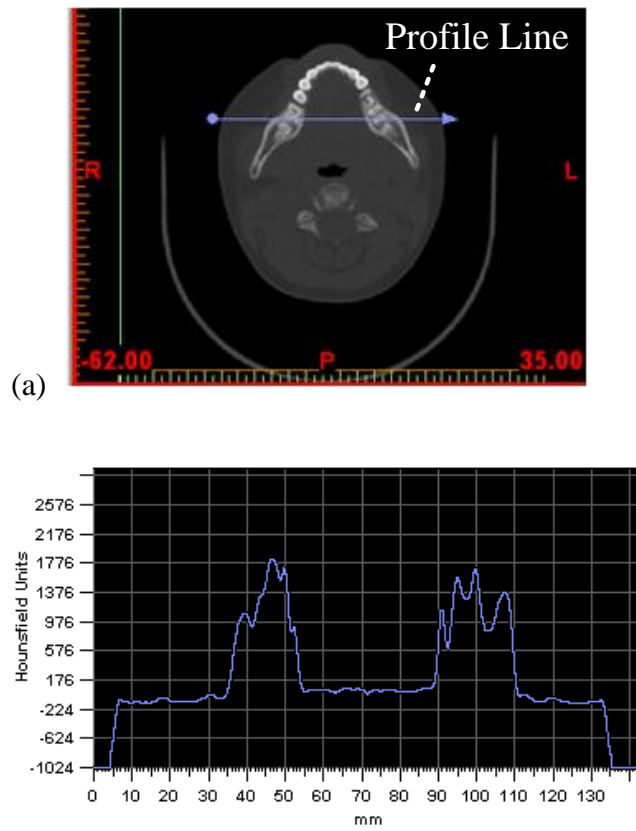


Figure 5.5: (a) A sliced image with a profile line (about the region with teeth and mandible); (b) the corresponding variations of HU value along the profile line

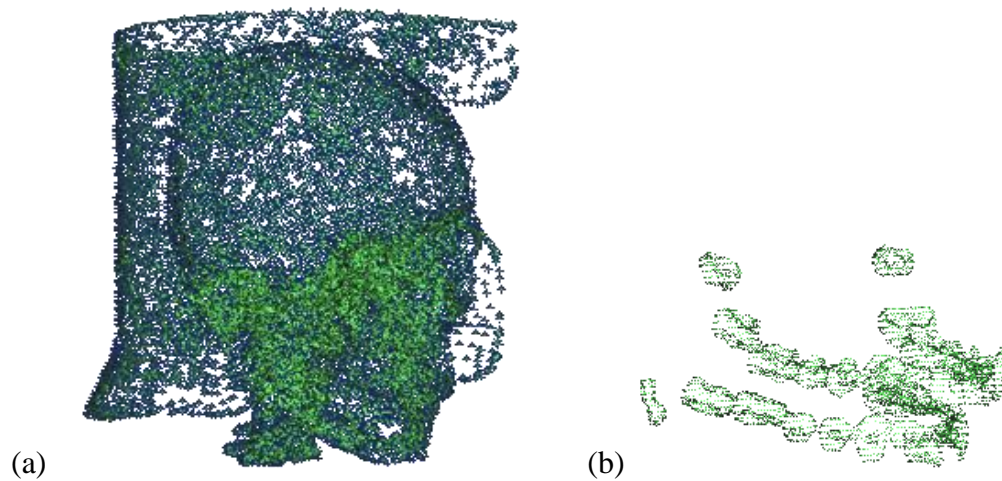


Figure 5.6: The preliminarily obtained geometric point cloud data for (a) mandible, dentin, and pulp descriptions; and (b) enamel description

5.1.2. Tissue Surfaces Construction

The purpose of this stage is to generate surface models of the designated tissues, which are free from imperfections, from the point cloud data through filtration, smoothing, refining, and repairing processes.

At first, the point cloud data acquired from the previous procedure underwent a polygon/facet creation process, and the software package, Rhinoceros ® 3.0, was employed. Facilitated by the software, facets were formed and joined. Surface models were then created as shown in Figure 5.7. Since the classification and segmentation processes (conducted in the previous stage) are performed throughout the whole set of anatomic images, surfaces of non-designated parts having similar *HU* description values

were also generated. In addition, polygon/facet creation was a blind process. Irrelevant facets and noisy points are inevitably formed which could hinder the conversion to the NURBS solid model later on. Therefore, a filtering process was undertaken to erase the non-designated/unwanted parts as well as the noisy points and irrelevant facets.

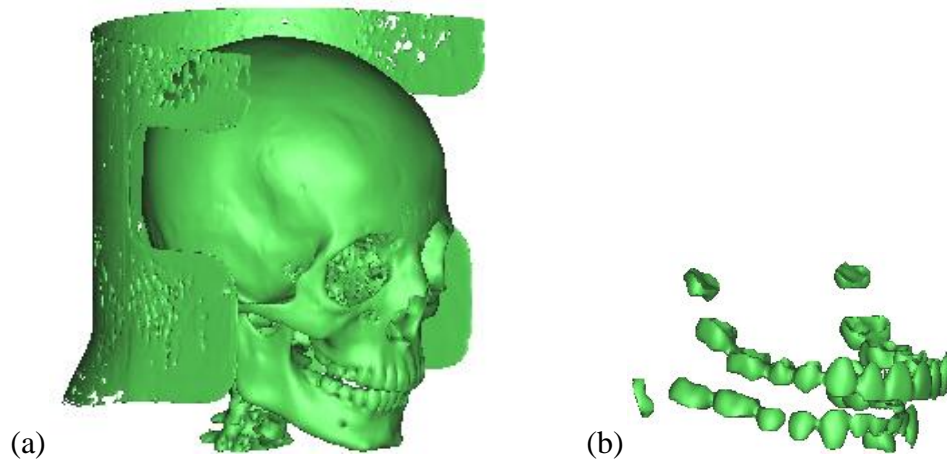


Figure 5.7: The surface models created through the polygon/facet creation process

The filtration process was performed with the aid of the embedded clustering function from Rhinoceros. As demonstrated in Figure 5.8, the surface contour of the mandible was extracted and separated from the noisy points and irrelevant facets. Similarly, the surface contours of enamel, dentin, and pulp were also extracted and filtered.

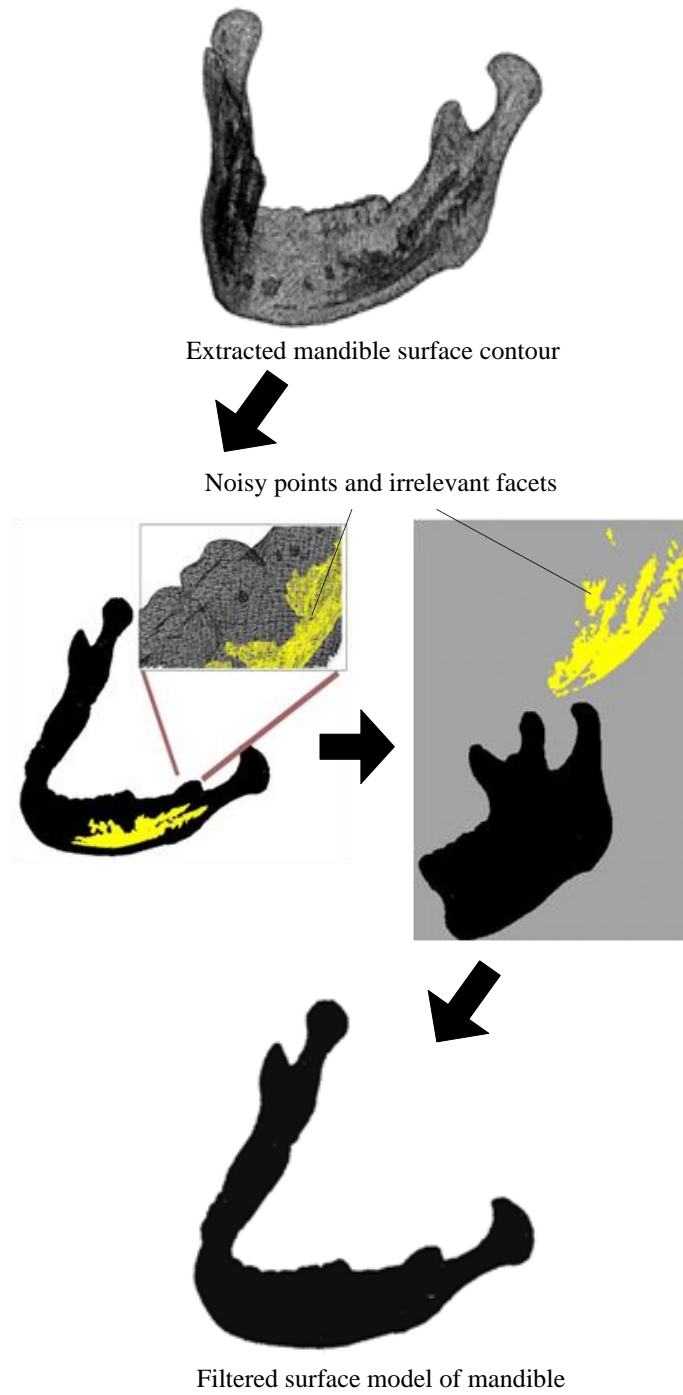


Figure 5.8: An illustrative example of separating noisy point data and irrelevant facets from the designated mandible tissue surface

Surface refinement and smoothing processes were then performed using another software package, CopyCAD. Surface refinement involves the detection and deduction of sharp facet triangles and self-intersecting facet triangles. Such action can minimize the chance of error in creating the mesh model in the later procedure. A surface smoothing process was then carried out, which performs a similar operation through the action of modifications rather than deductions. This process involves the definition of a smooth factor (SF) value (a real number ranging from 0 to 1) and an iterative parameter (IP). The SF value indicates the importance of the local geometry. If the local geometry is important, the value of the SF will be set to a small value, which indicates that the corresponding smoothing action is limited. If a large value of SF (close to 1) is set, the position of the nodes of the facet triangle sets would be rearranged and the newly assigned position is mainly determined by the position of the other points of the facet triangles in the neighborhood. The number of cycles for smoothing depends on the defined IP. The definition of IP needs to be exercised with caution and to avoid exaggeration. If too many cycles of smoothing are performed, the imported 3D object would be turned into a sphere-like object. Suitable iteration cycles can maintain the morphology of the part of interest while reducing computational loading when carrying out simulation analysis. In this study, the SF and IP parameters were given values of 0.1 and 3 respectively.

Surface repairing was also performed in this procedure, dealing with repairing imperfections, such as small holes and big cavities, in the designated surfaces. Such process was carried out through one of the three schemes, shown in Figure 5.9, based on

the selection criteria. This procedure is important in constructing a closed-surface model which is a must condition for the solid model construction process in the later procedure.

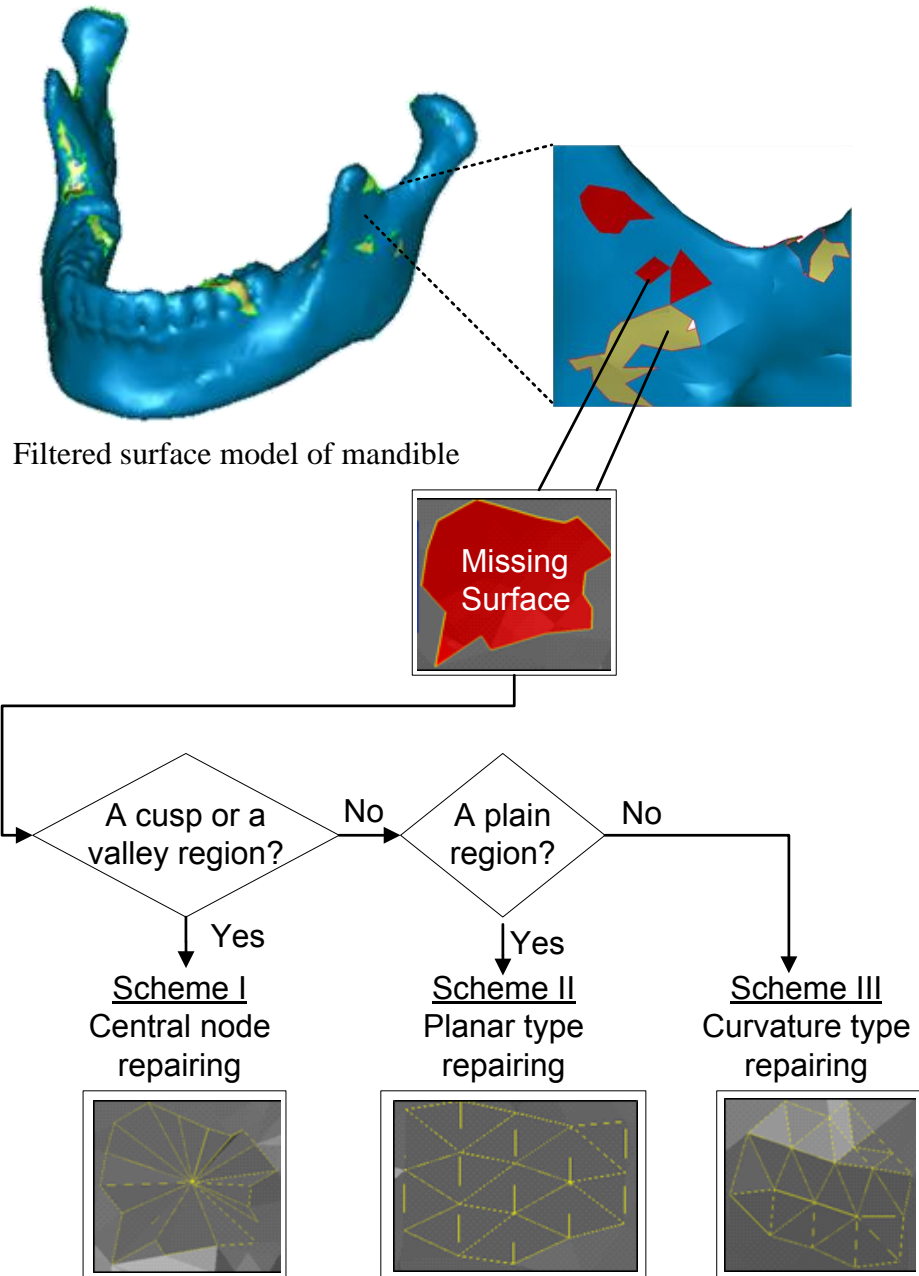


Figure 5.9: Surface repairing process involved in the tissue surface construction stage

5.1.3. NURBS Object Modeling

This procedure aims to represent the facet surfaces of the designated tissues using the non-uniform rational basis spline (NURBS) mathematical model. NURBS representing surfaces allows better performance in designing and creating restorations using CAD tools.

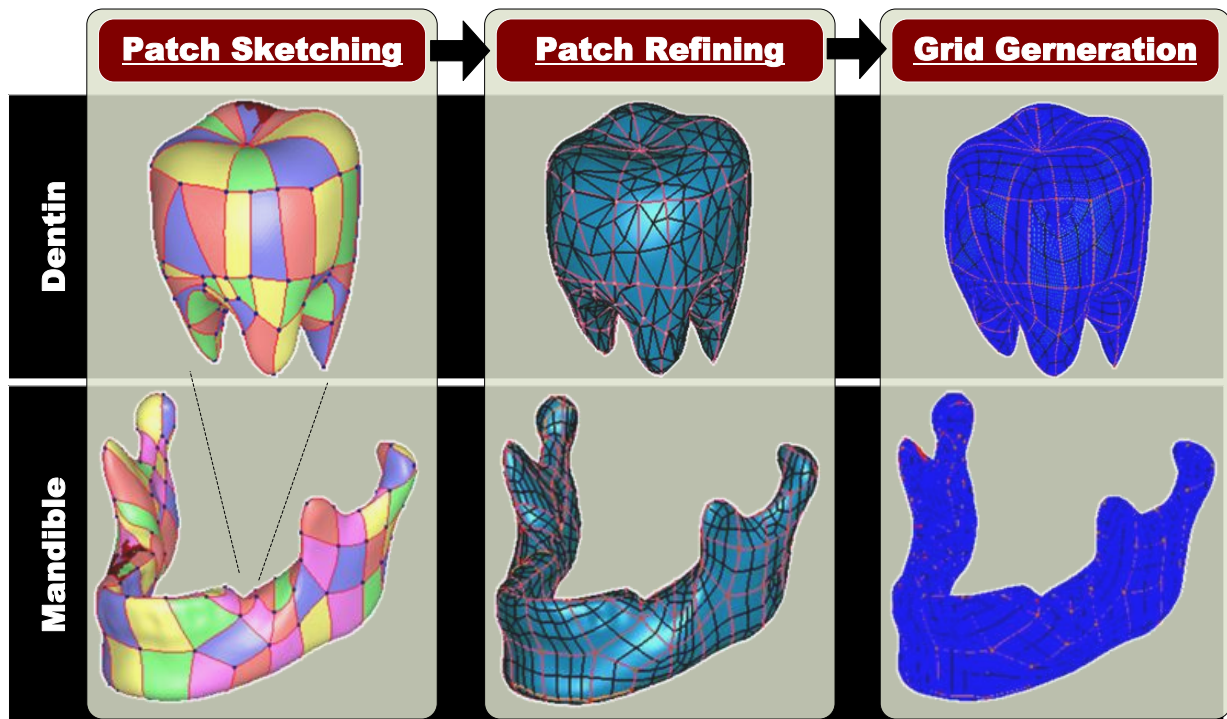


Figure 5.10: Processes involved in the NURBS object modeling procedure

Patch sketching, patch refining and grid generation are the three processes involved in converting the facet surfaces into NURBS representing surfaces. After the three processes, the morphology of the imported surface models can be kept but is represented using quadrilateral patches. Figure 5.10 illustrates the processes involved in creating the

NURBS representing surfaces of dentin and mandible. This was done using the software package, Geomagic Studio 10.

5.1.4. Assembly Modeling

This stage is aimed at transforming the NURBS surface model into a solid model. Using the CAD tools, a conceptual research idea can be substantiated virtually and established interactively according to the freeform geometry of living tissues. In this study, a Class II MO restoration structure has been incorporated virtually into a tooth model.

Firstly, the imported NURBS surface models of the mandible and tooth underwent a geometric diagnosis process using the CAD software package, SolidWorks ® Office Premium 2007. If a model is detected in an opened state, it needs to be reworked from the “Tissue Surfaces Construction” procedure, where the surface repairing process can be performed. If a model is identified to be in a closed state, a solid model can be generated directly.

Facilitated with the CAD tools, Boolean operations were performed for the construction of a restored tooth. Figure 5.11 demonstrates the Boolean subtraction process for creating a restoration cavity on the tooth model. Additionally, the Boolean union process was executed to trim off and customize the Class II MO restoration model according to the geometry of a tooth surface with dimensions given by Yaman et al. (2000) and a 10µm thick adhesive phase (Ausiello et al., 2011). In addition, to simulate the mastication process, a ball-shaped morsel with a diameter of 6mm was constructed to apply occlusal

loading to the tooth model (Lin et al., 2008b). The desired assembly model with a restored tooth and a mandible sub-models was then prepared.

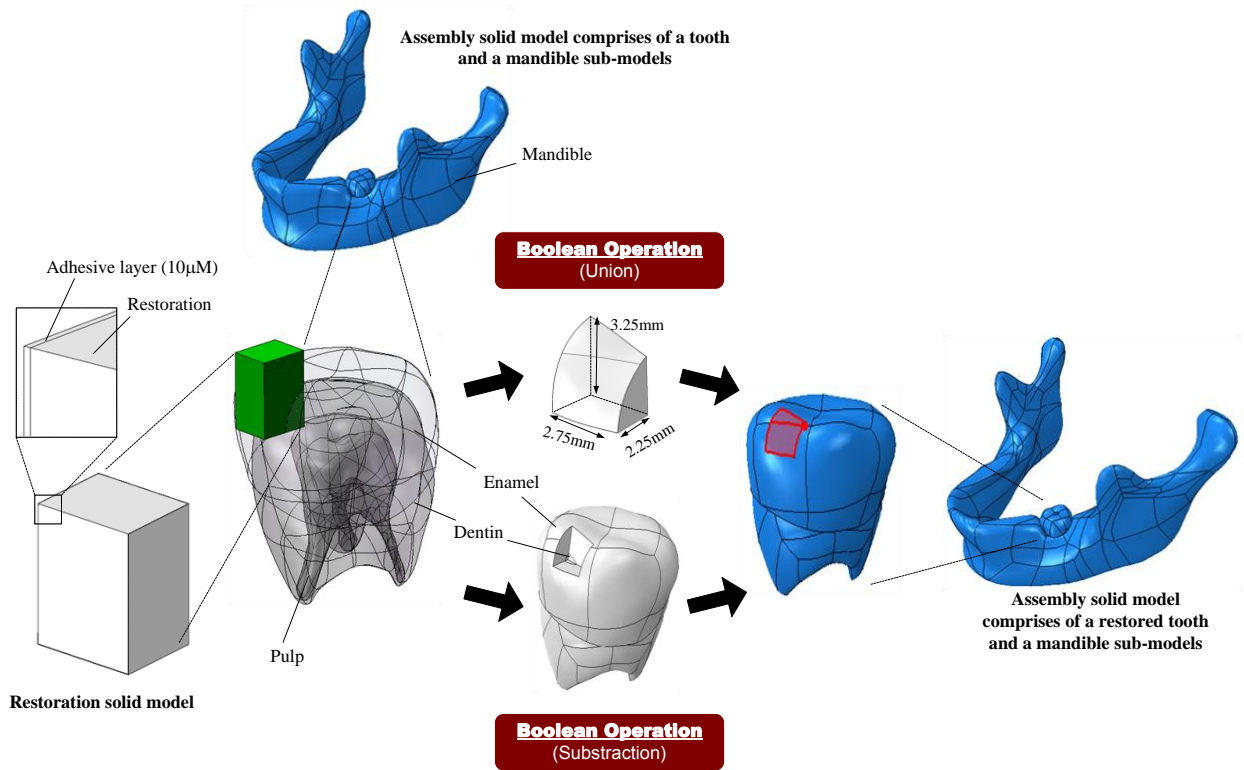


Figure 5.11: Processes involved in the assembly modeling procedure

5.1.5. FE Model Construction

This stage aims to further develop the assembly solid model from the previous stage to a FE model, and involves the definition of the loading and boundary conditions, as well as meshing the model using finite elements.

The assembly model of a mandible with a restored tooth was meshed using 3D tetrahedral solid elements (C3D4). This was done using the CAE software package, Abaqus 6.8-1. Explicit finite element theory has been employed, as discussed in Section 2.8. To simulate the mastication loading, a spherical morsel was used having impact velocity of 0.03 mm s^{-1} exerted on the restoration (Yaman et al., 2000). Simplified boundary conditions were applied, and the base of the mandible model was fixed.

5.2. Material Properties and Mechanical Damage Modeling

In this study, a commercially available compomer SrF₂/UEDMA:TCB:TEGDMA, with particle volume fraction of 47%, was selected as the restoration material (Dentsply, 2011). Its material properties were set according to the stress-strain relations in Chapter 3 considering interfacial debonding damage, Figure 3.23. To simulate marginal damage, an interphase of thickness 10 μm was added between the restoration and the tooth structure (Ausiello et al., 2011). The mechanical properties of the interphase were assumed to be the same as the restoration material except that it was considered to be damageable. To simulate the debonding damage, a stress-based failure criteria was adopted for the interfacial elements. When the $\bar{\sigma}_H$ stress of an element reached a critical value σ_c , damage was assumed to occur. In this study, σ_c was set with the bond strength of the dental composite to the enamel (Munehika et al., 1984). The vanishing finite element technique (Li et al., 2000) was employed to simulate the debonding damage of the restoration phase in the FE models.

Concerning the properties of enamel and dentin, their anisotropic elastoplastic properties were assigned using the determined mechanical parameters as listed in Table 4.3. To take into account the radial variation structure of enamel and dentin, the tooth model was partitioned into 18 regions, with a specific local coordinate system for each, as shown in Figure 5.12. The material properties for the morsel, mandible, and pulp phases of the model were assigned as stated in Table 5.1.

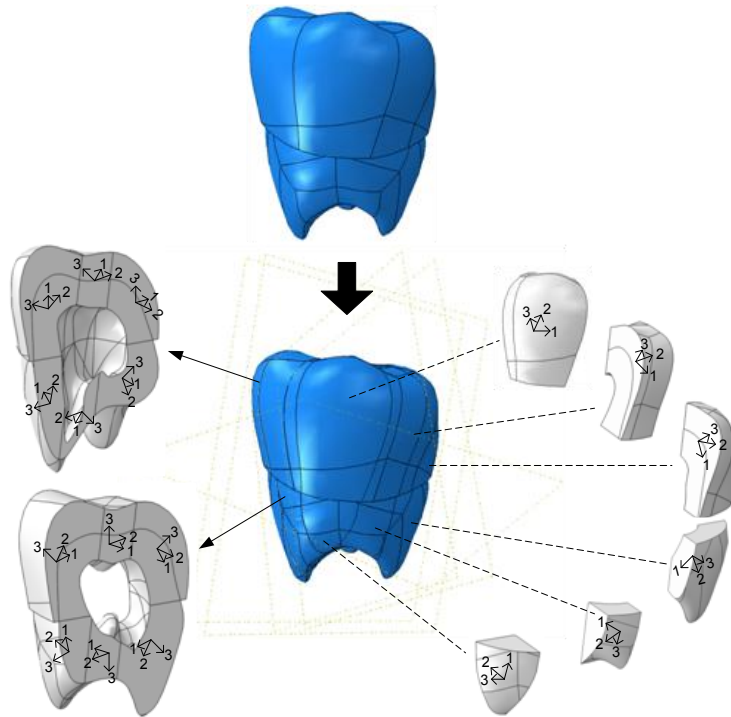


Figure 5.12: The 18 partitioned regions of the tooth model with their associated local coordinate system

Table 5.1: Mechanical properties of morsel, mandible, and pulp phases

	Elastic modulus (GPa)	Poisson's ratio
Morsel ^a	210	0.3
Mandible ^b	14.7	0.3
Pulp ^b	2	0.45

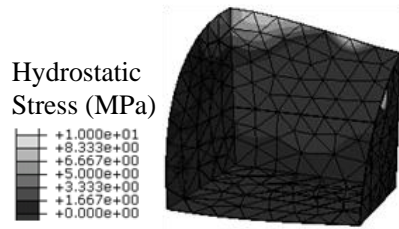
a: (Li et al., 2011); b: (Gurbuz et al., 2008)

5.3. Stress Distribution and Failure Prediction of Restoration

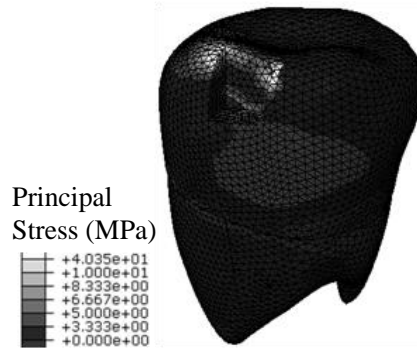
Figure 5.13 presents the failure initiation and propagation of the restoration and shows the stress distribution in the interphase and tooth phase. Budyn and Hoc (2007) stated that damage cracks of bone tissue can be initiated perpendicularly to the maximum principal stress direction, so the tooth phase was studied using the maximum principal stress. Under small loading, the interphase is in an intact state since none of the elements exceeded the hydrostatic critical value σ_c . In such a state, in both the interphase and tooth phase, it is found that most of the loading was sustained in the marginal region near to the loading. When further loading was applied, part (i) of the figure shows where damage was initiated, and values of $\bar{\sigma}_H$ of the interfacial elements exceeding σ_c were removed from the mesh. Interfacial elements in the marginal region were firstly removed and the debonding damage was propagated progressively downwards. Concerning the stress distribution, stresses were concentrated around the debonded tips in the interphase. In addition, the tooth phase above the debonded region sustained less stress in comparison with the bonded region. Based on the simulation result, the interfacial debonding

occurred once the mastication loading reached 140N. This is in a good agreement with experimental studies (Yaman et al., 2000; Li et al., 2010).

(a) Load=47N

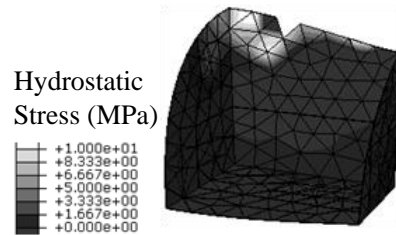


(i) Interphase

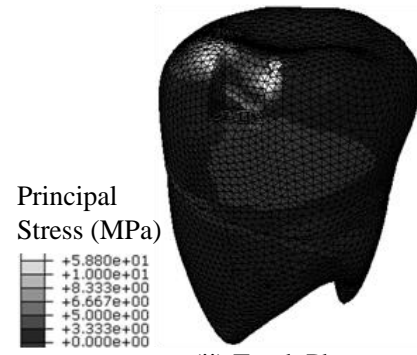


(ii) Tooth Phase

(b) Load=140N

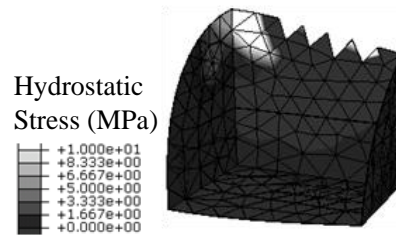


(i) Interphase

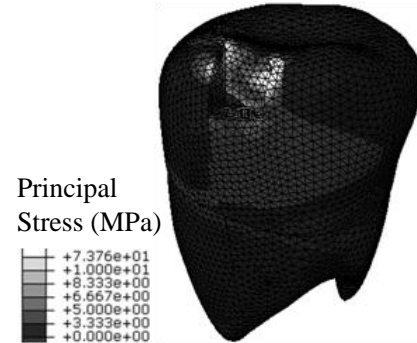


(ii) Tooth Phase

(c) Load=152N

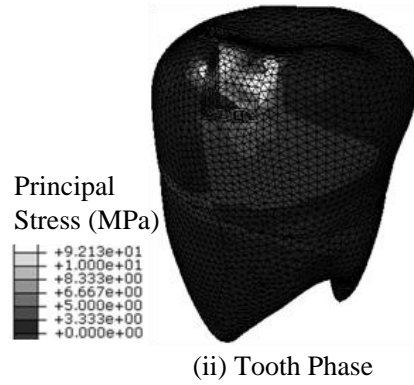
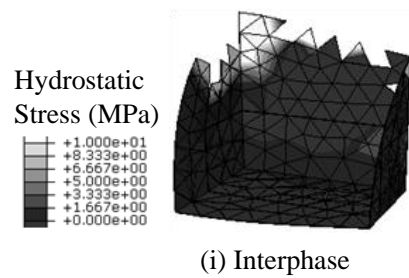


(i) Interphase

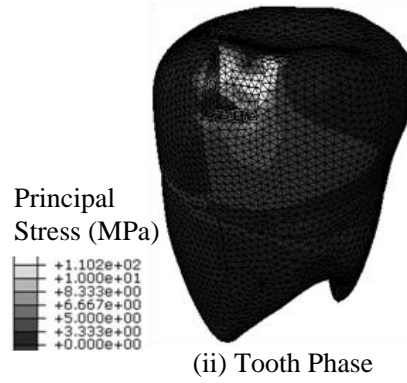
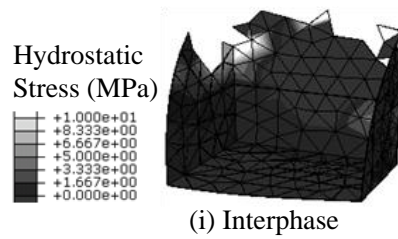


(ii) Tooth Phase

(d) Load=177N



(e) Load=258N



(f) Load=299N

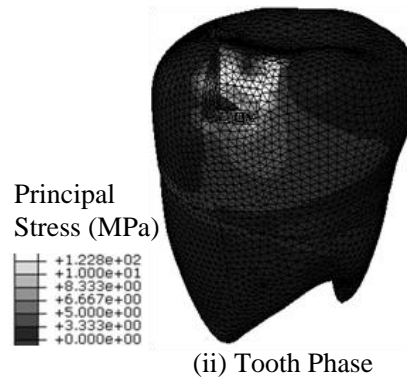
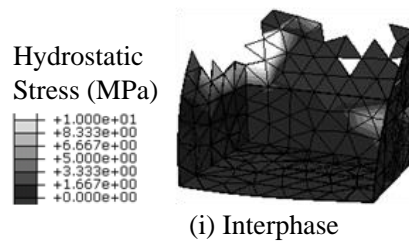


Figure 5.13: Predicted stress distribution in the interphase and tooth phase at various loads: (a) 47N, (b) 140N, (c) 152N, (d) 177N, (e) 258N, and (f) 299N

Chapter 6. Conclusions and Future Work

6.1. Conclusions and Statement of Originality

In this study, a computational approach has been developed for failure prediction of dental restoration so that experimental effort can be minimized. A scientific method which can facilitate the development of new dental composites considering damage phenomenon has been proposed. The anisotropic elastoplastic mechanical parameters of enamel and dentin in bulk have been determined as well as the isotropic elastoplastic stress-strain relations of their constituents in the micro-scale. The major contributions of this research are summarized below:

- (1) The effect of particle morphology, particle volume fraction, and interfacial strength on the mechanical behavior of dental composites has been investigated using the unit cell modeling method. The CAD-based modeling technique has been suggested through which the construction of a cell model involving various particle morphologies and packing with high packing efficiency, such as body-centered cubic (BCC) and face-centered cubic (FCC) systems, becomes possible. With the integration of inter-part parametric assembly features, unit cell models with different particle volume fractions can be efficiently generated for analysis using the FE technique through simple modification of a predefined key dimension in the template model. With the incorporation of damage in the interphase, the mechanical properties of composites, such as stress concentration, stress distribution, damage

mechanism, elastic modulus, tensile strength, and stress-strain relations, can be studied. The proposed CAD-based method not only assists in the design of composites for the dental industry, but is also applicable to design composites in other applications.

- (2) The elastoplastic properties of the four micro-scale constituents of enamel and dentin have been determined. This was done through the integration of nanoindentation, finite element modeling and artificial neural network techniques. A nanoindentation experiment is firstly performed, and the elastic moduli of the constituents are calculated using the Oliver and Pharr method. The artificial neural network modeling technique has been employed for the functional approximation between the nanoindentation load-displacement responses and the elastoplastic mechanical properties. Four neural networks have been built, and the data obtained from the finite element analyses have been utilized for network training and validating. Based on the neural models, the desired mechanical properties of the four tooth constituents have been determined. Contribution of such a method can benefit the application in determining the elastoplastic mechanical properties of isotropic materials involving small volumes.
- (3) A fixture has been designed and incorporated with the current nanoindentation apparatus, offering rotational movement freedom to conduct nanoindentation experiments on specimens. Thus, indentation on a specimen involving a curved surface can be facilitated, and multi-indentations can also be performed on a single specimen. Contribution of this work can be applied to other applications which involve indentations on curved surfaces.

- (4) The anisotropic elastoplastic properties of enamel and dentin have been determined using a hierarchical unit cell method. By considering the tooth hierarchical structure from the open literature, unit cell models have been constructed for enamel and dentin with the incorporation of the determined elastoplastic properties of the four micro-scale constituents. The desired anisotropic elastoplastic mechanical parameters of enamel and dentin have been calibrated by applying tensile and shear deformations to the unit cell models. A similar idea can be applied to determine the properties of other natural materials such as wood.
- (5) a viable alternative method involving the application of commonly used software packages has been used to create a 3D FE solid assembly model based on 2D CT images. A Class II MO restoration has been incorporated virtually into the tooth model. The contribution of the established method of constructing a 3D FE model from 2D scanned images is not limited to the dental industry but also to other medical applications. It can be applied in creating patient-specific models of any body tissue parts using CT images.
- (6) A 3D tooth FE model with better prediction capability has been constructed. This is due to better definitions of the boundary conditions and material properties. The 3D FE model of the periodontal tissues, i.e. mandible, has also been constructed. Such model gives information on how a tooth is oriented in the patient. Consequently, the definition of the boundary conditions of the tooth model can be established. For the definition of material properties, the determined anisotropic elastoplastic mechanical properties of enamel and dentin have been incorporated into the tooth model. Concerning the radial variation structure of enamel and dentin, the tooth

model has been partitioned into 18 regions, with a specific local coordinate system for each region. Contribution of the tooth model developed is not limited to only this study but also can apply to other research studies where a tooth model is required.

Some of the above mentioned research contributions have led to the following technical papers:

- Y.P. Chan, C.Y. Tang , B.W. Darvell and C.P. Tsui, (2006). “Effect of Filler Shape and Volume Fraction on Strain Damage of Particulate-reinforced Dental Composites”, *Material Science Forum*, 532-533, pp. 117-120.
- Y.P. Chan, C.Y. Tang and C.L. Chow (2006). “CAD-based finite element analysis of dental composites using a face-centred cubic model”, *Industrial Engineering Research*, 3, pp. 111-119.
- Y.P. Chan and C.Y. Tang (2007). “Investigation of Interfacial Debonding Damage and Mechanical Behavior of Dental Composite with Different Filler Geometries”, *Eurofillers 2007*, August 2007, Zalakaros, Hungary, pp. 115.
- Y.P. Chan, C.Y. Tang and C.P. Tsui (2011). “Effect of Debonding Damage on the Mechanical Properties of a Particulate Reinforced Dental Composite”, The Nineteenth Annual International Conference on Composites/ Nano Engineering (ICCE-19), July 2011, Shanghai, China.
- Y.P. Chan, “A Study on Debonding Damage of a Dental Composite with High Particle Loading”, *World Journal of Engineering* (accepted in 2011).

- Y.P. Chan, C.Y. Tang and B. Gao. “Stress Analysis of a Class II MO Restored Tooth Using a 3D CT-based Finite Element Model”, *International Journal of Biomaterials* (accepted in 2012).

6.2. Future Work

In this work, a unit cell model has been adopted to study the mechanical behavior of particulate reinforced dental composites. The reinforcing particles are assumed to be evenly distributed in the matrix so that they are packed regularly and symmetrically in a cubic array. In reality, the distribution of the reinforcing particles is irregular in the matrix. Therefore, further investigation can be focused on developing unit cell models consisting of multiple particles with random distribution. Moreover, advanced digital imaging technology has opened up new alternative possibilities, realistic micro-architecture of a composite material can be digitized and thus an enhanced unit cell model can be constructed for more accurate stress analysis and failure prediction.

The proposed CT-based modeling technique is versatile, using which further research in dentistry, such as design of graded dental implants, can be conducted. For the CT-based tooth model, current model has been partitioned in 18 regions to take into account of the radial variation structure of enamel and dentin. For further improvement, user-defined material subroutines (VUMATs), describing the spatial variance of their material properties, can be written to describe the anisotropic mechanical behavior of enamel and dentin.

References

- Abaqus, 2008. *Abaqus analysis user's manual (version 6.8)*. Providence: Dassault Systèmes Simulia Corp.
- Ang, S.F., Scholz, T., Klocke, A., Schneider, G.A., 2009. Determination of the elastic/plastic transition of human enamel by nanoindentation. *Dental Materials*, 25(11), pp. 1403-1410.
- Ang, S.F., Bortel, E.L., Swain, M.V., Klocke, A., Schneider, G.A., 2010. Size-dependent elastic/inelastic behavior of enamel over millimeter and nanometer length scales. *Biomaterials*, 31(7), pp. 1955-1963.
- Arola, D., Reprogl, R.K., 2005. Effects of aging on the mechanical behavior of human dentin. *Biomaterials*, 26(18), pp. 4051-4061.
- Ashby, M.F., Jones, D.R., 1980. *Engineering Materials*. Oxford, England: Pergamon Press.
- Asmussen, E., Peutzfeldt, A., 1998. Influence of UEDMA BisGMA and TEGDMA on selected mechanical properties of experimental resin composites. *Dental Materials*, 14(1), pp. 51-56.
- Ausiello, P., Apicella, A., Davidson, C.L., 2002. Effect of adhesive layer properties on stress distribution in composite restorations—a 3D finite element analysis. *Dental Materials*, 18(4), pp.295–303.

- Ausiello, P., Franciosa, P., Martorelli, M., Watts, D.C., 2011. Numerical fatigue 3D-FE modeling of indirect composite-restored posterior teeth. *Dental Materials*, 27(5), pp. 423-430.
- Balać, I., Uskoković, P.S., Ignjatović, N., Aleksić, R., Uskoković, D., 2001. Stress analysis in hydroxyapatite/poly-L-Lactide composite biomaterials. *Computational Materials Science*, 20, pp. 275-283.
- Balać, I., Tang, C.Y., Tsui, C.P., Chen, D.Z., Uskoković, P.S., Ignjatović, N., Uskoković, D.P., 2006. Nanoindentation of in situ polymers in hydroxyapatite/poly-L-lactide biocomposites. *Recent developments in advanced materials and processes*, 518, pp.501-506.
- Bao, G., Hutchinson, J.W., McMeeking, R.M., 1991. Particle reinforcement of ductile matrices against plastic flow and creep. *Acta Metallurgica et Materialia*, 39(8), pp. 1871-1882.
- Baran, G., Boberick, K., McCool, J., 2001. Fatigue of restorative materials. *Critical Reviews in Oral Biology & Medicine*, 12, pp.350–360.
- Bastioli, C., Romano, G., Migliaresi, C., 1990. Water sorption and mechanical properties of dental composites. *Biomaterial*, 11, pp.219–223.
- Bechtle, S., Ang, S.F., Schneider, G.A., 2010. On the mechanical properties of hierarchically structured biological materials. *Biomaterials*, 31(25), pp. 6378-6385.

- Bowen, R.L., Rodriguez, M.M., 1962. Tensile strength and modulus of elasticity of tooth structure and several restorative materials. *Journal of the American Dental Association*, 64, pp. 378-387.
- Boyd, S. K., Davison, P., Müller, R., Gasser, J. A., 2006. Monitoring individual morphological changes over time in ovariectomized rats by in vivo micro-computed tomography. *Bone*, 39(4), pp. 854-862.
- Brodnyan, J.G., 1959. The concentration dependence of the Newtonian viscosity of prolate ellipsoids. *Journal of Rheology*, 3, pp.61–68.
- Bucaille, J.L., Stauss, S., Felder, E., Michler, J., 2003. Determination of plastic properties of metals by instrumented indentation using different sharp indenters. *Acta Materialia*, 51(6), pp. 1663-1678.
- Budyn, E., Hoc, T., 2007. Multiple scale modeling for cortical bone fracture in tension using X-FEM. *Revue Européenne de Mécanique Numérique*, 16, pp. 215-238.
- Bujtár, P., Sándor, G.K.B., Bojtos, A., Szucs, A., Barabás, J., 2010. Finite element analysis of the human mandible at 3 different stages of life. *Oral Surgery, Oral Medicine, Oral Pathology, Oral Radiology, and Endodontology*, 110(3), pp. 301-309.
- Bulychev, S. I., Alekhin, V. P., Shorshorov, M. Kh., Ternovskii, A. P., 1976. Mechanical properties of materials studied from kinetic diagrams of load versus depth of impression during microimpression. *Strength Mater*, 8, pp. 1084–1089.

- Bulychev, S.I., Alekhin, V.P., Shorshorov, M.K., Ternovskii, A.P., Shnyrev, G.D., 1975. Determining Young's modulus from the indenter penetration diagram. *Zavodskaya Laboratoriya*, 41(9), pp. 1137-1140.
- Bush, M.B., 1992. An investigation of two- and three-dimensional models for predicting the elastic properties of particulate- and whisker-reinforced composite materials. *Materials Science and Engineering: A*, 154(2), pp. 139-148.
- Chen, H.Y., Manhart, J.K., Kunzelmann, H., Hickel, R., 2003. Polymerization contraction stress in light-cured compomer restorative materials. *Dental Materials*, 19(7), pp. 597-602.
- Cheng, Y.T., Cheng, C.M., 1999. Scaling relationships in conical indentation of elastic-perfectly plastic solids. *International Journal of Solids and Structures*, 36(8), pp. 1231-1243.
- Cheng, Y.T., Cheng, C.M., 2004. Scaling, dimensional analysis, and indentation measurements. *Materials Science and Engineering: R: Reports*, 44(4-5), pp. 91-149.
- Christensen, R.M., 1990. A critical evaluation for a class of micromechanics models. *Journal of the Mechanics and Physics of Solids*, 38(3), pp. 379-404.
- Chung, S.M., Yap, A.U.J., Koh, W.K., Tsai, K.T., Lim, C.T., 2004. Measurement of Poisson's ratio of dental composite restorative materials. *Biomaterials*, 25(13), pp. 2455-2460.

- Condon, J.R., Ferracane, J.L., 1998. Reduction of composite contraction stress through non-bonded microfiller particles. *Dental Materials*, 14, pp. 256–260.
- Condon, J.R., Ferracane, J.L., 2002. Reduced polymerization stress through non-bonded nanofiller particles. *Biomaterials*, 23, pp. 3807–3815.
- Craig, R.G., Peyton, F.A., 1958. Elastic and mechanical properties of human dentin. *Journal of Dental Research*, 37, pp.710-718.
- Craig, R.G., Peyton, F.A., Johnson, W., 1961. Compressive properties of enamel, dental cements, and gold. *Journal of Dental Research*, 40, pp. 936-943.
- Crystran Ltd, 2011. *Material properties of strontium fluoride (SrF₂)*. [online] Available at: <<http://www.crystran.co.uk/strontium-fluoride-srf2.htm>> [Accessed 14 July 2011].
- Danusso, F., Tieghi, G., 1986. Strength versus composition of rigid matrix particulate composites. *Polymer*, 27, pp. 1385–1390.
- Dao, M., Chollacoop, N., Van Vliet, K.J., Venkatesh, T.A., Suresh, S., 2001. Computational modeling of the forward and reverse problems in instrumented sharp indentation. *Acta Materialia*, 49(19), pp. 3899-3918.
- Dao, M., Gu, P., Maewal, A., Asaro, R. J., 1997. A micromechanical study of residual stresses in functionally graded materials. *Acta Materialia*, 45(8), pp. 3265-3276.
- Dauvillier, B.S., 2000. Visco-elastic parameters of dental restorative materials during setting. *Journal of Dental Research*, 79, pp. 818–823.

- Davidson, C.L., 1986. Resisting the curing contraction with adhesive composites. *Journal of Prosthetic Dentistry*, 55, pp. 446–447.
- Davidson, C.L., 2000. Handling of polymerization stresses in resin-based restorative materials. *Dental News*, 7(4), pp. 9–13.
- Davidson, C.L., Abdalla, A.I., 1993. Effect of thermal and mechanical load cycling on the marginal integrity of Class II resin composite restorations. *American Journal of Dentistry*, 6, pp. 39–42.
- Davidson, C.L., Abdalla, A.I., 1994. Effect of occlusal load cycling on the marginal integrity of adhesive Class V restorations. *American Journal of Dentistry*, 2, pp. 111.
- Dejak, B., Mlotkowski, A., 2008. Three-dimensional finite element analysis of strength and adhesion of composite resin versus ceramic inlays in molars. *The Journal of Prosthetic Dentistry*, 99(2), pp. 131-140.
- Deligeorgi, V., Mjör, I.A., Wilson, N.H., 2001. An overview of reasons for the placement and replacement of restorations. *Primary Dental Care*, 8, pp. 5–11.
- Dentsply, 2011. *Prime & Bond® NT technical report*. [online] Available at: <<http://www.dentsply.es/>> [Accessed 14 July, 2011].
- Drummond, J.L., 2008. Degradation, fatigue, and failure of resin dental composite materials. *Journal of Dental Research*, 87, pp. 710–719.

- Fagundes, T.C., Barata, T.J., Carvalho, C.A., Franco, E.B., Dijken, J.W. van., Navarro, M.F., 2009. Clinical evaluation of two packable posterior composites: a five-year follow-up. *The Journal of the American Dental Association*, 140(4), pp. 447–454.
- Fan, J.P., Tsui, C.P., Tang, C.Y., 2004a. Modeling of the mechanical behavior of HA/PEEK biocomposite under quasi-static tensile load. *Materials Science and Engineering A*, 382(1-2), pp. 341-350.
- Fan, J.P., Tsui, C.P., Tang, C.Y., Chow, C.L., 2004b. Influence of interphase layer on the overall elasto-plastic behaviors of HA/PEEK biocomposite. *Biomaterials*, 25(23), pp. 5363-5373.
- Feilzer, A.J., De Gee, A.J., Davidson, C.L., 1987. Setting stress in composite resin in relation to configuration of restoration. *Journal of Dental Research*, 66, pp. 1636–1639.
- Ferracane, J.L., Mitchem, J.C., 2003. Relationship between composite contraction stress and leakage in Class V cavities. *American Journal of Dentistry*, 16(4), pp. 239.
- Forss, H., Widstrom, E., 2004. Reasons for restorative therapy and the longevity of restorations in adults. *Acta Odontologica Scandinavica*, 62(2), pp. 82.
- Frank, R.M., Nalbandian, J., 1989. Structure and ultrastructure of dentin. In: B.K.B. Berkovitz, A. Boyde, R.M. Frank, H.J. Hohlings, B.J. Moxham, J. Nalbandian, eds. *Teeth*. New York: Springer-Verlag, pp. 212.

- Frazier, P.D., 1968. Adult human enamel: an electron microscopic study of crystallite size and morphology. *Journal of Ultrastructure Research*, 22, pp. 1-11.
- Frencken, J.E., 2010. The ART approach using glass-ionomers in relation to global oral health care. *Dental Materials*, 26, pp. 1-6.
- Frost, P.M., 2009. An audit on the placement and replacement of restorations in a general dental practice. *Primary Dental Care*, 9, pp. 31-36.
- Gao, H., Chae, O., 2010. Individual tooth segmentation from CT images using level set method with shape and intensity prior. *Pattern Recognition*, 43(7), pp. 2406-2417.
- Garberoglio, R., Brännström, M., 1976. Scanning electron microscopy investigation of human dentinal tubules. *Archives of Oral Biology*, 21, pp. 355-362.
- Gautier, L., Mortaigne, B., Bellenger, V., 1999. Interface damage study of hydrothermally aged glass-fibre-reinforced polyester composites. *Composites Science and Technology*, 59, pp. 2329-2337.
- Ge, J., Cui, F.Z., Wang, X.M., Feng, H.L., 2005. Property variations in the prism and the organic sheath within enamel by nanoindentation. *Biomaterials*, 26(16), pp. 3333-3339.
- Ghosh, S., Lee, K., Raghavan, P., 2001. A multi-level computational model for multi-scale damage analysis in composite and porous materials. *International Journal of Solids and Structures*, 38(14), pp. 2335-2385.

- Ghosh, S., Moorthy, S., 1998. Particle fracture simulation in non-uniform microstructures of metal–matrix composites. *Acta Materialia*, 46(3), pp. 965-982.
- Goldberg, A.J., 1990. Deterioration of restorative materials and the risk for secondary caries. *Advances in Dental Research*, 4, pp. 14.
- Gomez, C., Donly, K.J., 1994. In vitro demineralisation–remineralization of enamel caries at restoration margins utilizing fluoride-releasing composite resin. *Quintessence International*, 25, pp. 355–358.
- Griffin, F., Donly, K.J., Erickson, R., 1992. Caries inhibition by fluoride-releasing liners. *American Journal of Dentistry*, 5, pp. 293–295.
- Gu, Y. W., Yap, A. U. J., Cheang, P., Kumar, R., 2004. Spheroidization of glass powders for glass ionomer cements. *Biomaterials*, 25(18), pp. 4029-4035.
- Guild, F.J. Kinloch, A.J., 1994. Predictive modeling of the mechanical properties of rubber-toughened epoxy. *Journal of Materials Science Letters*, 13, pp. 629-632.
- Guild, F.J., Bonfield, W., 1998. Predictive modeling of the mechanical properties and failure processes in hydroxyapatite- polyethylene (Hapex™) composite. *Journal of Materials Science: Materials in Medicine*, 9(9), pp. 497-502.
- Gurbuz, T., Sengul, F., Altun, C., 2008. Finite element stress analysis of short-post core and over restorations prepared with different restorative materials. *Dental Materials Journal*, 27(4), pp. 499-507.

- Habelitz, S., Marshall, G.W., Balooch, M., Marshall, S.J., 2002. Nanoindentation and storage of teeth. *Journal of Biomechanics*, 35, pp. 995-998.
- Habelitz, S., Marshall, S.J., Marshall, G.W.Jr., Balooch, M., 2001. Mechanical properties of human dental enamel on the nanometer scale. *Archives of Oral Biology*, 46(2), pp. 173-183.
- Halpin, J.C., 1969. Stiffness and expansion estimates for oriented short fiber composites. *Journal of Composite Materials*, 3, pp. 732–734.
- Halpin, J.C., Tsai, S.W., 1969. Effects of environmental factors on composite materials. *Force Materials Laboratory Technical Report*, pp. 67-423.
- Hambli, R., Soulat, D., Gasser, A., Benhamou, C.L., 2009. Strain-damage coupled algorithm for cancellous bone mechano-regulation with spatial function influence. *Computer Methods in Applied Mechanics and Engineering*, 198(33), pp. 2673–2682.
- Hasegawa, A., Shinya, A., Nakasone, Y., Lassila, L.V.J., Vallittu, P.K., Shinya, A., 2010. *Development of 3D CAD/FEM Analysis System for Natural Teeth and Jaw Bone Constructed from X-Ray CT Images*. [online] Available at: <<http://www.mendeley.com/research/development-3d-cadfem-analysis-system-natural-teeth-jaw-bone-constructed-xray-ct-images/>> [Accessed 14 Sep, 2011]
- Hashin, Z., 1983. Analysis of composite materials—a survey. *Journal of Applied Mechanics*, 50(3), pp. 481–503.

- Hayashi, M., Wilson, N.H.F., 2003. Marginal deterioration as a predictor of failure of a posterior composite. *European Journal of Oral Sciences*, 111(2), pp. 155–162.
- He, L. H., Swain, M. V., 2007a. Enamel—A “metallic-like” deformable biocomposite. *Journal of Dentistry*, 35(5), pp. 431-437.
- He, L. H., Swain, M. V., 2007b. Influence of environment on the mechanical behavior of mature human enamel. *Biomaterials*, 28(30), pp. 4512-4520.
- He, L. H., Swain, M.V., 2007c. Nanoindentation derived stress-strain properties of dental materials. *Dental Materials*, 23, pp. 814-821.
- He, L. H., Swain, M. V., 2008. Understanding the mechanical behaviour of human enamel from its structural and compositional characteristics. *Journal of the Mechanical Behavior of Biomedical Materials*, 1(1), pp. 18-29.
- He, L.H., Swain, M.V., 2009. Enamel-A functionally graded natural coating. *Journal of Dentistry*, 37, pp. 596-603.
- Hedia, H.S., Mahmoud, N.A., 2004. Design optimization of functionally graded dental implant. *Biomedical Materials and Engineering*, 14(2), pp. 133-143.
- Herzberg, R., Dolev E., Schwartz-Arad D., (2006). Implant marginal bone loss in maxillary sinus grafts. *The International Journal of Oral and Maxillofacial Implants*, 21(1), pp.103–10.
- Hill, R., 1948. A theory of the yielding and plastic flow of anisotropic metals. *Proceedings of the Royal Society of London*, 193, pp. 281–297.

- Hill, R.G., Wilson, A.D., 1988. Some structural aspects of glasses used in ionomer cements. *Glass Technology*, 29, pp. 150–167.
- Ho, S. T., Hutmacher, D.W., 2006. A comparison of micro CT with other techniques used in the characterization of scaffolds. *Biomaterials*, 27(8), pp. 1362-1376.
- Huang, H.L., Huang, J.S., Ko, C.C., Hsu, J.T., Chang, C.H., Chen, M.Y., 2005. Effects of splinted prosthesis supported a wide implant or two implants: a three-dimensional finite element analysis. *Clinical Oral Implants Research*, 16, pp. 466–472.
- Huang, T.J.G., Schilder, H., Nathanson, D., 1992. Effects of moisture content and endodontic treatment on some mechanical properties of human dentin. *Journal of Endodontics*, 18, pp. 209-215.
- Hulme, P.A., Boyd, S.K., Ferguson, S.J., 2007. Regional variation in vertebral bone morphology and its contribution to vertebral fracture strength. *Bone*, 41(6), pp. 946-957.
- Huo, B., 2005. An inhomogeneous and anisotropic constitutive model of human dentin. *Journal of Biomechanics*, 38(3), pp. 587-594.
- Huo, B., Zheng, Q.S., 1999. Effect of dentin tubules to the mechanical properties of dentin. Part I: Stress–strain relations and strength criterion. *Acta Mechanica Sinica*, 15(4), pp. 355–364.

- Ichim, I., Li, Q., Li, W., Swain, M.V., Kieser, J., 2007a. Modeling of fracture behavior in biomaterials. *Biomaterials*, 28(7), pp. 1317-1326.
- Ichim, I., Schmidlin, P.R., Kieser, J.A., Swain, M.V., 2007b. Mechanical evaluation of cervical glass-ionomer restorations: 3D finite element study. *Journal of Dentistry*, 35(1), pp. 28-35.
- Jenkins, W.M., 1997. An introduction to neural computing for the structural engineer. *The Structural Engineer*, 75(3), pp. 38–41.
- Jensen, M.E., Wefel, J.S., Hammesfahr, P.D., 1991. In vitro recurrent caries. *General Dentistry*, 39, pp. 12–17.
- Jiang, W., Bo, H., YongChun, G., LongXing, N., 2010. Stress distribution in molars restored with inlays or onlays with or without endodontic treatment: A three-dimensional finite element analysis. *The Journal of Prosthetic Dentistry*, 103(1), pp. 6-12.
- Jones, S.J., Boyde, A., 1984. Ultrastructure of dentin and dentinogenesis. In: J. Linde, ed. *Dentin and dentinogenesis*. Boca Raton: CRC Press, pp. 81-134.
- Katz, J.L., 1971. Hard tissue as a composite material. I. Bounds on the elastic behavior. *Journal of Biomechanics*, 4, pp. 455-73.
- Kemp-Scholte, C.M., Davidson, C.L., 1990. Complete marginal seal of class V resin composite restorations effected by increased flexibility. *Journal of Dental Research*, 69, pp. 1250–1253.

- Kerebel, B., Daculsi, G., Kerebel, L.M., 1979. Ultrastructural studies of enamel crystallites. *Journal of Dental Research*, 57, pp. 306-12.
- Kim, H.S., Hong, S.I., Kim, J.L., 2001. On the rule of mixtures for predicting the mechanical properties of composites with homogeneously distributed soft and hard particles. *Journal of Materials Processing Technology*, 112(1), pp. 109-113.
- Kinney, J.H., Balooch, M., Marshall, G.W., Marshall, S.J., 1993. Atomicforce microscopic study of dimensional changes in human dentine during drying. *Archives of Oral Biology*, 38, pp. 1003-1007.
- Kinney, J.H., Balooch, M., Marshall, G.W., Marshall, S.J., 1999. A micromechanics model of the elastic properties of human dentine. *Archives of Oral Biology*, 44(10), pp. 813–822.
- Kinney, J.H., Oliveira, J., Haupt, D.L., Marshall, G.W., Marshall, S.J., 2001a. The spatial arrangement of tubules in human dentin. *Journal of Materials Science: Materials in Medicine*, 12, pp. 743-751.
- Kinney, J.H., Pople, J.A., Marshall, G.W., Marshall, S.J., 2001b. Collagen orientation and crystallite size in human dentin:a small angle x-ray scattering study. *Calcified Tissue International*, 69, pp. 31-37.
- Kinomoto, Y., 1999. Comparison of polymerisation contraction stresses between self- and light-curing composites. *Journal of Dentistry*, 27, pp. 383–389.

- Kraus, R., Wilke, W., Zhuk, A., Luzinov, I., Minko, S., Voronov, A., 1997. Investigation of debonding processes in particle-filled polymer materials by acoustic emission. *Journal of Material Science*, 32, pp. 4397–4403.
- Lacroix, D., Chateau, A., Ginebra, M.P., Planell, J.A., 2006. Micro-finite element models of bone tissue-engineering scaffolds. *Biomaterials*, 27(30), pp. 5326-5334.
- Lee, S.Y., Chiang, H.C., Lin, C.T., Huang, H.M., Dong, D.-R., 2000. Finite element analysis of thermo-debonding mechanism in dental composites, *Biomaterials*, 21, pp.1315–1326.
- Lemaitre, J. 1992. A course on Damage Mechanics. *Springer-Verlag*, pp. 210.
- Levita, G., Marchetti, A., Lazzeri, A., 1989. Fracture of ultrafine calcium carbonate/polypropylene composites. *Polymer Composites*, 10, pp. 39–43.
- Li, G.C., Ling, X.W., Shen, H., 2000. On the mechanism of void growth and the effect of straining mode in ductile materials. *International Journal of Plasticity*, 16(1), pp. 39-57.
- Li, H., Li, J., Zou,Z., Fok,A.S., 2011. Fracture simulation of restored teeth using a continuum damage mechanics failure model. *Dental Materials*, 27(7), pp. e125-e133.
- Li, H., Yun, X., Li, J., Shi, L., Fok, A.S., Madden, M.J., Labuz, J.F., 2010. Strengthening of a model composite restoration using shape optimization: A numerical and experimental study. *Dental Materials*, 26(2), pp. 126-134.

- Lin, C.N., Chang, Y.H., Lin, Y.F., 2008a. Combining structural-thermal coupled field FE analysis and the Taguchi method to evaluate the relative contributions of multi-factors in a premolar MOD restoration. *Journal of Dentistry*, 36(8), pp. 626-636.
- Lin, C.L., Chang, Y.H., Liu, P.R., 2008b. Multi-factorial analysis of a cusp-replacing adhesive premolar restoration: A finite element study. *Journal of Dentistry*, 36(3), pp. 194-203.
- Lin, D., Li, Q., Li, W., Zhou, S., Swain, M.V., 2009. Design optimization of functionally graded dental implant for bone remodeling. *Composites Part B: Engineering*, 40(7), pp. 668-675.
- Llorca, A., Martin, J.R., Elices, M., 1993. Particulate fracture during deformation of a spray formed metal-matrix composites. *Metallurgical Transactions A, Physical Metallurgy and Materials Science*, 24A, pp. 1575-1588.
- Luccioni, B., Oller, S., Danesi, R., 1995. Plastic damaged model for anisotropic materials. *Applied Mechanics in the Americas*, I, pp. 124–129.
- Luo, J., Lin, J., 2007. A study on the determination of plastic properties of metals by instrumented indentation using two sharp indenters. *International Journal of Solids and Structures*, 44(18-19), pp. 5803-5817.
- Magne, P., 2007. Efficient 3D finite element analysis of dental restorative procedures using micro-CT data. *Dental Materials*, 23(5), pp. 539-548.
- Mahler, D.B., Engle, J.H., 2000. Clinical evaluation of amalgam bonding in class I and II restorations. *The Journal of the American Dental Association*, 131(1), pp. 43.

- Malafaya, P.B., Santos, T.C., Van Griensven, M., 2008. Morphology, mechanical characterization and in vivo neo-vascularization of chitosan particle aggregated scaffolds architectures. *Biomaterials*, 29(29), pp. 3914-3926.
- Manski, R.J., Brown, E., 2007. Dental use, expenses, private dental coverage, and changes, 1996 and 2004. Rockville (MD): Agency for Healthcare Research and Quality. *Medical Eependiture Panel Survey Chartbook No.17*, pp. 4.
- Martin, N., Jedyakiewicz, N.M., Fisher, A.C., 2003. Hygroscopic expansion and solubility of composite restoratives. *Dental Materials*, 19, pp. 77-86.
- McLean, J.W., Nicholson, J.W., Wilson, A.D., 1994. Proposed nomenclature for glass-ionomer dental cements and related materials. *Quintessence International*, 25, pp. 587-589.
- Mesarovic, S.D., Fleck, N.A., 2000. Frictionless indentation of dissimilar elastic-plastic spheres, *International Journal of Solids and Structures*, 37(46-47), pp. 7071-7091.
- Meyer, J.M., Cattani-Lorente, M.A., Dupuis, V., 1998. Compomers: between glass-ionomer cements and composites. *Biomaterials*, 19, pp. 529-539.
- Miura, J., Maeda, Y., Nakai, H., Zako, M., 2009. Multiscale analysis of stress distribution in teeth under applied forces. *Dental Materials*, 25(1), pp. 67-73.
- Mjör, I.A. and Fejerskov, O., 1986. *Human Oral Embryology and Histology*. Copenhagen: Munksgaard.

Mjör, I.A., 1985. Frequency of secondary caries at various anatomical locations. *Operative Dentistry*, 10, pp. 88–92.

Mjör, I.A., 1997. The reasons for replacement and the age of failed restorations in general dental practice. *Acta Odontologica Scandinavica*, 55, pp. 58–63.

Mjör, I.A., Moorhead, J.E., 1998. Selection of restorative materials, reasons for replacement, and longevity of restorations in Florida. *The Journal of the American College of Dentists*, 65, pp. 27–33.

Mjör, I.A., Moorhead, J.E., Dahl, J.E., 2000. Reasons for replacements of restorations in permanent teeth in general dental practice. *International Dental Journal*, 50, pp. 361–366.

Mjör, I.A., Shen, C., Eliasson, S.T., Richter, S., 2002. Placement and replacement of restorations in general dental practice in Iceland. *Operative Dentistry*, 27, pp. 117–123.

Munehika, T., Suzuki, K., Nishiyama, M., Ohashi, M., Horie K., 1984. A comparison of the tensile bond strengths of composite resins to longitudinal and transverse sections of enamel prisms in human teeth, *Journal of Dental Research*, 63, pp.1079–1082.

Nalla, R.K., Kinney, J.H., Ritchie, R.O., 2003. On the fracture of human dentin- Is it stress- or strain-controlled?. *Journal of Biomedical Materials Research*, 67A, pp. 484–495.

- Nanci, A., 2003. Enamel: Composition, formation, and structure. In: Nanci, A , ed. *Ten Cate's Oral Histology: Development, structure, and function*. St. Louis: Mosby.
- Nielsen, L.E., 1966. Simple theory of stress–strain properties of filled polymers. *Journal of Applied Polymer Science*, 10, pp. 97–103.
- Oliver, W.C., Pharr, G.M., 1992. An improved technique for determining hardness and elastic modulus using load and displacement sensing indentation experiments. *Journal of Materials Research*, 7(6), pp. 1564.
- Oller, S., Botello, S., Miquel, M., Oñate, E., 1995. Anisotropic elasto-plastic model based on an isotropic formulation. *Engineering Computations*, 12, pp. 245–262.
- Opdam, N.J.M., Bronkhorst, E.M., Roeters, J.M., Loomans, B.A.C., 2007. A retrospective clinical study on longevity of posterior composite and amalgam restorations. *Dental Materials*, 23(1), pp. 2.
- Orams, H.J., Phakey, P.P., Rachinger, W.A., Zybert, J.J., 1974. Visualization of micropore structure in human dental enamel. *Nature*, 252, pp. 584-585.
- Oshida, Y., Gorthy, J., 1999. Water-sorption kinetics of dental polymeric resin under tensile stressing conditions. *Bio-Medical Materials and Engineering*, 9, pp. 125–133.
- Osorio, E., Toledano, M., Bravo, M., Osorio, R., 1995. Short-term changes in lymphocytes after placement of silver amalgam restorations in healthy subjects. *Dental Materials*, 11, pp. 323-326.

- Owen, D.R.J., and Hinton, E., 1982. *Finite Elements in Plasticity: Theory and Practice*. Pineridge Press Ltd., Swansea, U.K.
- Park, S., Quinn, J.B., Romberg, E., Arola, D., 2008. On the brittleness of enamel and selected dental materials. *Dental Materials*, 24(11), pp. 1477-1485.
- Pashley, D.H., 1948. Dentin: a dynamic substrate—a review. *Scanning Microscopy*, 3, pp. 161–176.
- Pereira, R.A., Araujo, P.A., Castañeda-Espinosa, J.C., Mondelli, R.F., 2008. Comparative analysis of the shrinkage stress of composite resins. *The Journal of Applied Oral Science*, 16(1), pp. 30–34.
- Petersen, P.E., 2003. The World Oral Health Report 2003; continuous improvement of oral health in the 21st century - the approach of the WHO Global Oral Health Programme. *Community Dentistry and Oral Epidemiology*, 31(1), pp. 3-24.
- Petersen, P.E., 2009. Global policy for improvement of oral health in the 21st century- implications to oral health research of World Health Assembly 2007, World Health Organization. *Community Dent Oral Epidemiol*, 37(1), pp. 1-8.
- Peyton, F.A., Mahler, D.B., Hershenov, B., 1952. Physical properties of dentin. *Journal of Dental Research*, 31, pp. 336–370.
- Phillips, R.W., 1991. *Skinner's science of dental materials*. 9th ed. Philadelphia: W.B. Saunders Co.

- Pukanszky, B., Turcsanyi, B. Tudos, F., 1988. Effect of interfacial interaction on the tensile yield stress of polymer composites. In: H. Ishida, ed. *Interfaces in polymer, ceramic and metal matrix composites*. Amsterdam: Elsevier, pp. 467–477.
- Qin, Q.H., Swain, M.V., 2004. A micro-mechanics model of dentin mechanical properties. *Biomaterials*, 25(20), pp. 5081-5090.
- Reich, F.R., Brenden, B.B. and Porter, N.S., 1967. *Ultrasonic imaging of teeth*. Washington: Batelle Memorial Institute.
- Renson, C.E., 1970. An experimental study of the physical properties of human dentine. *PhD Thesis*, University of London.
- Renson, C.E., Braden, M., 1971. The experimental deformation of dentine by indenters. *Archives of Oral Biology*, 16, pp. 563-572.
- Rodrigues, F.P., Li, J., Silikas, N., Ballester, R.Y., Watts D.C., 2009. Sequential software processing of micro-XCT dental-images for 3D-FE analysis. *Dental Materials*, 25(6), pp.e47-e55.
- Roy, S., Basu, B., 2008. Mechanical and tribological characterization of human tooth. *Materials Characterization*, 59(6), pp. 747-756.
- Rudolph, H., Luthardt, R.G., Walter, M.H., 2006. Computer-aided analysis of the influence of digitizing and surfacing on the accuracy in dental CAD/CAM technology. *Computers in Biology and Medicine*, 37(5), pp. 579-587.

- Sakaguchi, R.L., 2005. Review of the current status and challenges for dental posterior restorative composites: clinical, chemistry, and physical behavior considerations. *Dental Materials*, 21, pp. 3–6.
- Sakaguchi, R.L., Wiltbank, B.D., Murchison, C.F., 2005. Cure induced stresses and damage in particulate reinforced polymer matrix composites: a review of the scientific literature. *Dental Materials*, 21(1), pp. 43-46.
- Sano, H., Ciucchi, B., Matthews, W.G., Pashley, D.H., 1994. Tensile properties of mineralized and demineralized human and bovine dentin. *Journal of Dental Research*, 73, pp. 1205-1211.
- Sarrett, D.C., 2005. Clinical challenges and the relevance of materials testing for posterior composite restorations. *Dental Materials*, 21, pp. 9–20.
- Schulze, K.A., Zaman, A.A., Söderholm, K.J.M., 2003. Effect of filler fraction on strength, viscosity and porosity of experimental compomer materials. *Journal of Dentistry*, 31(6), pp. 373-382.
- Shor, A., Nicholls, J.I., Phillips, K.M., Libman, W.J., 2003. Fatigue load of teeth restored with bonded direct composite and indirect ceramic inlays in MOD class II cavity preparations. *International Journal of Prosthodontics*, 16(1), pp. 64–69.
- Sideridou, I., Tserki, V., Papanastasiou, G., 2003. Study of water sorption, solubility and modulus of elasticity of light-cured dimethacrylate-based dental resins. *Biomaterials*, 24(4), pp. 655-665.

- Simmelink, J.W., 1987. Histology of enamel. In: J.K. Avery, ed. *Oral development and histology*. Baltimore: Williams & Wilkins, pp. 140–151.
- Smith, E.D., Martin, F.E., 1992. Microleakage of glass ionomer/composite resin restorations: A laboratory study. I. The influence of glass ionomer cement. *Australian Dental Journal*, 37, pp. 23–30.
- Sneddon, I.N., 1965. The relation between load and penetration in the axisymmetric Boussinesq problem for a punch of arbitrary profile. *International Journal of Engineering Science*, 3, pp. 47-56.
- Spears, I.R., 1997. A three-dimensional finite element model of prismatic enamel: a re-appraisal of the data on the Young's modulus of enamel. *Journal of Dental Research*, 76, pp. 1690–1697.
- Staines, M., Robinson, W.H., Hood, J.A.A., 1981. Spherical indentation of tooth enamel. *Journal of Material Science*, 16(9), pp. 2551-2556.
- Suliman, A.A., Boyer, D.B., Lakes, R.S., 1993. Cusp movement in premolars resulting from composite polymerization shrinkage. *Dental Materials*, 9, pp. 6–10.
- Tabor, D., 1951. *The hardness of metals*. Oxford: Clarendon Press.
- Toledo, M.W.E., Nallim, L.G., Luccioni, B.M., 2008. A micro-macromechanical approach for composite laminates. *Mechanics of Materials*, 40(11), pp.885-906.

- Toparli, M., Koksai, N.S., 2005. Hardness and yield strength of dentin from simulated nano-indentation tests. *Computer Methods and Programs in Biomedicine*, 77(3), pp. 253-257.
- Tsui, C.P., Chen, D.Z., Tang, C.Y., Uskokovic, P.S., Fan, J.P., 2005. Prediction for debonding damage process of glass beads-reinforced modified polyphenylene oxide under simple shear. *Journal of Materials Processing Technology*, 167(2-3), pp. 429-437.
- Tsui, C.P., Chen, D.Z., Tang, C.Y., Uskokovic, P.S., Fan, J.P., Xie, X.L., 2006. Prediction for debonding damage process and effective elastic properties of glass-bead-filled modified polyphenylene. *Composites Science and Technology*, 66(11-12), pp. 1521-1531.
- Tsui, C.P., Tang, C.Y., Fan, J.P., Xie, X.L., 2004. Prediction for initiation of debonding damage and tensile stress–strain relation of glass-bead-filled modified polyphenylene oxide. *International Journal of Mechanical Sciences*, 46(11), pp. 1659-1674.
- Tunvisut, K., O'Dowd, N.P., Busso, E.P., 2001. Use of scaling functions to determine mechanical properties of thin coatings from microindentation tests. *International Journal of Solids and Structures*, 38(2), pp. 335-351.
- Turcsanyi, B., Pukanszky, B., Tudos, F., 1988. Composition dependence of tensile yield stress in filled polymers. *Journal of Materials Science Letters*, 7, pp. 160–162.

- Turner, M. J., Clough, R. W., Martin, H. C., Topp, L. J., 1956. Stiffness and deflection analysis of complex structures. *Journal of Aerospace Science*, 23, pp. 805-823.
- Tvergaard, V., 1982. On localization in ductile materials containing spherical voids. *International Journal of Fracture*, 18, pp. 237-252.
- Tyas, M.J., 2003. Milestones in adhesion: Glass-ionomer cements. *The Journal of Adhesive Dentistry*, 5, pp. 259–266.
- Tyldesley, W.R., 1959. The mechanical properties of human enamel and dentine. *British Dental Journal*, 106, pp. 269-278.
- Ulusoy, Ç., Darendeliler, N., 2008. Effects of Class II activator and Class II activator high-pull headgear combination on the mandible: A 3-dimensional finite element stress analysis study. *American Journal of Orthodontics and Dentofacial Orthopedics*, 133(4), pp. 490.e9-490.e15.
- Van Meerbeek, B., Willems, G., Celis, J.P., Roos, J.R., Braem, M., Lambrechts, P., Vanherle, G., 1993. Assessment by nano-indentation of the hardness and elasticity of the resin-dentin bonding area. *Journal of Dental Research*, 72, pp. 1434-1442.
- Wang, H.Y., Poul, E.P., You, B.J., Xue, Z.B., 2002. The second national survey of oral health status of children and adults in China. *International Dental Journal*, 52(4), pp. 283-90.
- Wang, L., Rokhlin, S.I., 2005. Universal scaling functions for continuous stiffness nanoindentation with sharp indenters Original Research Article. *International*

Journal of Solids and Structures, 42(13), pp. 3807-3832.

Watts, D.C., El Mowafy, O.M., Grant, A.A., 1987. Temperature dependence of compressive properties of human dentin. *Journal of Dental Research*, 66, pp. 29-32.

Weisstein, E., 1999. *CRC Concise Encyclopedia of Mathematics*. CRC Press.

Wilson, A.D., Clinton, D. Miller, R.P., 1972. The formation and microstructure of dental silicate cements. *Journal of Materials Science*, 7, pp. 220.

Wilson, A.D., Kent, B.E., 1971. The glass ionomer cement, a new translucent dental filling material. *Journal of Applied Chemistry and Biotechnol*, 21, pp. 313.

Wilson, A.D., McLean, J.W., 1988. *Glass Ionomer Cement*. Chicago: Quintessence Publishers.

Wilson, N.H., Burke, F.J., Mjör, I.A., 1997. Reasons for placement and replacement of restorations of direct restorative materials by a selected group of practitioners in the United Kingdom. *Quintessence International*, 28, pp. 245–248.

Wu, W., Sadeghipour, K., Boberick, K., Baran, G., 2002. Predictive modeling of elastic properties of particulate-reinforced composites. *Materials Science and Engineering A*, 332(1-2), pp. 362-370.

Wu, Y., Dong, Z., 1995. Three-dimensional finite element analysis of composites with coated spherical inclusions. *Materials Science and Engineering A*, 203(1-2), pp. 314-323.

- Xi, Y.L., Chai, D.L., Zhang, W.X., Zhou, J.E., 2006. Titanium alloy reinforced magnesium matrix composite with improved mechanical properties. *Scripta Materialia*, 54(1), pp. 19-23.
- Xie, D., Brantley, W.A., Culbertson, B.M., Wang, G., 2000. Mechanical properties and microstructures of glass-ionomer cements. *Dental Materials*, 16(2), pp.129-138.
- Xu, X., Burgess, J.O., 2003. Compressive strength, fluoride release and recharge of fluoride-releasing materials. *Biomaterials*, 24(14), pp. 2451-2461.
- Yaman, S.D., Yetmez, M., Türköz, E., Akkas, N., 2000. Fracture resistance of Class II approximal slot restorations. *The Journal of Prosthetic Dentistry*, 84(3), pp. 297-302.
- Yan, J., Karlsson, A.M., Chen, X., 2007. Determining plastic properties of a material with residual stress by using conical indentation original research article. *International Journal of Solids and Structures*, 44(11-12), pp. 3720-3737.
- Yan, J., Taskonak, B., Platt, J.A., Mecholsky, J.J.Jr., 2008. Evaluation of fracture toughness of human dentin using elastic–plastic fracture mechanics. *Journal of Biomechanics*, 41(6), pp. 1253-1259.
- Yap, A.U.J., Wang, X., Wu, X., Chung, S.M., 2004. Comparative hardness and modulus of tooth-colored restoratives: A depth-sensing microindentation study. *Biomaterials*, 25(11), pp. 2179-2185.

- Young, A.M., Raffeka, S.A., Howlett, J.A., 2004. FTIR investigation of monomer polymerisation and polyacid neutralisation kinetics and mechanisms in various aesthetic dental restorative materials. *Biomaterials*, 25, pp. 823–833.
- Yukitani, W., Hasegawa, T., Itoh, K., Hisamitsu, H., Wakumoto, S., 1997. Marginal adaptation of dental composites containing prepolymerized filler. *Operative Dentistry*, 22, pp. 242–248.
- Zahl, D.B., Meeking, R.M.M., 1991. The influence of the residual stress on the yielding of metal matrix composites. *Acta Metallurgica*, 39, pp. 1117-1122.
- Zhang, J.T., Liu, L.S., Zhai, P.C., Fu, Z.Y., Zhang, Q.J., 2007. The prediction of the dynamic responses of ceramic particle reinforced MMCs by using multi-particle computational micro-mechanical method. *Composites Science and Technology*, 67(13), pp. 2775-2785.
- Zhao, M., Ogasawara, N., Chiba, N., Chen, X., 2006. A new approach to measure the elastic–plastic properties of bulk materials using spherical indentation. *Acta Materialia*, 54(1), pp. 23-32.
- Zimmerman, B.F., Rawls, H.R. Querens, A.E., 1984. Prevention of in vitro secondary caries with an experimental fluoride-exchanging resin. *Journal of Dental Research*, 63, pp. 689–692.
- Ziskind, D., Fleischer, S., Zhang, K., Cohen, S.R., Wagner, H.D., 2010. A novel experimental method for the local mechanical testing of human coronal dentin. *Dental Materials*, 26(2), pp. 179-184.

Ziskind, D., Hasday, M., Cohen, S.R., Wagner, H.D., 2011. Young's modulus of peritubular and intertubular human dentin by nano-indentation tests. *Journal of Structural Biology*, 174(1), pp. 23-30.